Using Electrons to Fabricate and Characterise Three-Dimensional Ferromagnetic Nanostructures

Aurys Šilinga
School of Physics & Astronomy, College of Science & Engineering
University of Glasgow

February 2026

A dissertation submitted in fulfilment of the requirements for the degree of
Doctor of Philosophy

Abstract

The study of electronics that utilise the spin of electrons has led to significant technological developments for data storage applications. The manufacturing of electronics on flat substrates is well established, and hence electron spin tends to be integrated into two-dimensional (2D) computer chips and data storage devices by design. This work investigates how spintronics may be extended to three-dimensional (3D) nanoscale structures. The additive manufacturing method of focused electron beam induced deposition (FEBID) is optimised for the fabrication of free-standing ferromagnetic nanowires (NWs). Vertical and angled NWs are tailored to exhibit consistent compositional and magnetic properties, which enhances the fabrication of free-standing spintronic circuits. The advanced transmission electron microscopy (TEM) method of off-axis electron holography is used to characterise the magnetic configurations in a 3D $\wedge$-shaped NW structure, and a method is developed for tomographic reconstruction of magnetisation in 3D. The tomographic method, based on model-based iterative reconstruction (MBIR), incorporates tomographic alignment and image-distortion correction algorithms, enabling experimental reconstruction of a 3D magnetisation vector field with a spatial resolution of 50 nm. To assess the applicability of the reconstruction method to other datasets, simulations are performed that test known limitations of TEM methods. The effects of a limited range of sample rotations are evaluated in simulations of NWs. It is found that spatial averaging between the vacuum and the sample surface can occur when tomographic datasets contain too few projections. In addition, Néel domain walls (DWs) and Bloch points are simulated to test how the MBIR algorithm treats magnetic configurations that are conventionally invisible to TEM. The reconstruction is limited to revealing only magnetic moments that create detectable signals. Overall, methods

were developed for the fabrication of consistently ferromagnetic 3D NW structures and for the characterisation of 3D magnetic configurations within them.

Declaration

This thesis details research I performed under the supervision of Trevor P. Almeida in the Materials and Condensed Matter Physics group at the University of Glasgow, from 2022 to 2026. The content of this thesis is my own work, except where explicit attribution to others is made.

- Chapters 1 and 2 review literature relevant to my research.
- Chapter 3 is based on a manuscript in preparation. Trevor P. Almeida acquired the data underlying Figures 3.9a & 3.10a. Keir Edgar performed Mumax micromagnetic simulations and provided Figures 3.1a & 3.8. Rafal E. Dunin-Borkowski, Kayla Fallon, András Kovács, and Stephen McVitie reviewed & edited the manuscript.
- Chapter 4 is based on work published in the Microscopy and Microanalysis journal [1]. Trevor P. Almeida and András Kovács supervised the work. Rafal E. Dunin-Borkowski, Kayla Fallon, and Stephen McVitie reviewed & edited the manuscript.
- Chapter 5 is based on a supplementary study published with the previous article [1].
- Chapter 6 draws conclusions based on the previous chapters.

Aurys Šilinga

Acknowledgements

My time as a postgraduate researcher has been excellent, and this is owed to the wonderful people around me. Some notable mentions are:

- My supervisor, Trevor P. Almeida. His dedication, guidance, pleasant manner, and ability to attract funding have made all of this possible.
- My parents and brother, Arvydas, Jolita, and Rytis. Their never-ending support has allowed me to arrive at the circumstances that enabled me to pursue a PhD.
- My collaborators, who are named in the declaration obove. Their wisdom and feedback have shaped my work, career path, and dreams.
- The Materials and Condensed Matter Physics group, in particular, the technicians Colin How, Sam McFadzean, and William Smith. Who have been welcoming, supportive, and taught me all I know about electron microscopy.
- The Institute of Physics, Royal Microscopy Society, UK Magnetics Society, Helmholtz Information and Data Science Academy (HiDA), the Microscopy Society of America, and the Rogers Scholars Fund. Who have awarded bursaries, which enabled me to present this work at international conferences in the United Kingdom, Germany, and the United States.
- My everyday companions, Amelia and Théo. Who have made life in Glasgow that wee bit better.
- The sportsmen, Adam and Dr Naskar. Who are good company, and helped keep our bodies from withering while we were lost in academic pursuits.
- The Research Lounge YouTube Channel. For presenting my papers on their talk shows.
- Stubz, the good boy whose mortal coil expired during the writing of this thesis.

List of abbreviations and symbols

Abbreviations

2D	Two-dimensional
3D	Three-dimensional
ADF	Annular dark field
AI	Artificial intelligence
BPDV	Bloch point domain wall
CAD	Computer-assisted design
CCD	Charge-coupled device
CG	Conjugate gradient
CMOS	Complementary metal oxide semiconductor
CPU	Central processing unit
CT	Computed tomography
DMI	Dzyaloshinskii–Moriya interaction
DPC	Differential phase contrast
DW	Domain wall
EELS	Electron energy loss spectroscopy
EH-VFT	Electron holographic vector field tomography
EI	Electron impact
E-T	Everhart–Thornley
FEBID	Focused electron induced deposition
FEG	Field emission gun
FFT	Fast Fourier transform
FWHM	Full-width at half-maximum
GIS	Gas injection system
HAADF	High-angle annular dark field
IMFP	Inelastic mean free path
LLS	Low-loss spectrum
LTEM	Lorentz transmission electron microscope
MBIR	Model-based iterative reconstruction
MRAM	Magnetic random access memory
NW	Nanowire
RM	Racetrack memory
RMS	Root-mean-square
SAV	Surface anti-vortex
SE	Secondary electron
SEM	Scanning electron microscope
SNR	Signal-to-noise ratio

STEM	Scanning transmission electron microscope
TEM	Transmission electron microscope
TD	Thermal dissociation
TVDW	Transverse vortex domain wall
VDW	Vortex domain wall

Common symbols

$\boldsymbol{B}$	Magnetic induction vector field
e	Euler's number
E	Energy
$\boldsymbol{H}$	Magnetic H-field
$\boldsymbol{k}$	Wave vector
$\boldsymbol{M}$	Magnetisation vector field
M_s	Saturation magnetisation
μ_0	Vacuum permeability
m_e	Relativistic electron mass
q_e	Electron charge
r	Radius
v	Relativistic speed
φ	Phase shift
Ψ	Wave function
(x, y, z)	Cartesian coordinates

Al	Aluminium
Au	Gold
C	Carbon
Co	Cobalt
Cu	Copper
Fe	Iron
O	Oxygen
Pt	Platinum
Si	Silicon
W	Tungsten

Contents

Chapter 1.

Introduction and Theory

"A sea of electrons."
— A popular analogy for describing electrons in metals.

1.1. Overview of nano-magnetism research

Over the last 60 years, the performance of standard-sized computer microchips has doubled every two years [2, 3]. These advancements in hardware, known as Moore's Law, have enabled many technological developments, including smartphones and consumer-accessible artificial intelligence (AI), but further improvements will be challenging. Since approximately 2020, the classical approach of fabricating smaller components with increased density on a silicon microchip is no longer viable because the operation of transistor gates is no longer adequately described by classical physics below 10 nm length scales, and quantum mechanics comes into effect. At quantum length scales, controlling the flow and storage of electrical charge on silicon chips becomes more challenging due to quantum tunnelling. This can be overcome by classical means, e.g., correcting charge levels more frequently; however, the overall processing speed of microchips does not improve significantly compared to incorporating larger components [4]. Consequently, new technologies are being researched to harness quantum mechanics in the development of computer hardware [5]. Among the many research directions considered globally, this thesis focuses on new 3D architectures for spintronic applications.

Although conventional electronics physically represent binary bit information (0 or 1) by the amount of charge stored in capacitors, the research field of spintronics develops methods to represent data using electron spin [6]. In ferromagnetic materials, magnetic moments arising from electron spins in atoms can be aligned to form magnetic domains, and their orientation can be used to represent data. In theory, rotating electron spins to represent bit values changing from 0 to 1 could be more energy efficient than the conventional electronic approach of translating electrons between capacitor plates [7]. Due to their unique properties, the study of nanoscale ferromagnets has led to the development of a range of impactful technologies [6]. Examples include: tunnelling magnetoresistive junctions that have improved the readout signal and enabled increased data storage density in magnetic hard disk drives [8]; magnetic random access memory (MRAM), which is a non-volatile implementation of RAM, that does not need a constant supply of power to store data [9]; magnetic racetrack memory (RM) that is a non-volatile shift-register, which can be scaled to implement (3D) stacking [10]; and artificial neural networks based on stochastic magnetic DW motion [11]. Figure 1.1 shows a diagram of a RM system and its operation by shifting, reading, and overwriting patterned magnetic domains. Regarding continued development, the emerging research field of 3D nanomagnetism is of particular interest as extending conventionally planar spintronic systems into 3D geometries unlocks one more degree of freedom [12]. Implementing 3D stacking has been shown to increase component density on microchips [13], and altering 3D geometry can tune device performance via geometry-dependent anisotropy [14] or symmetry breaking [15]. The emerging field of 3D nanomagnetism involves the development of theory, fabrication, and characterisation methods for completely novel spintronic circuits [12].

This thesis discusses the development of methods for the fabrication and characterisation of 3D nanomagnetic devices. First, electron microscopy (EM) methods are introduced for fabrication of nanoscale materials and characterisation of their chemical, structural and magnetic properties. Then, a 3D-printing EM method for ferromagnetic nanostructures is tested, and improvements to fabrication quality are discussed. To characterise the fabricated nanostructures, a method is developed for reconstruction of the 3D distributions of spins in a ferromagnetic NW structure. Following this, simulations are used to evaluate the conditions under which the spin reconstructions are accurate and the types of samples that can be characterised are described. In summary, investigations of 3D nanomagnetism often lead to the discovery of interesting physical phenomena, and in this thesis methods are developed for optimised fabrication, accurate simulation, and 3D characterisation of ferromagnetic NWs arranged in bespoke 3D structures.

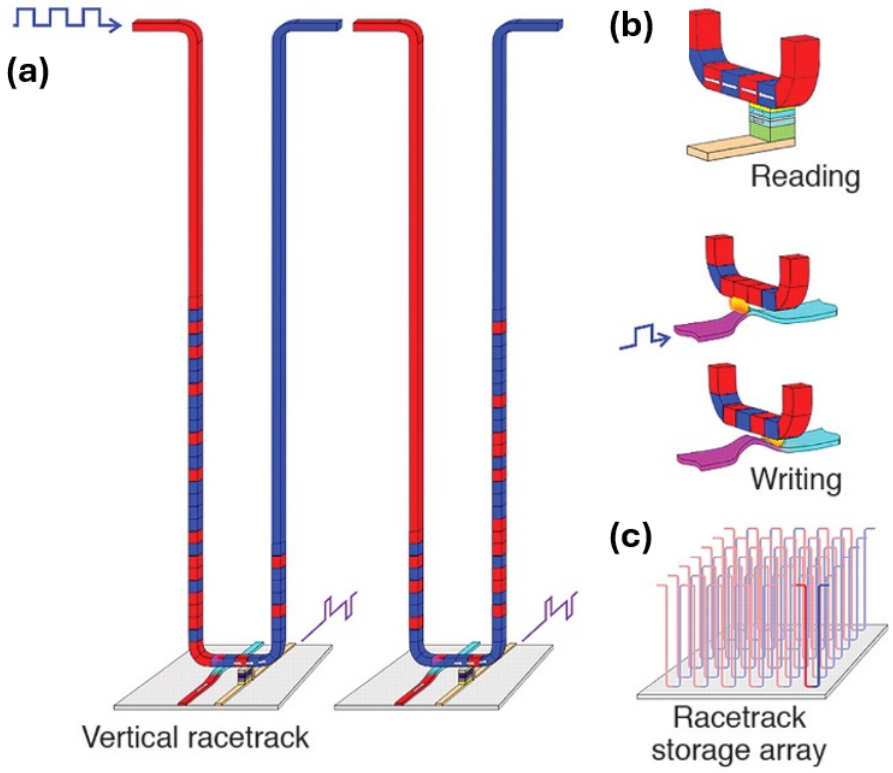

Figure 1.1. RM diagram. (a) Magnetic domain movement in RM. Electrical pulses can be applied to shift the magnetic domains along the RM, and the magnetic state of each domain is read by a tunnelling magnetoresistive junction. (b) Read/write circuitry, using a magnetic field created by an electrical current to change the alignment of a magnetic domain. (c) Scaling to a complete data storage device. Reproduced with permission from [10].

1.2. Ferromagnetism on the nanoscale

All physical phenomena that will be relevant, including the very existence of solid matter, can be explained by the quantum mechanical observation that electrons behave as waves that interact both with electromagnetic fields and with one another. Inside atoms, electrons carry quantised amounts of energy, angular momentum, and charge, and due to the Pauli exclusion principle, every electron must be unique [16]. Due to quantisation and exclusion, electrons must occupy specific orbitals unique to each chemical element. Therefore, if the atoms in a material show long-range order, the electronic properties will also be consistent over extended length scales. Ferromagnetism is a special case (occurring due to exchange interaction) when the sum angular momentum of electrons in atom orbitals is non-zero, thus creating a magnetic moment, and the moments of nearby atoms align towards one direction. This is typically observed in transition metals,

including cobalt (Co) and iron (Fe), which can form permanent magnets. The emergent nanoscale behaviour in ferromagnetic materials can be modelled by considering the energy associated with configurations of atomic magnetic moments. The main contributions to the energy associated with one magnetic moment ($\boldsymbol{m_i}$) are

$$E_i = E_{exchange} + E_{demag} = -\sum_j J_{ij}\ \boldsymbol{m_i} \cdot \boldsymbol{m_j} - \mu_0\ \boldsymbol{m_i} \cdot \boldsymbol{H}_{demag}. \tag{1.1}$$

Where J_{ij} is the exchange constant, μ_0 is the permeability of free space, and ($\boldsymbol{H}_{demag}$) is the net magnetic field created by all magnetic moments in the material [17], given by

$$\boldsymbol{H}_{demag}(\boldsymbol{r}) = \frac{1}{4\pi}\sum_i \frac{3\boldsymbol{r_i}(\boldsymbol{m_i} \cdot \boldsymbol{r_i}) - \boldsymbol{m_i}}{r_i^5}. \tag{1.2}$$

Where r is a point in space, and $\boldsymbol{r_i}$ is a distance vector pointing from the position of $\boldsymbol{m_i}$ to r. A ferromagnetic sample is considered to be in a stable configuration if the total energy of all moments, $E = \sum_i E_i$, is minimal [17], which requires a trade-off between all energy terms. Exchange energy corresponds to the interactions between electrons in neighbouring atoms, which favours parallel alignment of spins in ferromagnetic materials. Demagnetisation energy corresponds to magnetic moments interacting with $\boldsymbol{H}_{demag}$, which depends strongly on sample geometry. This energy term often favours long-range $\boldsymbol{m_i}$ configurations that create a weak $\boldsymbol{H}_{demag}$, such as vortices. The magnetic configurations of many ferromagnetic nanostructures are accurately described by the competition of interactions between neighbouring atoms and magnetic fields created by the whole system [18]. Note, that the underlying theory presented here will be revisited and expanded upon in later chapters when experimental results requiring further theory are presented.

Based on the principle of energy minimisation, simulations can be developed that can predict stable configurations in ferromagnetic nanostructures. By expressing magnetic moments as a magnetisation field $\boldsymbol{M} = \frac{\mathrm{d}\boldsymbol{m}}{\mathrm{d}V}$, corresponding to the magnetic moment per unit volume, it is possible to efficiently simulate ferromagnetic samples larger than 1 nm [19]. Additional energy terms representing material-specific properties [20, 21] or interactions with external fields [22] can be added as necessary, and will be discussed in Section 2.7. Based on the consideration of energy states, it is possible to define micromagnetic simulations that model $\boldsymbol{M}$ in ferromagnetic materials and relate the emergent nanoscale behaviour to the underlying quantum mechanical principles [23].

Such simulations form the theoretical basis for designing spintronic devices and validating experimental results, and will be discussed in detail in Section 2.7.

For spintronic applications, the study of ferromagnetism focuses on the formation of magnetic domains in NWs and on mechanisms for controlling the motion of magnetic DWs [24]. Figures 1.2a and 1.2b introduce the types of DWs typically observed in NWs. In planar NWs, which have a thickness to width ratio corresponding to the dashed square in Figure 1.2b, the magnetic configurations are energetically constrained by the low-thickness (typically < 10 nm for NWs fabricated from ferromagnetic metals) and can be described by 2D $\boldsymbol{M}$ distributions. In planar NWs, either transverse DWs (TDW) or vortex DWs (VDW) are typically observed, as shown in the top of Figure 1.2a. When considering a wider range of NW thicknesses, configurations are characterised by 3D $\boldsymbol{M}$ distributions that exhibit both transverse and vortex DW (TVDW) characteristics with the vortex core oriented perpendicular to the long-axis (y in the figure), or a Bloch-point DW (BPDW) with vortex cores oriented parallel to the long-axis forming a point of undefined $\boldsymbol{M}$ [25] as shown in Figure 1.2a. TVDWs propagate along the NW when an external magnetic field ($\boldsymbol{H}$) is applied parallel to the NW long-axis, as shown in Figure 1.2c. This property can be utilised to transmit DWs over ferromagnetic NWs or to study collective spin oscillations, known as magnons. Figure 1.2d shows that a DW propagating above a critical velocity V_m can emit spin waves. The dynamics of DWs and topological DW configurations, such as skyrmions, have been applied to develop stochastic computing devices that accelerate machine learning by non-linearly transforming electromagnetic signals [11, 26]. For comparison, 3D nanostructures, such as tubes, spheres, and Möbius strips in Figure 1.3a, exhibit DWs that are more stable in response to external stimuli and thus more suitable for deterministic computing than their 2D counterparts in Figure 1.3b [27, 28]. This is attributed to asymmetric magnetostatic interactions energetically favouring exotic $\boldsymbol{M}$ configurations in curved 3D geometries [14, 24, 25]. The study of such ferromagnetic nanostructures in 3D is enabled by recent advances in fabrication, characterisation, and computational techniques.

1.3. Characterisation using electron microscopy

In addition to theory, research in nanomagnetism requires methods to characterise the nanostructured materials, as understanding their physical properties is essential for developing novel technologies. Comprehensive magnetic characterisations are possible by

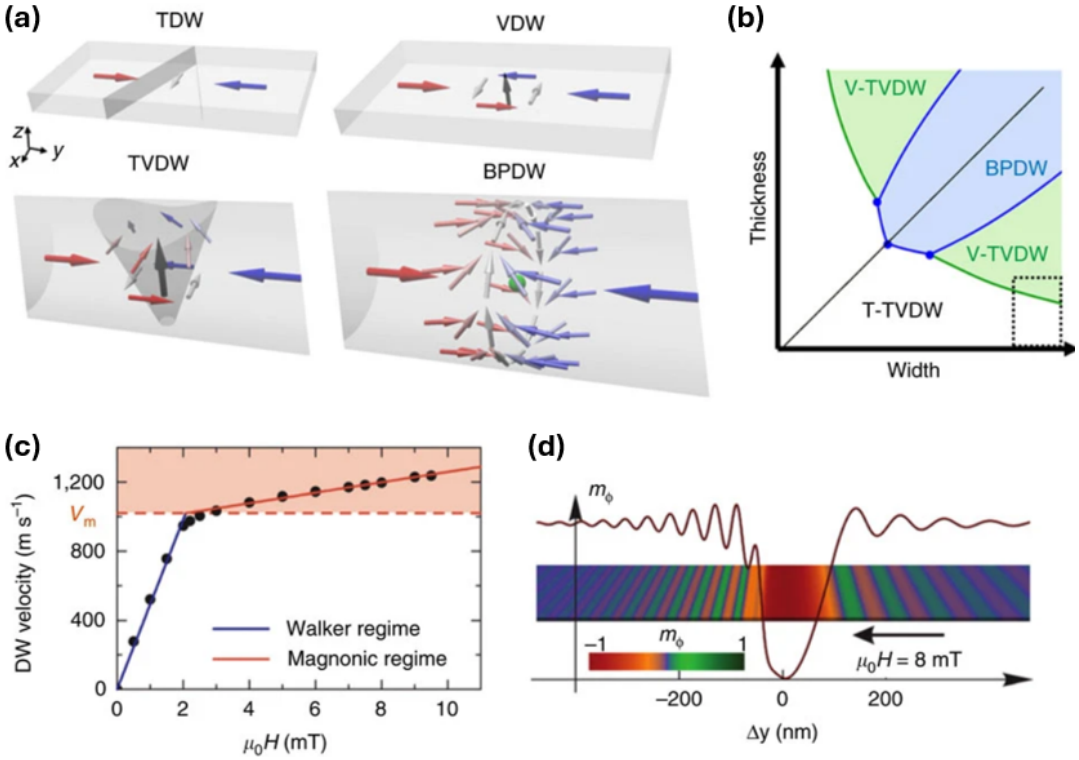

Figure 1.2. Overview of magnetic DWs in ferromagnetic NWs. (a) $\boldsymbol{M}$ configurations in common DW types, showing TDW and VDW features in thin nanoscale strips (top), and TVDW and BPDW textures in 3D NWs (bottom). (b) Schematic diagram showing the correlation between DW types and NW dimensions. (c) Velocity of a TVDW propagation as a function of applied $\boldsymbol{H}$ field strength. (d) Azimuthal component of magnetic moments in a simulation of DW propagation in the magnonic regime. In non-planar NWs, Magnetic DWs form vortex-like magnetic configurations that can be propagated by applying an external magnetic field. Reproduced with permission from [24].

probing the sample using beams of light [29], neutrons [30], X-rays [31], or electrons [1]. Electron-based techniques stand out due to their small size and strong interactions with materials. When an electron is accelerated by a 100 kV electrostatic potential, its velocity is more than half the speed of light, and it exhibits a relativistically corrected de Broglie wavelength of 3.7 pm. As a result, electron wavelengths are small enough to resolve electromagnetic fields and subatomic particles between atoms, allowing fundamental physical properties to be characterised by analysing the statistics of signals collected in electron microscopes. Figure 1.4 shows the range of useful signals that are produced when an electron beam interacts with a thin (typically < 200 nm) sample [32]. High-energy incident electrons can scatter in all directions, with a probability distribution dependent on the atomic structure of the material. Scattering transfers energy to the

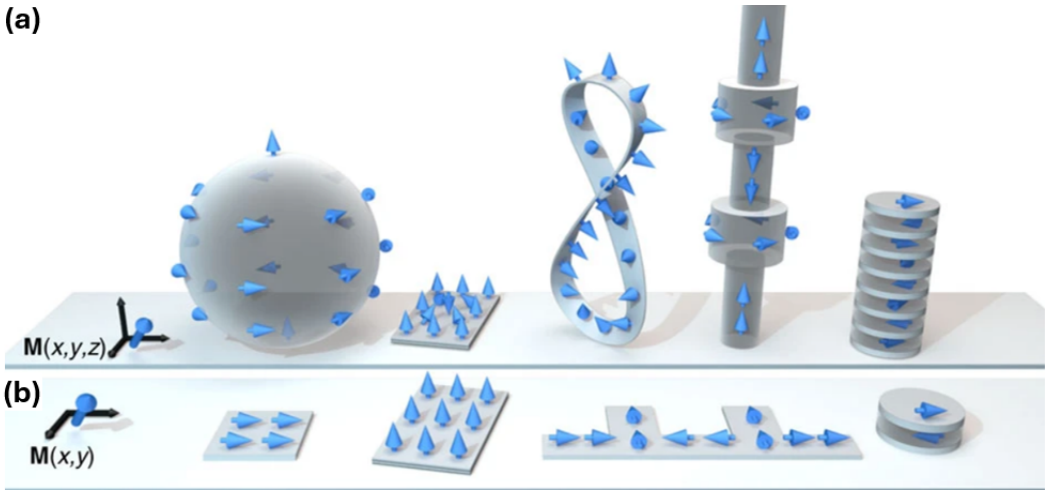

Figure 1.3. Schematic comparing examples of 3D (a) and 2D (b) nanostructure geometries. Blue arrows indicate the $\boldsymbol{M}$ distributions. Curved 3D surfaces exhibit novel magnetostatic interactions that have not been observed in 2D nanostructures. Spherical surfaces exhibit chiral magnetic configurations that are stable at room temperature; thick films exhibit internal variations; and cylinders switch between longitudinal and transverse alignment depending on diameter. Reproduced with permission from [24].

material, exciting atoms and causing them to emit both X-rays and low-energy secondary electrons (SEs), dependent on the electronic structure of the atoms. Since electrons carry charge, their movement can result in the flow of electrical currents in the sample or collective oscillations called plasmons [33]. Additionally, the electron beam can ionise gas molecules in a near-vacuum, causing them to chemically erode the sample or deposit new material [34]. Using dedicated instruments (discussed in Chapter 2), these signals can be detected to characterise the atomic structure, elemental composition, and electronic properties of the material, but the most precise quantitative measurements require analysis of the transmitted beam as well.

Transmitted electrons scatter elastically or inelastically. Elastically scattered electrons are typically coherent and show interference effects when detected. They can be described using wave optics and modelled as wavefronts diffracted by electromagnetic fields created by atoms in the sample, which underpins coherent TEM techniques, such as electron crystallography and electron holography [32] (discussed in Chapter 2). For comparison, inelastically scattered electrons lose energy, thereby increasing their wavelength and causing decoherence. Hence, coherent TEM techniques are only applicable if a sufficient elastic signal can be detected. The electron inelastic mean free path (IMFP) is the average distance an electron can travel in a material before scattering inelastically, and

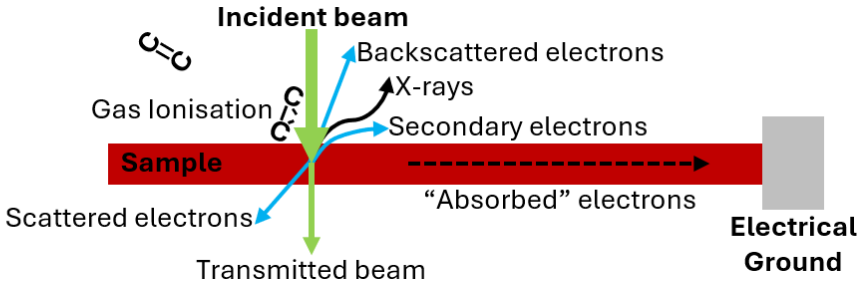

Figure 1.4. Signals that are detected when an electron beam interacts with an electron-transparent sample. Electrons can transmit elastically or inelastically. Inelastic scattering transfers energy to atoms in the material, thereby inducing the emission of photons and electrons from the irradiated volume. Additionally, irradiation of volatile molecules can incite chemical reactions.

is $\sim$100 nm for 100 kV electrons in most materials [35]. Figure 1.5 shows measurements and theoretical models of IMFP as a function of electron energy relative to the Fermi level (typically < 20 eV) in elemental solids [36]. Conventionally, material samples are considered electron-transparent if their projected thickness is less than the IMFP for the material, indicating that coherent TEM signals can be collected efficiently. In this thesis, both coherently transmitted electrons and inelastically generated SEs are utilised for sample fabrication and characterisation.

1.3.1. Lorentz transmission electron microscopy

A TEM is a specialised instrument used to characterise materials below the atomic scale by analysing an electron beam transmitted through an electron-transparent sample [32]. Transmitted electrons are often coherent, and by relating to quantum mechanics, they can be described by charge-carrying wave-functions $\Psi = ae^{i\varphi}$. The amplitude a and phase φ of the plane wave are affected by quantum-mechanical interactions between the electron and the atoms in the sample [37]. Modern, aberration-corrected TEMs frequently achieve atomic resolution and can be used to study inter-atomic interactions affecting individual atomic columns [38]. Magnetic interactions can be characterised by mapping the projected magnetic vector potential [39], but this requires specialised TEMs.

A Lorentz TEM (LTEM) is dedicated to measuring electromagnetic potentials and holds the sample in an environment free of external magnetic fields [28]. Named in honour of H. A. Lorentz, LTEMs are used to quantify electromagnetic fields that interact

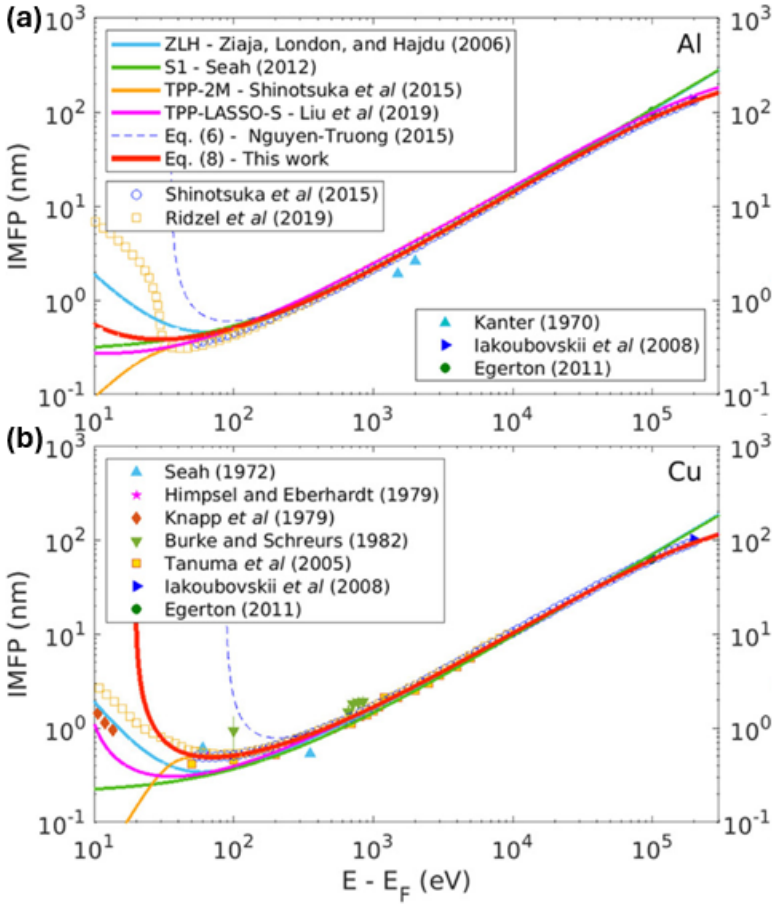

Figure 1.5. IMFPs for (a) Al and (b) Cu. Points and lines correspond to experimental data and theoretical functions, respectively. Theoretical predictions and experimental measurements of IMFP are in good agreement for electron energies above 1 kV, and predict $\sim$100 nm IMFP for typical TEM beam energies in the 100 kV range. Reproduced with permission from [36].

with transmitted electrons via the Lorentz force [40], given by

$$\boldsymbol{F} = q_e(\boldsymbol{E} + \boldsymbol{v} \times \boldsymbol{B}). \tag{1.3}$$

Where q_e is the electron charge, $\boldsymbol{E}$ is the electrostatic field, $\boldsymbol{v}$ is the electron velocity, and $\boldsymbol{B}$ is the magnetic induction. Although the Lorentz force offers a qualitative description of electron deflections in TEM, scattering from electromagnetic potentials is quantitatively described by the quantum-mechanical Aharonov-Bohm effect on φ [41], which will be discussed in Section 2.6. This is used to characterise functional nanostructures that exhibit or utilise electromagnetic fields, such as components in electronics and spintronics [42]. Theoretically, an LTEM can be used to characterise all relativistic quantum fields that

feature in Maxwell's equations [1, 41], but this work focuses on magnetic moments and magnetic induction in spintronic device prototypes.

LTEM techniques sensitive to $\boldsymbol{B}$ include Fresnel imaging, differential phase contrast (DPC), and electron holography [43]. When the electron beam transmits through a $\boldsymbol{B}$ field created by a material sample, the beam will be deflected by a Lorentz force according to Equation 1.3. Fresnel imaging is a technique for detecting magnetic DWs in thin films, in which the sample is illuminated with a parallel electron beam and bright or dark lines are detected when magnetic domains deflect the beam around the DW, causing the beam to locally converge or diverge when defocused. When the electrostatic fields and inelastic scattering in the sample are negligible, the magnetic contrast can be modelled numerically using the "transport-of-intensity" equation [44]. Quantitative measurements of projected $\boldsymbol{B}$ are more reliably acquired using DPC, which detects deflections of a convergent beam, as shown in Figure 1.6. The Lorentz force deflects the transmitted beam away from the beam axis, thereby shifting the illuminated spot on the detector off-centre. The detected spot shift can be calibrated to quantify the average Lorentz force acting on the beam [45, 46]. The mathematical description of DPC is consistent with the leading theory based on the Aharonov-Bohm effect on the electron wave phase, but is sensitive to the gradient of φ. Off-axis electron holography is a technique that utilises the interference of two electron beams to reconstruct φ directly [37]. Holography is the preferred technique for imaging 3D nanostructures because the direct φ reconstruction is affected less by non-magnetic forces that can introduce uncertainty to DPC [47].

Magnetic characterisation of 3D nanostructures benefits from the use of tomographic techniques for 3D imaging and reconstruction, such as electron holographic vector field tomography (EH-VFT) [1, 48]. Figure 1.7 introduces the acquisition method for EH-VFT datasets, which requires a 360°rotation of the sample around two orthogonal axes and the acquisition of electron holograms at $< 10°$ intervals. Phase reconstruction from holograms, including requirements for the electron biprism and reference wave, will be discussed in detail in Section 2.6. By modelling φ signals created by a 3D object, EH-VFT has been used to reconstruct the 3D distributions of electrostatic potential (V) and $\boldsymbol{B}$ with 10 nm spatial resolution, enabling the observation of 3D geometry-dependent variations in electromagnetic fields created by the sample [49]. In combination with electromagnetic simulations, the 3D $\boldsymbol{B}$ reconstruction has enabled the derivation of local variations in micromagnetic material properties, such as J_{ij} from Equation 1.1 [48]. The reconstruction and analysis of 3D datasets are underpinned by computational optimisation techniques, which enable large-scale data processing and are extensively employed in this thesis.

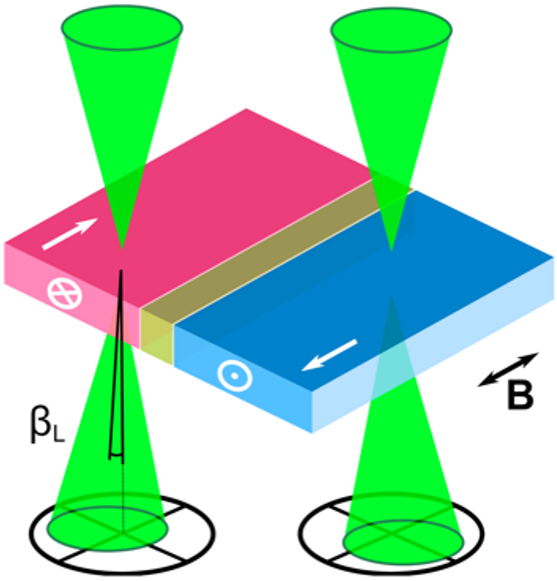

Figure 1.6. Illustrative DPC diagram. The electron beam is deflected away from the central axis by $\boldsymbol{B}$. The deflection angle (β_L) is reconstructed by measuring the shift of the illuminated spot on the detector and is indicative of the average $\boldsymbol{B}$ in the beam path. Reproduced with permission from [45].

1.4. Cost function minimisation

Electron microscopy encompasses a range of techniques that can comprehensively characterise nanostructure composition and physical properties, but analyses often must be automated to handle the volume of data. When applying the LTEM techniques introduced above, terabytes of data can be generated during experiments, which requires efficient use of computational resources and development of processing algorithms.

As computers are utilised for data analysis, many analytical procedures depend on the underlying technique of cost function minimisation. Given a scalar cost function $c = c(x_1, ..., x_n)$, it solves the problem of finding parameters $(x_{*1}, ..., x_{*n})$ that correspond to the minimum value of c [50]. For example, minimisation is used in micromagnetic simulations to find magnetic configurations corresponding to minimum energy, or in least-squares fitting to refine parameters in a theoretical model $f = f(x_1, ..., x_n)$, such that the differences between the measurements y_i and the predictions f_i are minimised by using a cost function

$$c = \sum (y_i - f_i(x_1, ..., x_n))^2. \tag{1.4}$$

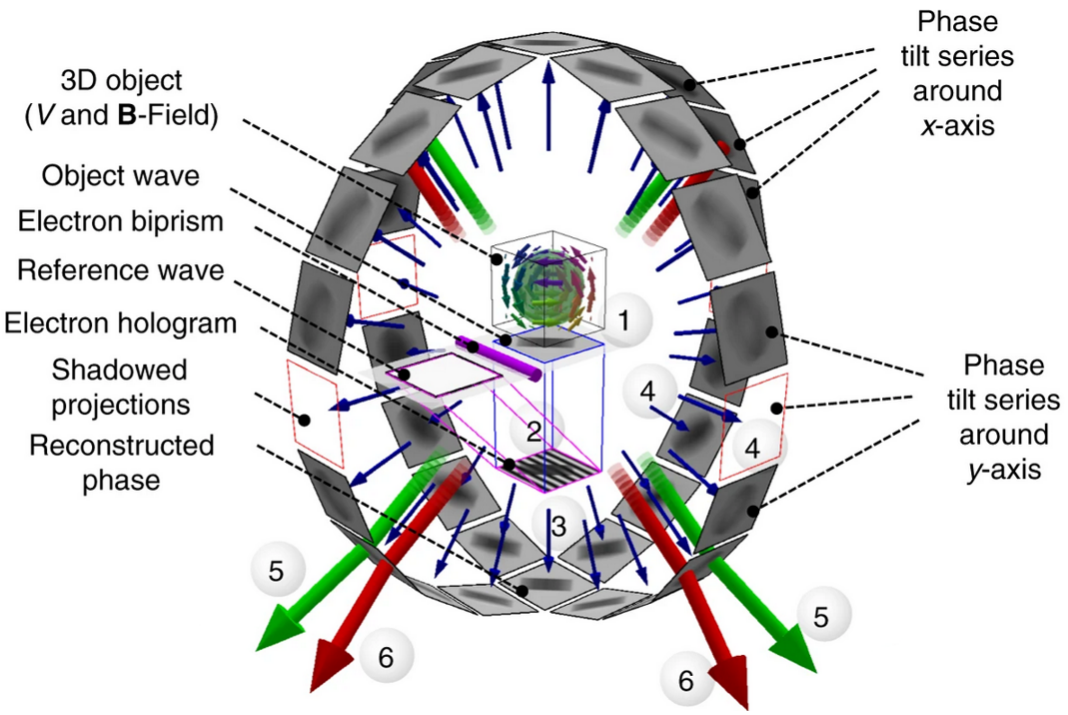

Figure 1.7. Schematic diagram of EH-VFT. 1) Electron waves pass through the sample represented by the V and $\boldsymbol{B}$ fields. 2) Electron holograms are formed on the detector. 3) Maps of φ are reconstructed. 4) Rotating the object and recording holograms around two tilt axes, x and y, provides a 360° tilt series of φ maps for each tilt axis. 5),6) Computed tomography (CT) is used to reconstruct V and $\boldsymbol{B}$ in 3D. EH-VFT enables comprehensive electromagnetic characterisation of nanostructures. Reproduced with permission from [48].

Minimisation problems can be solved using three main types of approaches, namely, analytical solutions, non-gradient iterative algorithms, and gradient-based iterative algorithms. Since the minimum of $c(x_1, ..., x_n)$ is at a point where the gradient $\nabla c = 0$, the minimum can sometimes be found by analytically solving the system of equations $\{\frac{\partial c}{\partial x_1} = 0, ..., \frac{\partial c}{\partial x_n} = 0\}$. Analytical solutions are fast and precise for simple functions such as linear regression, but for functions with many parameters, it is much faster to compute good iterative approximations [51]. Non-gradient iterative methods approximate the minimum by evaluating c at many different points and choosing the lowest value. Grid search is an example of a "brute force" method that sets bounds for all parameters, represents all possible combinations of $(x_1, ..., x_n)$ values as a grid, and evaluates c for all combinations. For comparison, more sophisticated algorithms consider $(x_1, ..., x_n)$ to be coordinates of a multi-dimensional "parameter space", where each set of coordinates corresponds to a point with an associated value c, and the minimisation problem is rephrased as a search for the point with lowest c. Powell's algorithm [52] is an example,

which does not require bounds, but starts the search at a specified point. The search is implemented by varying one parameter at a time to evaluate c at multiple points, taking a step to a point with a lower c value, and then varying the next parameter to determine the next point. At each iteration, the value of c is reduced until a point is found where changing any of $(x_1, ..., x_n)$ no longer reduces the value of c. The benefit of these non-gradient-based algorithms is their reliability, finding a minimum for any cost function with a real-number value; however, faster algorithms can be defined for well-behaved, differentiable functions. The conjugate gradient (CG) method is the standard for large least-squares problems, and it functions by taking steps from a starting point towards the direction of decreasing ∇c, whilst making sure that each step is in a direction conjugate to previous steps [53]. This ensures that each step preserves the reduction of c value gained from previous steps. If the analytical expression for the gradient is known, the CG method needs to evaluate c and ∇c fewer than $n + 1$ times to find the minimum of a quadratic function. Alternatively, if the gradient is approximated numerically, c must be evaluated a number of times proportional to n^2. Further algorithm optimisations are possible for non-quadratic functions [54], but the computation time required for CG minimisation is often most significantly improved by optimising c to compute faster, rather than altering the algorithm. Regarding uncertainty, the discussed iterative methods can, theoretically, find a local minimum of c with precision equal to the numerical precision of the computer. In practice, minimisation is performed multiple times from a few starting points to detect if multiple minima are present, and to save time, algorithms are terminated when the reduction in c per iteration slows below a user-defined threshold. In summary, cost function minimisation is performed during micromagnetic simulations or when fitting functions to experimental data, and by choosing the best algorithm for each problem, computations that may take years with pen-and-paper are executed in seconds.

1.5. Combined applications

Research in ferromagnetism and the development of specialised magnetic characterisation techniques have often been driven by the potential to harness magnetic material properties in computing applications. Theoretically, readily available materials such as Fe can encode one bit of data in a magnetic domain smaller than 100 nm in all dimensions, the data can be stored for decades, and by applying external stimuli, including electrical current or magnetic fields, the bits can be read, written or deleted by physics-based randomisation [55]. If integrated with existing technologies, this could address many

limitations of computer hardware, such as data storage density, volatility, absence of true randomness, and reliance on rare-earth metals [6]. However, to achieve this, the technology to fabricate functioning devices must be developed, which requires dedicated fabrication techniques and a comprehensive understanding of the properties of the ferromagnetic material. LTEM has been instrumental in this and has been developed historically to meet the challenges of characterising spintronic device prototypes as they increased in complexity. Early works focused on investigating magnetic domains in thin ferromagnetic films [56]. This led to the characterisation of films with magnetic domains on 100 nm length scales [57], and to the design of functional 2D NWs that control the types of domains and DWs that can form by altering the NW geometry [58, 59]. Further works investigated how DWs can be manipulated by using magnetic fields that apply torque to magnetic moments [60], applying electrical currents to rotate moments via spin transfer torque [61, 62], or structural deformations caused by localised thermal expansion [63]. Based on the knowledge gained from such experiments, a design was proposed for a device based on 3D RM [10], which could combine the benefits of non-volatility, storage density, and material availability. Such a device has not been realised at the time of writing, but 3D fabrication techniques for functional ferromagnetic materials [64, 65] and methods for tomographic LTEM imaging & reconstruction that can be used to characterise prototypes [48] are being developed. With ever-increasing use of computational resources for AI and big data, research into ferromagnetic materials that may reduce the environmental impact of computers by addressing key hardware limitations is growing in significance. Some of the most promising device designs require the development of dedicated 3D prototyping techniques, which can be based on electron microscopy.

Recent work has investigated magnetic configurations at connections between ferromagnetic 3D NWs [66]. FEBID has been used to fabricate NW networks that exhibit switching of magnetic states with applications in data storage, which is influenced by the topological configuration of the NW system [64, 67]. Figure 1.8 shows the magnetic characterisation of a 3D NW lattice element, which can be switched between multiple $\boldsymbol{M}$ configurations and exhibits the formation of magnetic DWs with vortex-anti-vortex pairs [68]. Topologically non-trivial $\boldsymbol{M}$ configurations are expected based on simulations shown in Figures 1.8b-d, but their existence is not explicitly confirmed by LTEM characterisation that is sensitive to 2D projections of $\boldsymbol{B}$, shown in Figures 1.8e-g. Previous works have used EH-VFT to comprehensively characterise 3D nanostructures by reconstructing $\boldsymbol{B}$ in 3D, which was used to constrain micromagnetic simulations [48, 49, 69]. In this thesis, an EH-VFT method is developed to reconstruct the underlying 3D $\boldsymbol{M}$ that

is consistent with $\boldsymbol{B}$, thus enabling direct comparison between data and micromagnetic theory.

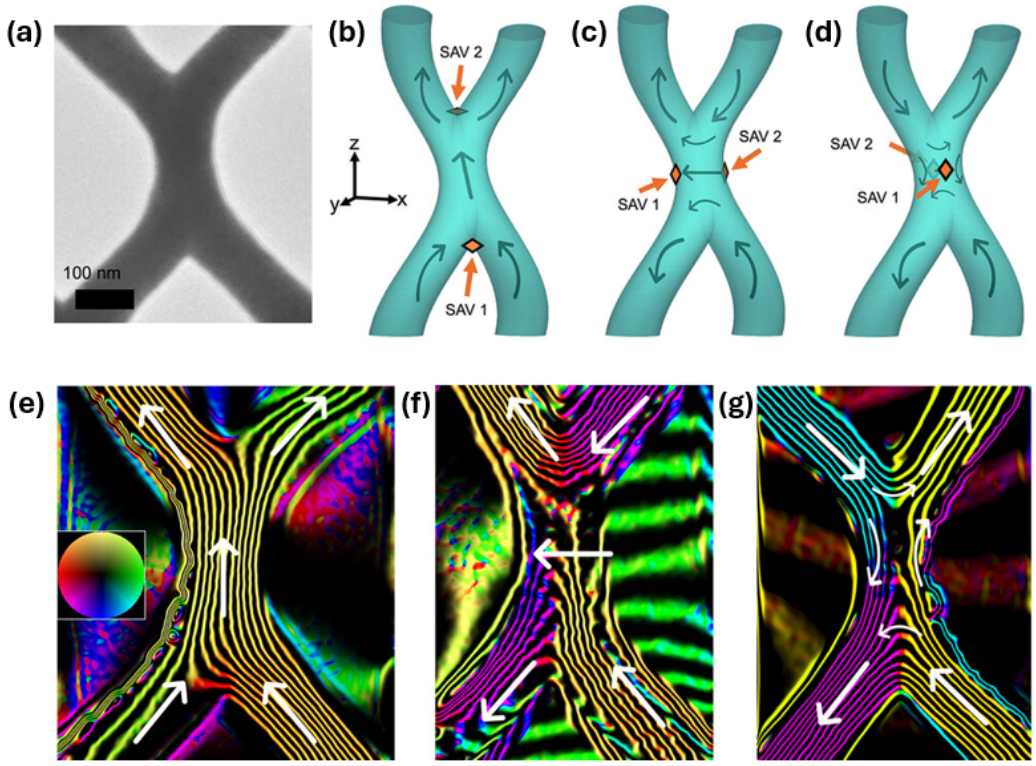

Figure 1.8. Magnetic states in a 3D NW junction. (a) TEM image of a free-standing NW. (b-d) Schematic depictions of $\boldsymbol{M}$ configurations predicted by micromagnetic simulation. The orange diamonds indicate the location and number of surface anti-vortices (SAV). (e-g) Magnetic induction contour maps, acquired using off-axis electron holography. The inset colourmap shows the direction of projected $\boldsymbol{B}$, and white arrows indicate the expected direction of $\boldsymbol{M}$. Conventionally, ferromagnetic nanostructures are examined through the combined use of LTEM and micromagnetic simulations. Reproduced with permission from [68].

1.6. Scope of this thesis

The focus of this thesis is the development of electron microscopy methods for the fabrication and characterisation of ferromagnetic 3D nanostructures.

Chapter 1 has introduced the core underlying concepts. The recent history of nanomagnetism research is summarised, and the novelty of extending 2D fabrication methods to 3D is discussed. A practical description of nanoscale ferromagnetism and statistical methods required to employ the theory are then introduced.

Chapter 2 introduces standard electron microscopy techniques that are applied in this work. A nanofabrication method based on FEBID is presented. The working principles of electron microscopes are summarised, and methods for interpreting amplitude contrast, phase contrast, and spectroscopy are shown. A comparison is made between the electron-optical alignments required for TEM, scanning TEM (STEM), off-axis electron holography, and SEM. Methods for counting atoms in a material using STEM electron energy-loss spectroscopy, and reconstruction of the electron wave phase using off-axis electron holography are discussed in detail.

Chapter 3 discusses the optimisations of the FEBID NW fabrication method. It is observed that vertical NWs create stronger magnetic fields than angled NWs. FEBID can be used as a 3D printing method to create bespoke 3D arrangements of ferromagnetic NWs, but for applications in spintronic devices, it would be preferable if NWs were consistently magnetic regardless of geometry. A study of how the deposition parameters affect the composition and magnetisation of angled NWs confirms that the depth of electron-beam penetration during deposition strongly influences their chemical composition. The higher stability of the precursor gas molecule and limitation of the penetration depth enable the fabrication of NWs with consistent material properties.

Chapter 4 describes the development of a method for reconstructing magnetisation in 3D, by using tomographic off-axis electron holography. Tomographic reconstruction is implemented using MBIR. Improvements to automated tomographic alignment and distortion correction algorithms are implemented, which enable the first successful experimental reconstruction of magnetisation in electron microscopy. The MBIR method is tested using a free-standing Co NW, and the results are compared with previous X-ray based reconstructions and with the expected magnetisation values for the material. The reconstruction is found to be accurate, and the software algorithms are identified as the primary limitation for precision.

Chapter 5 investigates the statistical performance of MBIR through testing on simulated datasets. The mathematical expression of MBIR is presented, and relevant optimisations are discussed. The accuracy of the algorithm is tested on idealised simulated datasets by purposely introducing artificial flaws to quantify reconstruction errors. The effects of a limited sample rotation range are measured to evaluate numerical uncertainty in the reconstruction. The sample surface is found to acquire the largest errors for an incomplete tomographic tilt series. Systematic errors for reconstructing divergent magnetic configurations are evaluated. Some magnetic moment distributions are inherently invisible to LTEM analysis, regardless of sample orientation. These include the cores of

Néel DWs and Bloch points, which are simulated and whose signatures in magnetisation reconstructions are discussed. Overall, spatial resolution is determined as a valid measure of the smallest features that can be interpreted quantitatively, and the reconstruction is shown to be sensitive only to features that produce detectable signals.

Chapter 6 summarises the work described in the thesis and discusses future developments in 3D nanofabrication and nanocharacterisation techniques.

Chapter 2.

Instrumentation and Methods

"If I have seen further, it is by standing on the shoulders of giants."
— Isaac Newton, 1675

2.1. Introduction

Electron beams are highly versatile probes for studying materials from the nanoscale to below the atomic scale. Considering that many material properties, such as the binding of atoms into a solid; conduction; creation of magnetic fields; and absorption of electromagnetic radiation; are facilitated by the electrons in a material, much can be learned about materials by observing their electrons. Since electrons interact with each other, an electron beam directed at a material will be altered by the electrons in its path. Electron microscopy is a branch of science that develops methods for characterising materials down to the atomic-scale. Current technologies have advanced to the extent that individual atomic columns can be easily observed, the number of atoms in the beam path can be counted, and electromagnetic fields can be measured [70]. In this thesis, electron microscopes are used to fabricate samples, characterise their atomic composition, and measure their magnetic fields.

2.2. Scanning electron microscopy

An SEM is a highly versatile tool for nanoscale characterisation and fabrication. It operates by scanning the surface of a sample with a focused electron beam and recording the radiation emitted from the illuminated site. The electron beam is formed and controlled by an electron-optical column, shown in Figure 2.1a. The electron source emits electrons into the vacuum by heating the source filament and/or applying a strong electrostatic field that induces quantum tunnelling from the source tip [71]. The emitted electrons are accelerated by applying voltage to the anode, and the condenser lens acts to converge the electrons into a focused beam. The condenser lens achieves this by creating a spatially varying magnetic field that converges electrons, similar to how a glass lens converges visible light. The lensing magnetic fields are often created by electromagnets, which allows the strength of the lens to be varied by altering the current in the electromagnet coils [72]. The lens strength and aperture size determine the beam current, i.e., the number of electrons reaching the sample per second. Scanning is facilitated by electrostatic coils that can control the deflection of the beam in horizontal, orthogonal x and y directions. The objective lens focuses the beam into a fine electron probe on the sample surface.

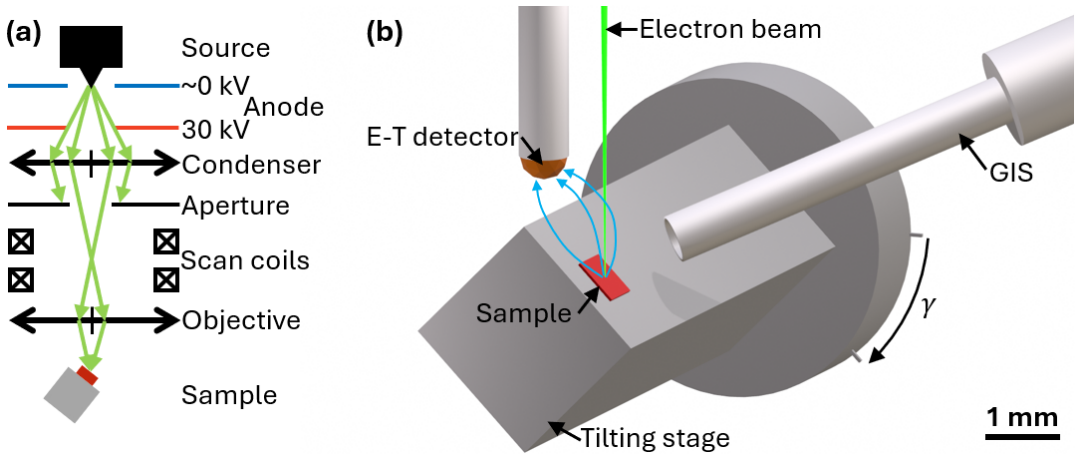

Figure 2.1. SEM operation. (a) Ray diagram of electron beam formation. Electrons are emitted into a vacuum, accelerated by an electrostatic potential difference, and focused with magnetic lenses to form a fine probe on the sample surface. (b) Schematic diagram of the instrumental configuration in the sample chamber. In conjunction with detecting SEs emitted from the sample surface, the sample can be irradiated with an electron beam, tilted, or submerged in a gas.

Detectors that are sensitive to radiation emitted from the high-energy SEM beam-sample interaction site can be positioned above the sample, as shown in Figure 2.1b.

To create an image, a SEM raster-scans the electron beam over the sample and collects the emitted radiation. An Everhart–Thornley (ET) detector [73] is commonly used for imaging and operates by attracting SEs to a positively charged electrode, and produces a signal proportional to the number of SEs collected at each beam position. SEs are generated by the SEM beam ionising the material and have low kinetic energy (< 50 eV), hence are detected from the top ~ 10 nm of the interaction volume, as shown in Figure 2.2a. This imaging mode is particularly sensitive to surface topology, since SEs emitted from the interaction site can be blocked by nearby protrusions [74], as displayed in Figure 2.2b. In combination with a motorised stage, an SEM can be used for tomographic imaging and reconstruction of 3D geometry, based on modelling of the beam path in SE scans [75]. Furthermore, additional equipment can be mounted to the SEM instrument and sample chamber, including a focused ion beam (FIB) to ion-mill the samples, additional detectors for elastically-backscattered electrons or emitted X-rays, gas injection systems (GIS) for depositing new material, or various attachments for *in-situ* experiments [76]. Due to its versatility and ability to map large areas, SEMs are widely used for characterisation and sample preparation of biological, mineral or mechanical specimens. In this work, an SEM with a GIS and a motorised stage, which can tilt the sample by angles $\gamma < 55°$, is used to characterise sample geometries and fabricate ferromagnetic nanostructures (Figure 2.1b).

2.2.1. Focused electron beam induced deposition

Focused electron beam induced deposition (FEBID) harnesses natural chemical processes in an SEM to develop an additive manufacturing method. As shown in Figure 1.4, irradiation by the electron beam can ionise residual or injected gas molecules in the sample chamber, leading to their chemical bonding with the sample. Insufficient vacuum levels often lead to unwanted deposition of hydrocarbon contaminants at the irradiation site [34]. Conversely, the injection of a precursor gas through the GIS, shown in Figure 2.1, alters the local molecular concentrations and allows for purposeful deposition of specific materials. Metal-carbonyls including $Co_2(CO)_8$ or $Fe_2(CO)_9$ are often injected, and disassociate under electron beam irradiation, resulting in metal deposition at the interaction site [65]. On the molecular level, FEBID is a statistical chemical process [78] that deposits the largest volume and concentration of Co or Fe metal in the centre of the irradiation site [42]. By depositing sequentially at a series of successive locations, FEBID can be used to fabricate nanostructures comprising ferromagnetic metals [79]. In this work,

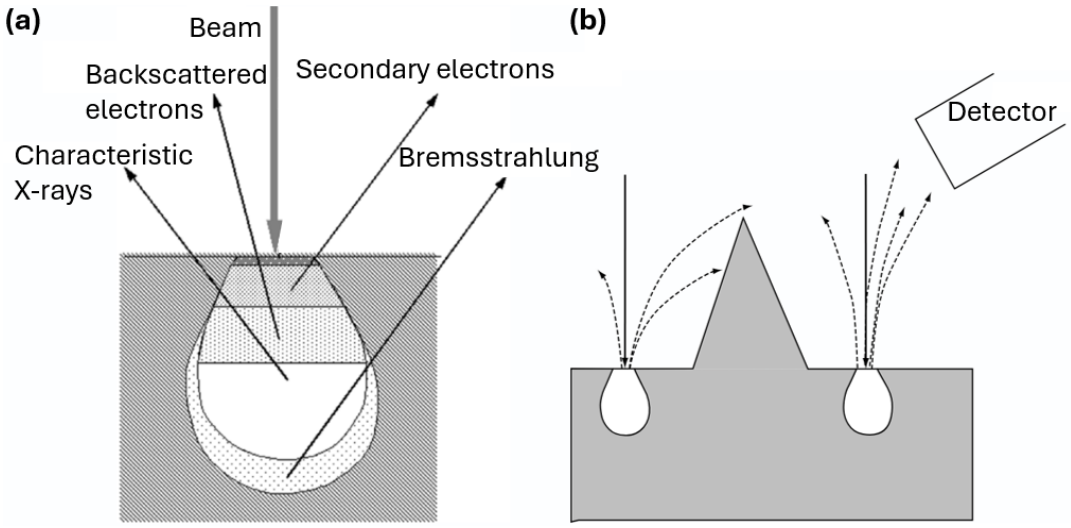

Figure 2.2. Generation and detection of SEs. (a) Schematic diagram showing that electron and X-ray signals are detected from different regions in the interaction volume. SEs can exit the material only when generated within < 10 nm from the surface. (b) Diagram of SE shadowing that results in topographic contrast. Fewer SEs are detected if the interaction volume is shadowed by protrusions on the sample surface. Reproduced with permission from [77]

FEBID is the primary technique for manufacturing ferromagnetic structures, and the fabrication of specific nanostructures is discussed separately for each experiment.

FEBID can be applied to the manufacture of complex 3D nanostructures. When the SEM beam is kept stationary, material is deposited in a column, whereas more complex structures can be deposited layer-by-layer by translating the beam along a predefined path [79]. The range of geometries that can be fabricated using FEBID is comparable to 3D printing [12], as illustrated in Figure 2.3a. Layered deposition has been used to fabricate 3D ferromagnetic NW structures, such as a Co Moebius strip [65], a mixed chirality helix [80], and a helical lattice [66] used to investigate topological formations of 3D spin states. Furthermore, reconfigurable ferromagnetic NW lattices have been manufactured from Co_3Fe to investigate switching dynamics for data storage applications [64, 67]. The geometry of such NW samples is highly reproducible, as shown in Figure 2.3b; however, the elemental composition of the deposited material has been shown to vary [81, 82]. Since 3D spintronic device prototypes can be fabricated using FEBID, achieving uniform composition throughout these structures is essential to ensure consistent and reliable device performance [83]. The material properties of FEBID structures can be tuned by varying the SEM accelerating voltage, beam current, and type of precursor gas [42]. This is discussed in Chapter 3 as part of a study aimed at

improving the consistency of FEBID for fabricating 3D nanostructures with uniform composition.

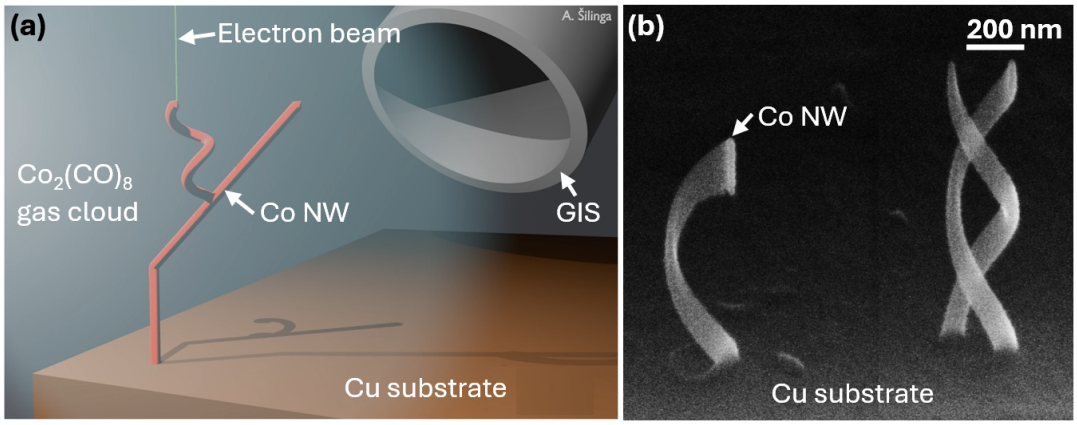

Figure 2.3. FEBID of 3D nanostructures. (a) Model of FEBID fabrication of 3D nanostructures. The SEM beam incites localised deposition of NWs, which can be precisely controlled. (b) SEM image of 3D, helical Co nanostructures. In the presence of an injected precursor gas, the electron beam can be translated to deposit bespoke NW geometries.

2.3. Transmission electron microscopy

TEM is a highly versatile tool for the characterisation of materials from the nanoscale to atomic resolution, with aberration-corrected TEMs resolving atom columns separated by less than 0.1 nm [84, 85]. The working principles of a TEM are similar to those of a visible-light microscope, except that the optical system focuses a beam of electrons instead of a beam of light [86]. As shown in Figure 2.4a, a TEM comprises a point source of electrons, a condenser lens that forms the beam and directs it at the sample, an objective lens that collects both transmitted and scattered electrons to form an image, and a projector lens that magnifies the image and projects it onto a detector. It should be noted that in modern TEM research instruments, each ideal lens in Figure 2.4 corresponds to a system of multiple lenses, apertures, corrective elements, and sometimes additional detectors, which are required to limit aberrations and achieve performance comparable to an ideal lens [72].

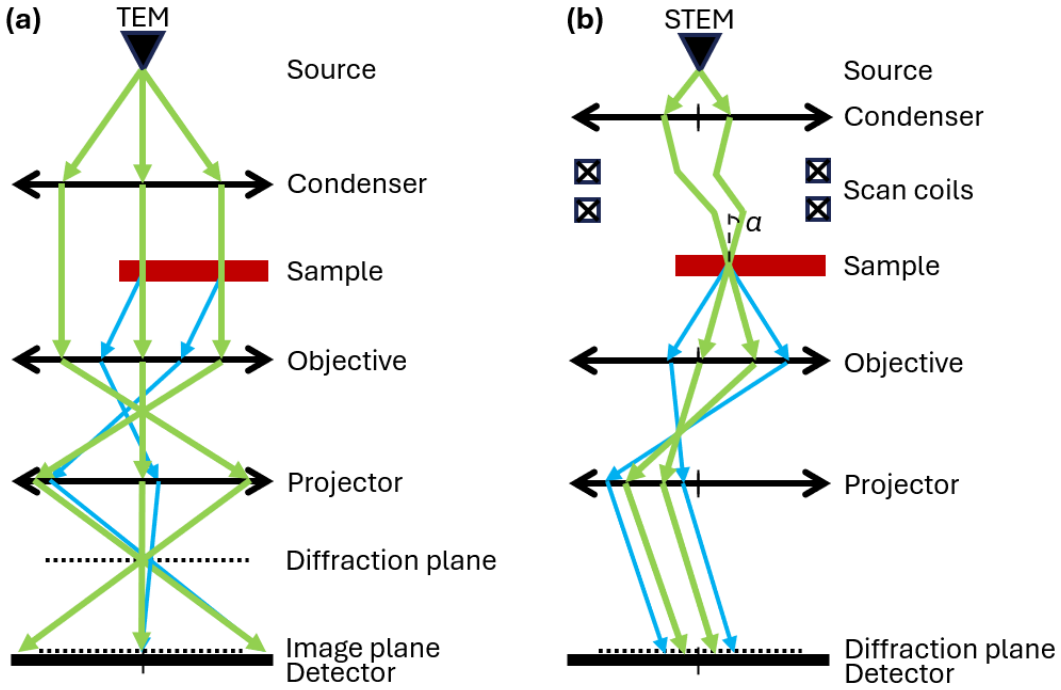

Figure 2.4. (S)TEM ray diagram. (a) Parallel beam in TEM mode. (b) Convergent beam in STEM mode. The directly transmitted beam is shown in green, and the diffracted beams are shown in blue. Electrons that interact with the sample are focused to either form images or diffraction patterns on the detector.

2.3.1. Electron sources

TEM electron sources are similar to those used in SEMs (Figure 2.1a), but are optimised to achieve improved beam coherency necessary to measure electron interference effects, and function at accelerating voltages in the 10 kV to 1000 kV range to increase the IMFP and enable transmission through material samples. Early TEMs used tungsten (W) filaments that emit electrons across a broad energy range when heated to $\sim$3000 °C, but they have since been replaced by field-emission guns (FEGs). An anode can be used to concentrate an electrostatic field on a W or LaB_6 needle such that electrons in the conduction band tunnel from the FEG tip into the vacuum. Conventional FEG types include Schottky FEGs, which are heated to prevent contaminants in the vacuum from reacting with the needle, and cold FEGs, which achieve a higher-intensity beam but require ultra-high vacuum ($< 10^{-9}$ Pa) to operate. This results in electrons emitted from a volume no larger than 5 nm and with an energy spread less than 1 eV, thus creating a coherent beam ideally suited for TEM imaging [87].

2.3.2. Lenses, apertures, and resolution

According to the Rayleigh criterion for optical systems with circular apertures, the minimum distance at which two sources of radiation can be resolved is limited by diffraction and is given by $r = 0.61\lambda$. The de Broglie wavelength (λ) for electrons accelerated by > 100 kV is such that $r < 3$ pm, but in practice TEM resolution is limited to 100 pm by spherical aberration (C_s) in the lenses [85]. TEM lenses are electromagnets that produce a radially varying magnetic field in the TEM column, which focuses the electron beam as shown in Figure 2.5a. Such lenses exhibit C_s that results in images of point-like objects being broadened to a diameter d_{img}. Given by

$$d_{img} = 2C_s\beta^3, \tag{2.1}$$

where β is the collection semi-angle of the lens, shown in Figure 2.5b [84]. The resolution limit resulting from C_s can be improved by using apertures to limit β, although doing so reduces beam intensity. Conventionally, TEMs have apertures at the condenser and objective lenses, which control collection angles for optics above the sample and below the sample, respectively. Additionally, C_s can be reduced by using a series of non-radially-symmetric lenses, such as quadrupole and hexapole arrangements of electromagnets, to correct the beam exiting a conventional lens [88]. Equation 2.1 represents the third-order term that is corrected to achieve 100 pm spatial resolution that enables imaging of individual atomic columns in most crystalline materials, but research is ongoing to correct higher-order terms that would enable use of higher β to improve beam intensity by enabling collection of electrons scattered at higher angles in the sample [72]. Whilst spatial resolution describes a system's ability to distinguish between closely spaced objects, the concept of resolution is also applicable to other instruments. For example, energy resolution that describes a spectroscope's ability to distinguish electrons of different energies, which is discussed in detail in Section 2.5.

2.3.3. Electron detection

Quantitative electron detectors use complementary metal–oxide–semiconductor (CMOS) technology, which is underpinned by semiconductor p-n junctions that produce an electrical current proportional to the number of electron-hole pairs generated when irradiating the semiconductor [89]. Some designs use charge-coupled device (CCD) sensors, often similar to sensors found in digital cameras, with an added scintillator

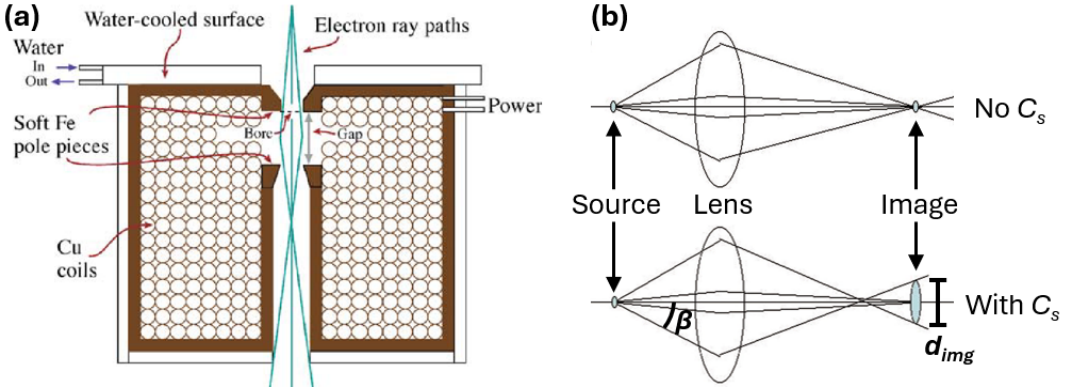

Figure 2.5. TEM lens design and aberrations. (a) Schematic diagram of a TEM lens cross-section. Electrical current flowing through the Cu coils generates a magnetic field that is shaped by the ferromagnetic Fe pole pieces, thereby focusing the electron beam as it passes through the gap. The lens is water-cooled to improve stability. Adapted from [72]. (b) If the lens were ideal, it would converge electrons, producing un-aberrated images (top). Real TEM lenses exhibit C_s, which results in point-source broadening to diameter d_{img}. Reproduced with permission from [84].

layer to convert high-energy electrons into visible light detected by the CCD. Because the scintillator converts each electron into a stream of photons, this can degrade TEM spatial resolution. The advantage is that CCD detectors are available in megapixel configurations, facilitate readout in conventional data formats, and can be fabricated in either square-pixel or ring-shaped geometries, positioned in the TEM beam to record images or around the beam to record scattered electrons, respectively. Alternatively, direct electron detectors (DEDs) have been developed that use radiation-hardened materials to detect high-energy electrons without a scintillator, thereby enabling counting of incident electrons in each pixel [90]. Conventionally, TEMs are equipped with a CMOS pixel detector for imaging, and include additional ring-shaped detectors or beam-stoppers that enable recording scattered electrons with high exposure times without saturating the detector by the central beam.

2.3.4. Reciprocal planes

For the analysis of TEM measurements, the output of these instruments is sufficiently described by the three concepts: resolution, detector type, and reciprocal planes. Reciprocal planes are locations in the TEM column, where electron beams converge to form easily interpretable patterns. If the detector in Figure 2.4a were a pixel detector, the acquired image would be comparable to a magnified photograph of the sample,

because the detector lies in the image plane, where electrons originating from one point in the sample converge to one point on the detector. The reciprocal plane to this is the diffraction plane, where all electrons scattered at a specific angle converge to one point; and if a pixel detector were inserted at this plane, it would acquire a diffraction pattern. Bragg's law defines elastic scattering angles θ_B that exhibit constructive interference when imaging crystals and is given by

$$n\lambda = 2d\,\sin(\theta_B), \tag{2.2}$$

where n is a natural number, d is the crystal plane spacing. In the diffraction plane, distance from the beam-axis is correlated with scattering angle, therefore, bright spots in the detector correspond to θ_B, and crystallography is performed by imaging in this plane. In addition to inserting detectors at different reciprocal planes, it is also possible to insert apertures that filter the electron beam to select specific signals. All subsequent TEM experiments will be described in terms of detector type, the planes in which the detector and apertures are located, and the achievable resolution of the system.

2.4. Scanning transmission electron microscopy

Scanning TEM (STEM) is an imaging method that uses a convergent electron beam. The condenser system shapes the electron beam into a convergent cone that tapers to a precise focal point on the specimen. This geometry is defined by the convergence semi-angle (α), which represents the angle between the optic axis and the outer edge of the cone. The electron beam is rastered over the sample using scanning coils, shown in Figure 2.4b, and the transmitted signal is recorded at each scanned probe position. The scanning coils are often integrated into the condenser system because lenses above and below the coils are needed to fully control the shifting (lateral translation) and tilting (angular deflection) of the beam [86]. Towards the bottom of the electron optics column, STEMs are regularly equipped with an annular dark field (ADF) detector. This ring-shaped detector is positioned in the diffraction plane and produces a signal proportional to the number of electrons scattered at angles larger than α. ADF imaging is a standard technique for qualitative sample characterisation or for aligning other STEM components. Figure 2.6 shows the ADF signal at each STEM probe position on a carbon (C) film with gold (Au) crystallites. Due to their higher atomic number, Au atoms have nuclei with higher charge, which scatter the electron beam at higher angles with more

intensity than the surrounding C film [91]. Additionally, crystal lattice planes are directly visible, indicating that the STEM is aligned sufficiently for atomic resolution imaging. Similar ADF images will be acquired in all STEM experiments to verify resolution and complement the data from other detectors.

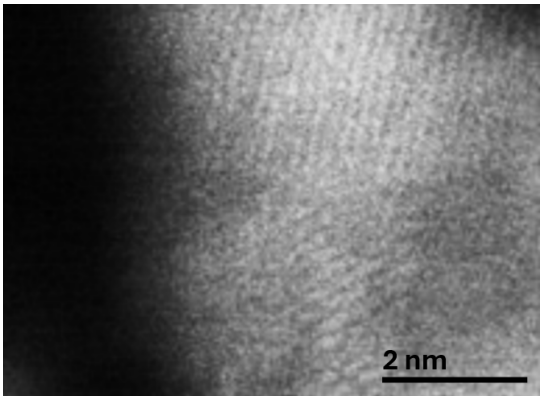

Figure 2.6. STEM ADF image of Au crystallites on a carbon membrane. Crystal planes are visible, indicating that atomic resolution is achieved. ADF imaging of crystals is commonly used to evaluate aberration-corrected STEM alignment.

2.5. Electron energy loss spectroscopy

STEM electron energy loss spectroscopy (EELS) is a powerful analytical technique that can be used to measure the elemental type, quantity, and chemical bonding of atoms in a material. When an electron beam is transmitted through a sample and undergoes inelastic scattering, it transfers a specific amount of kinetic energy to a bound inner-shell electron of an atom. If this energy exceeds the binding energy of the element, the atom becomes ionised and the discrete energy loss corresponds to a direct spectroscopic signature of the element's unique electronic orbital structure [87]. The energy loss can be measured using an electron spectrometer and its operation is shown in Figure 2.7. The spectrometer aperture defines the collection semi-angle, β, and acts as a spatial filter to selectively admit electrons into the spectrometer. The focused convergent beam enters the magnetic prism, where electrons are then dispersed along different paths dependent on their kinetic energy. The magnetic prism creates a $\boldsymbol{B}$ field perpendicular to the beam path, therefore, electrons experience a centripetal Lorentz force that constrains them in

arced trajectories with a radius (r) dependent on their velocity,

$$r = \frac{m_e v}{q_e B}. \tag{2.3}$$

Where m is the relativistic electron mass, v is the electron velocity component perpendicular to $\boldsymbol{B}$, and q_e is the electron charge. The projection optics focus the dispersed beams onto a detector that produces a signal proportional to the number of electrons in each energy channel.

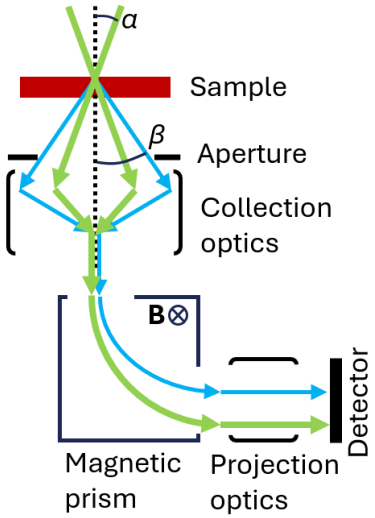

Figure 2.7. Ray diagram of an EELS spectrometer. Green and blue arrows indicate directly transmitted and scattered electron beams, respectively. Transmitted electrons are collected into one beam, deflected by a magnetic prism at different angles dependent on their energy, and the number of electrons in each energy channel is counted by a digital detector. EELS enables the characterisation of inelastic scattering.

To quantify the acquired spectra, the areal density of atoms in the beam path is determined using least-squares fitting [92]. The number of electrons detected per second in the energy window, dE, which underwent inelastic scattering from atoms of type i, is given by

$$I_i(\mathrm{d}E, \beta) = N_i \; \sigma_i(\mathrm{d}E, \beta) \; I_0(\mathrm{d}E, \beta). \tag{2.4}$$

Where N_i is the number of atoms per unit area in the beam path (areal density), I_0 is the number of electrons per second that are incident below angle β, and σ_i is the scattering cross-section for electrons (collected below β) that transmit through type i atoms and lose energy in the range dE. σ_i is computed theoretically using the Hartree-Slater

description of electron waves [93], which predicts energy loss from ionisation of the first two electron orbital energy levels with 5-10 % uncertainty, when compared to known standards [94]. Typically, N_i can be determined by fitting I_i to an experimental EELS spectrum. Figure 2.8 shows the quantitative analysis of a sum spectrum acquired by scanning the STEM beam over a 10 nm x 10 nm square. The Gatan 965 Quantum ER spectrometer was equipped with a Dual EELS system [95] and uses an electrostatic shutter to simultaneously record high-loss and low-loss spectral energies with different exposure times to maximise the signal without saturating the detector. The signal is further increased by summing spectra acquired at multiple nearby probe positions, corresponding to the square in Figure 2.8a. Figure 2.8b shows the zero-loss and plasmon peaks. The zero-loss peak has a full-width at half-maximum (FWHM) of 1.5 eV, indicating that the electron beam comprises electrons of different energies. Additionally, some electrons can scatter multiple times in the material, and to account for this beam-energy broadening, I_i is convolved with the low-loss spectrum (LLS). Figure 2.8c shows the high-loss energy region of the spectrum, where I_i is shown for each atomic element and the plural scattering background is described by an exponential function in each fitting window. After including broadening and background corrections, N_i is determined by least-squares fitting of the function:

$$f_i(\mathrm{d}E) = N_i \; I_0 \int LLS(\mathrm{d}E - x) \; \sigma_i(x) \; \mathrm{d}x + a_i e^{-\frac{\mathrm{d}E}{b_i}} + c_i, \tag{2.5}$$

where N_i, a_i, b_i, and c_i are the parameters determined by least-squares fitting.

In the example spectrum Figure 2.8, the areal densities are $N_C = 1080 \pm 50$ C atoms/nm^2, $N_{Co} = 690 \pm 70$ Co atoms/nm^2, and $N_O = 700 \pm 40$ O atoms/nm^2. The uncertainties correspond to the sum contributions from Poisson noise in the spectrum and systematic uncertainties in the Hartree-Slater cross-section. The analysis is performed with the Gatan elemental quantification software for Digital Micrograph. In this work, spectrometers are set such that $\alpha = 29$ mrad, $\beta = 36$ mrad, and the energy range in each detector channel (called dispersion) is 0.5 eV/channel. These settings are chosen to ensure full capture of the directly transmitted electrons, preserve the fine detail of the spectra, and maintain consistency with previous works [96].

The example EELS quantification was performed on a single region in Figure 2.8a and focused on determining atomic areal densities, which is one of many EELS applications. STEM EELS, combined with automated spectrum fitting, can be used to map composition across large areas by performing repeated analyses at each scanned beam position [97].

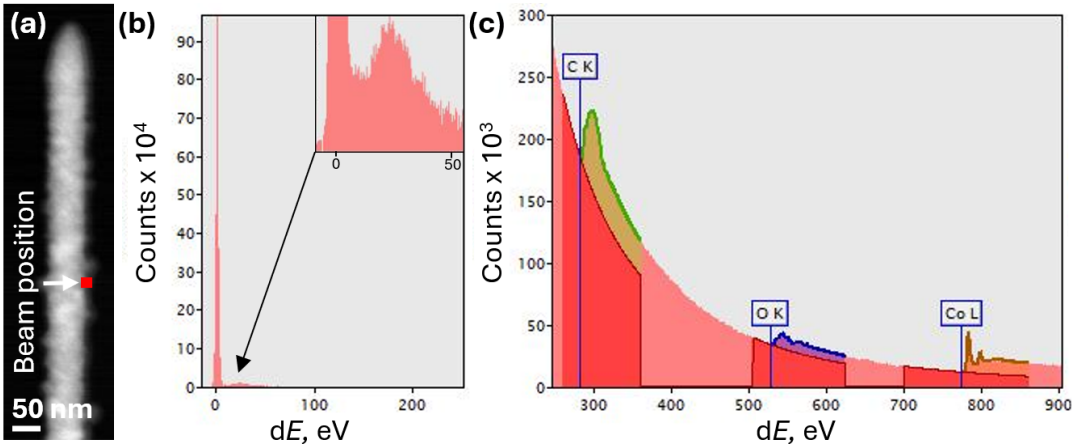

Figure 2.8. Example EELS spectrum quantification. (a) STEM ADF image of an NW, showing beam position during spectrum acquisition. (b) Low-loss energy region of the spectrum, with the inset showing the plasmon peak. (c) High-loss energy region of the spectrum, showing the characteristic energy loss spectra for C, O, and Co atoms. Both the background and the EELS peaks match theoretical functions shown by shaded areas.

Furthermore, since modern STEMs can achieve energy resolution < 1 eV, fine details in the spectra can be used to identify additional signals. The oxidation states of metals have been determined by correlating experimental spectral fine structure with simulated energy-loss near-edge structures (ELNES) models [98]. In the LLS, the plasmon peak ($\mathrm{d}E < 50$ eV) is the result of energy imparted to collective oscillations of weakly-bound electrons in the material, which are the most frequent type of inelastic scattering and are dependent on the dielectric constant of the material. Consequently, analysis of the plasmon resonance peak can provide information on material's optical properties. Since the scattering probability is directly proportional to the sample thickness, it can also facilitate the estimation of the electron IMFP [99]. Furthermore, by attaining a meV energy resolution, it is possible to resolve coupling to thermal vibrations, allowing the precise measurement of local sample temperature [100]. Overall, most mechanisms of inelastic scattering can be studied with sufficient EELS energy resolution and modelling [101]. However, STEM EELS is primarily used to map the atomic composition of nanostructures in this work.

2.6. Off-axis electron holography

2.6.1. Phase contrast

Off-axis electron holography is a wave-optics-based TEM technique that is sensitive to electromagnetic fields. This specialised TEM technique allows for reconstruction of the phase shift of an electron wave and can be used for the nanoscale characterisation of ferromagnetic materials [47]. A coherent electron beam in the TEM image plane is described using wave-optics theory by a wave function

$$\Psi_{img}(x,y) = a(x,y)e^{i\varphi_{tot}(x,y)}. \tag{2.6}$$

Where a is the amplitude, defined such that the beam intensity is $I_{img}(x,y) = a^2$, and the total phase is given by

$$\varphi_{tot} = \int_{path} \boldsymbol{k} \cdot \mathrm{d}\boldsymbol{s}. \tag{2.7}$$

This equation accounts for the total optical phase accumulated by an electron propagating along a path, $\boldsymbol{s}$, with a corresponding wave vector, $\boldsymbol{k}$. The interaction between the electron beam and electromagnetic fields is described by the Aharonov-Bohm effect [41], and can be interpreted as a variation of $\boldsymbol{k}$, such that

$$\boldsymbol{k} = \frac{2\pi\sqrt{2q_e\ m_e(U_a + V(x,y,z))}}{h}\hat{\boldsymbol{s}} - \frac{2\pi\ q_e}{h}\boldsymbol{A}(x,y,z). \tag{2.8}$$

Where U_a is the accelerating voltage, V is the electrostatic potential, h is the Planck's constant, $\boldsymbol{A}$ is the magnetic vector potential, and $\hat{\boldsymbol{s}}$ is the unit vector parallel to the beam trajectory. The integral in Equation 2.7 can be solved easily if the beam is parallel to the z-axis, and both the TEM lens aberrations and beam deflections in the sample are assumed negligible. In that case, the phase shift relative to vacuum $\varphi(x,y) = \varphi_{tot}(x,y) - \varphi_{vac}(x_0,y_0)$ can be expressed as

$$\varphi(x,y) = \varphi_{el} + \varphi_m = \frac{2\pi\ q_e}{h\ v}V_{proj}(x,y) - \frac{2\pi\ q_e}{h}\Phi(x,y). \tag{2.9}$$

Where φ_{el} and φ_m are the electrostatic and magnetic contributions to φ, respectively, V_{proj} is the electrostatic potential projected along the z-axis, and $\Phi = \int_{area} \boldsymbol{B} \cdot \mathrm{d}\boldsymbol{S}$ is the magnetic flux enclosed in the area between the primary beam and the beam in vacuum.

Figure 2.9a shows that φ_{el} at an arbitrary point x_i is defined by the integral of V along the z-axis, $V_{proj} = \int V dz$. Additionally, Figure 2.9b shows that φ_m is defined relative to the beam in vacuum, and used to specify the integral area $\boldsymbol{S}$. Conventionally, the beam in vacuum is chosen to be both infinitely long and far away, such that it is located in a volume without electromagnetic fields present. In summary, equation 2.9 is derived from plane-wave optics and can be used to characterise electromagnetic fields by measuring φ.

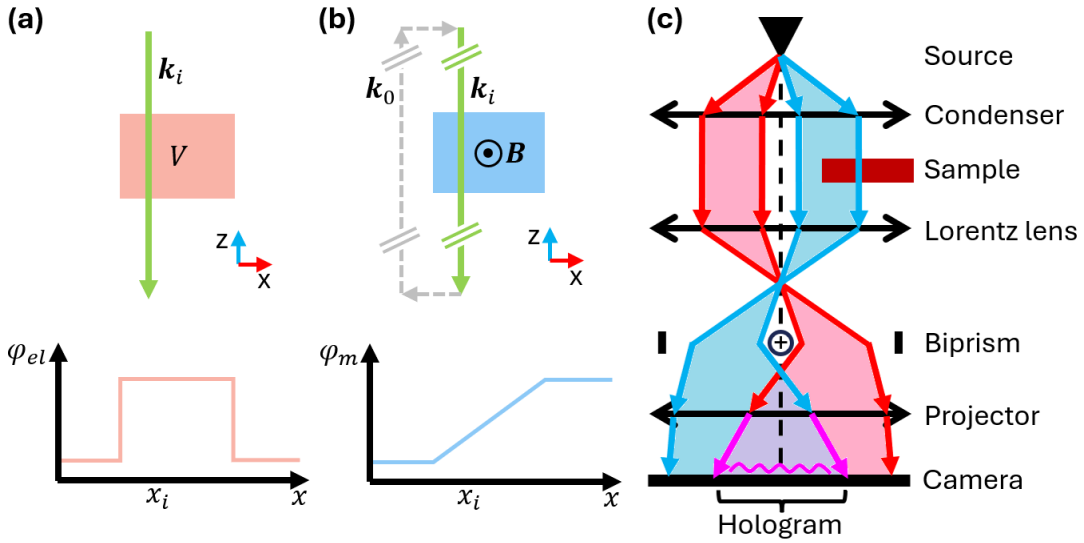

Figure 2.9. Hologram formation. (a) Schematic diagram showing the beam path and φ_{el} created by a potential V. (b) Schematic diagram showing the primary beam and beam in vacuum required to describe the φ_m created by a $\boldsymbol{B}$ field. The beams are shown as arrows parallel to wave vectors k_i, and the corresponding phase shifts are represented in the graphs below. (c) TEM ray diagram corresponding to off-axis electron holography. The object and reference beams are, respectively, shown in red and blue. Electromagnetic fields shift the phase of the object beam, and the phase shift can be reconstructed from holograms that are formed by overlapping two coherent beams.

2.6.2. Phase reconstruction

φ information is often lost when the directly transmitted beam is recorded by a camera in the image plane, as detectors are sensitive to the time-averaged intensity rather than Ψ itself. Reconstructing φ is possible if an interference pattern is formed, which can be achieved by overlapping two beams. Figure 2.9c is a ray diagram of off-axis electron holography, where an electrostatic biprism is used to deflect two electron beams and overlap them on the detector. The Möllenstedt biprism is a fine wire with radius

$r_1 \sim 1$ µm, positioned between electrodes at a distance r_2. When a positive potential (V_b) is applied to the biprism, it attracts electrons via the Lorentz force and deflects the beams by an angle

$$\delta = \frac{\pi \ q_e \ V_b}{2E \ \ln(r_1/r_2)}, \tag{2.10}$$

where E is the kinetic energy of the electrons [102]. Conventionally, V_b in the range from 20 V to 200 V is used to deflect the beams by ~ 10 µrad, which results in interference fringe spacing from 1 nm to 10 nm [37, 103]. It should be noted that TEMs used for holography often also include a Lorentz lens, which performs the function of the objective system without exposing the sample to magnetic fields, allowing the characterisation of magnetic materials. The measured interference pattern is described by the sum of two wave functions

$$\Psi_{hol}(x,y) = \Psi_{img} + \Psi_0 = a \ e^{i(\varphi + q_c x)} + a_0 \ e^{-iq_c}. \tag{2.11}$$

Where q_c is the wave vector representing the change in optical path length due to beam deflection along the x-axis, and a_0 is the amplitude of the reference wave Ψ_0 [37]. The normalisation $a_0 = 1$ is assumed if the Ψ_0 beam transmits only through vacuum, as shown in Figure 2.9c. The recorded interference pattern, named a hologram, corresponds to

$$I_{hol}(x,y) = \Psi_{hol}\Psi^*_{hol} = 1 + a^2 + a \ e^{i(\varphi + 2q_c x)} + a \ e^{-i(\varphi + 2q_c x)}. \tag{2.12}$$

Since φ directly modulates the measured signal, it can be reconstructed using numerical methods. Notably, the Fourier transform of the hologram can be expressed as three functions: the centre band; and two opposite side bands, that are located at points in reciprocal space corresponding to $q = 0$, $q = q_c$, and $q = -q_c$, such that

$$\mathcal{F}[I_{hol}](\boldsymbol{q}) = \mathcal{F}[a^2 + 1](\boldsymbol{q}) + \mathcal{F}[\Psi_{img}](\boldsymbol{q} - \boldsymbol{q_c}) + \mathcal{F}[\Psi^*_{img}](\boldsymbol{q} - \boldsymbol{q_c}). \tag{2.13}$$

Numerical representations of the sidebands are shown in the example Figure 2.10. Ψ_{img} can be reconstructed by performing a numerical fast Fourier transform (FFT) of the hologram, applying a numerical aperture at $\boldsymbol{q} = \boldsymbol{q_c}$ with radius $r = q_c/2$ to isolate and

re-centre one sideband, and applying an inverse FFT. The phase shift is then given by

$$\varphi(x, y) = \arctan\left(\frac{\mathrm{Im}(\Psi_{img})}{\mathrm{Re}(\Psi_{img})}\right). \tag{2.14}$$

In the experimental reconstruction of φ, all theoretical assumptions made during the derivation must be addressed. Figure 2.10 shows the reconstruction workflow for holograms of a Co NW, which includes the following experimental considerations [1].

- To reduce the significance of Poisson noise, multiple holograms are acquired and their reconstructed φ is averaged. The interference fringes can bend due to imperfect TEM alignment, hence reference holograms of empty space are acquired in vacuum to enable flat-field correction.

- The electron beam may not be parallel to the z-axis under strongly diffracting conditions, which may create unwanted diffraction contrast in some materials. In this work, no significant diffraction contrast is observed. Deflection of the electron beam by the biprism itself is limited to a few µrad, which is also often negligible.

- Coherent TEM lens aberrations, such as spherical aberration, introduce spatial averaging to Ψ_{img}, which limits the spatial resolution of φ reconstruction [47]. In the example Figure 2.10c, the actual resolution limit (6 nm) is determined by the range of spatial frequencies allowed by the numerical aperture. The aperture radius is limited to $r = q_c/2$ to prevent overlap between the side and central bands.

- Scattering and aberrations that cause incoherence primarily affect the a distribution, which is not relevant in this work.

- Reference-wave perturbation induced by the interaction between the reference wave and long-range electromagnetic fields from the sample is another source of uncertainty. To first order, it can be approximated by a linear phase ramp, since fields created by single charges or magnetic moments asymptotically approach zero at long distances [41].

Regarding software implementation, defining that φ_{el} is a positive number and electrons transmit in the -z direction are conventions that can be introduced without loss of generality, as in Figure 2.10f. Overall, the derivation of phase imaging and reconstruction is straightforward, and the uncertainties associated with off-axis electron holography are extensively studied, which makes it a suitable technique for the characterisation of electromagnetic fields.

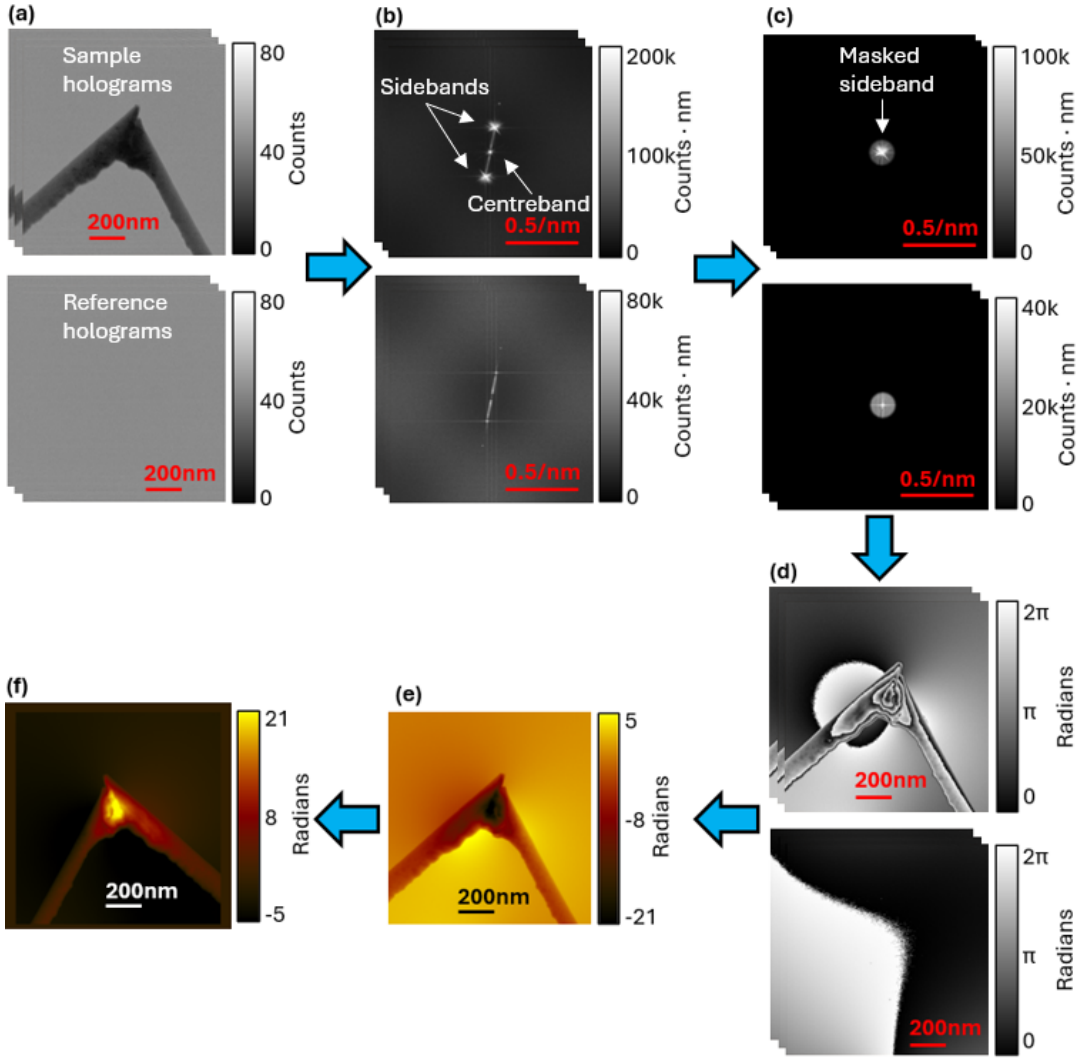

Figure 2.10. Hologram-to-phase reconstruction workflow. (a) Holograms of the sample (top) and reference holograms of free space (bottom). Five holograms are acquired with 2 s exposure time each. The interference fringe spacing is less than 3 nm, which is not visible in this document. (b) A FFT is applied to all holograms. The magnitude of the complex number array is shown. The peak signal at the sidebands is located at a 0.35 rad/nm distance from the centre. (c) The centre line is masked to reduce Fresnel fringes, and a virtual aperture is applied to isolate one sideband. (d) An inverse FFT is applied to the masked image, which results in a complex real-space image. The phase shift of the complex images is shown, and it corresponds to the phase difference between the object and reference waves. (e) The phase images are 'unwrapped' by applying a 2π offset at the discontinuous lines. Then they are averaged to reduce measurement noise, and the vacuum reference phase is subtracted. The total phase shift image is shown. (f) To ensure consistency, the image is rotated such that the electron beam direction is out of the page. The rotation is performed by assuming that the image defines a 2D plane in 3D space. Then the sign of the image is changed, such that the electrostatic mean inner potential is positive (following convention).

One of the more recent significant applications of electron holography is 3D magnetic imaging. By acquiring a tomographic tilt series of electron holograms, it is possible to reconstruct the magnetic induction ($\boldsymbol{B}$) [48], and the corresponding vector potential ($\boldsymbol{A}$), in 3D [104]. These reconstruction techniques are a form of EH-VFT, which is computed with high precision using MBIR algorithms [1, 105]. Statistically, MBIR is equivalent to a large least-squares fitting problem, where a tomographic series of φ measurements represents the input data, and the function is a forward model parametrised by a distribution of $\boldsymbol{M}$ vectors in 3D space that calculates corresponding φ_{sim}. Since ferromagnetic materials create $\boldsymbol{B}$ and $\boldsymbol{A}$, nanostructures can be comprehensively characterised by reconstructing the underlying 3D $\boldsymbol{M}$ distribution [1, 106, 107]. Therefore, the development of experimental and computational methods for 3D $\boldsymbol{M}$ reconstruction will be discussed in chapters 4 and 5, respectively.

From a theoretical perspective, the study of nanoscale electromagnetism is necessary to verify quantum field theories. Electromagnetism is one of the four fundamental forces of nature [108], and its description by a Lorentz-invariant 4-potential in the standard model of physics is one of the most exhaustively tested theories in history [109]. Based on these quantum-mechanical principles, a theory of electron interactions with materials has been derived from the Aharonov-Bohm effect [41]. Although the effect on φ has been tested unambiguously, the expected forces and interaction cross-sections have yet to be verified [110, 111]. Since EH-VFT can characterise electromagnetic fields and their underlying charge distributions [1, 112, 113], it is a distinct possibility that corrections to the mathematical formulism for quantum mechanical interactions in materials may be discovered as 3D reconstruction techniques are developed and approach atomic resolution.

2.7. Micromagnetic simulation

As mentioned in section 1.2, by considering the magnetostatic energy of a nanostructure, it is possible to simulate magnetic configurations. Since other energy forms and thermal fluctuations are omitted, the simulations approximate an idealised, defect-free material with temperature-independent properties [17]. Nonetheless, they are a useful qualitative technique for simulating what $\boldsymbol{M}$ distributions might exist. To compute a simulation, an equation and an algorithm for computing it must be chosen. The sum of Equations 1.1 for all magnetic moments in the material can be minimised to find an energetically

stable state. Additional energy terms can also be added to account for interactions with external fields or to model material-specific properties, including:

Zeeman energy $E_{app} = -\sum_i \mu_0 \boldsymbol{m_i} \cdot \boldsymbol{H_{app}}$, where $\boldsymbol{H_{app}}$ is an externally applied magnetic field. This term can be used to simulate hysteresis loops and magnetic domain reconfiguration in response to external fields.

Magnetocrystalline anisotropy energy $E_K = -\sum_i K \left(\frac{\boldsymbol{m_i}}{|\boldsymbol{m_i}|} \cdot \hat{\boldsymbol{u}} \right)$, where $K \geq 0$ is the anisotropy energy density, and $\hat{\boldsymbol{u}}$ is the unit vector parallel to the easy (energetically favoured) axis for $\boldsymbol{m_i}$. In some materials, the crystal structure can affect the alignment of $\boldsymbol{m_i}$, but magnetocrystalline anisotropy has a negligible net effect in nanocrystalline samples presented in this thesis.

DMI $E_{DMI} = \sum_{i,j} \boldsymbol{D_{ij}} \cdot (\boldsymbol{m_i} \times \boldsymbol{m_j})$, where $\boldsymbol{D_{ij}}$ is the atomic Dzyaloshinskii-Moriya interaction (DMI) constant. DMI is observed at interfaces between ferromagnetic films and adjacent layers with strong spin-orbit coupling, and is necessary to describe chiral magnetic configurations, such as skyrmions [21, 114]. DMI has not been observed in FEBID materials, but will be discussed when comparing non-trivial topological configurations in 2D and 3D nanostructures.

Conventionally, the four energy terms, namely, Heisenberg exchange, demagnetising field energy, Zeeman energy, and magnetocrystalline anisotropy are added to define the total micromagnetic energy, which is minimised to simulate energetically stable $\boldsymbol{M}$ configurations. However, it is straightforward to add additional energy terms, such as long-range coupling with conduction electrons [20], or effects of magnetostrictive strain [115].

Alternatively, the time evolution of an initial $\boldsymbol{M}$ state can be simulated by numerically integrating the Landau-Lifshitz-Gilbert equation [116]

$$\frac{\mathrm{d}\boldsymbol{M}}{\mathrm{d}t} = -|\gamma| \boldsymbol{M} \times \boldsymbol{H_{eff}} + \frac{\alpha}{|\boldsymbol{M}|} \left(\boldsymbol{M} \times \frac{\mathrm{d}\boldsymbol{M}}{\mathrm{d}t} \right). \tag{2.15}$$

Where the first term on the right-hand side describes the precession of $\boldsymbol{M}$ about $\boldsymbol{H_{eff}}$, and γ is typically the gyromagnetic ratio of a free electron spin. The second term is phenomenological and represents the damping of spin precession, specified by a positive parameter α, which is a property of the simulated material. $\boldsymbol{H_{eff}}$ is the sum of $\boldsymbol{H_{demag}}$, an effective field representing exchange energy, and any additional effective field terms. Equation 2.15 can also be further modified to model the effects of spin-polarised currents.

Given sufficient computation time, either equation can be used to find an energy minimum, but a direct solution by differentiating Equation 1.1 often requires fewer iterations [17].

The choice of algorithm depends on how the 3D $\boldsymbol{M}$ distribution that represents the sample is discretised. Finite difference schemes represent $\boldsymbol{M}$ as a grid with a vector in each rectangular volume element (voxel). Simulation software packages like OOMMF [117] and MuMax [118] use the rectangular geometry to implement software optimisations that reduce computation time by utilising graphics card optimisation and FFT. Alternatively, finite element schemes sample $\boldsymbol{M}$ at the vertices of a mesh composed of tetrahedra. The MERRILL simulation software [119] uses tetrahedral meshes to accurately represent samples with complex geometries. All simulation packages can find energy minima, but they are optimised for different types of simulations. Crucially, simulation results are only reproducible if the mesh spacing is relatively small. The exchange length $l_{ex} = \sqrt{\frac{2A}{\mu_0 M_s^2}}$, approximately 5 nm for common ferromagnetic materials, indicates the length scales over which $\boldsymbol{M}$ is expected to change direction. If the distance between neighbouring spin vectors is less than l_{ex}, the simulation is likely to be physically meaningful [17]. After a simulation is computed, its validity can be tested by measuring the maximum angle between neighbouring spins. Since the expression for exchange energy relies on the small-angle approximation, simulations are physically meaningful only if the maximum neighbour spin angle is less than 10° to 30° [22]. Overall, micromagnetic simulation is a technique for determining possible $\boldsymbol{M}$ distributions in samples, and how they might be affected by interactions with electrical currents or external magnetic fields.

2.8. Conclusions

The experimental procedures used for the fabrication and characterisation of the 3D nanostructures in this research have been presented. A SEM is used to map sample surface topography by recording SEs and fabricate ferromagnetic nanostructures with FEBID. Nanoscale resolution images of samples are acquired with a TEM, and the elemental composition of NWs is mapped with STEM EELS. With the addition of an electron biprism, a TEM can record interference patterns and reconstruct the phase shift of electron waves, which enables characterisation of electromagnetic fields. Micromagnetic simulations predict energetically stable configurations of $\boldsymbol{M}$ that can be compared with reconstructions of projected $\boldsymbol{B}$ obtained using off-axis electron holography, which are

indicative of underlying magnetostatic interactions. By combining these techniques, it is possible to fabricate and characterise increasingly complex ferromagnetic nanostructures.

Chapter 3.

Compositional Variation in Ferromagnetic Co and Fe Angled Nanowire Structures Fabricated Using Focused Electron Beam Induced Deposition

"The first principle is that you must not fool yourself - and you are the easiest person to fool."

— Richard P. Feynman, 1974

This chapter is based on a manuscript in preparation. Authors and CRediT:
Aurys Šilinga: software, methodology, formal analysis, writing—original draft & editing;
Keir Edgar: software, writing—review & editing;
András Kovács: supervision, writing—review & editing;
Rafal E. Dunin-Borkowski: writing—review & editing;
Kayla Fallon: writing—review & editing;
Stephen McVitie: writing—review & editing;
Trevor P. Almeida: supervision, writing—review & editing.

3.1. Introduction

Focused electron beam induced deposition (FEBID) is an additive manufacturing technique uniquely suited for fabricating nanoscale 3D prototypes for a range of applications, including spintronic devices. However, the variation of growth dynamics associated with electron beam translation and sample interaction volumes results in structures with non-uniform composition when fabricating intricate 3D geometries. Herein, we measure changes in atomic composition and corresponding changes of the magnetic induction in 3D ferromagnetic nanostructures with overhanging elements, e.g. bridges or arches. To investigate the effects of electron beam translation, we fabricated 41 Co and Fe NW structures with growth angle relative to the optic axis varying from 0°to 90°. The (scanning) TEM techniques of EELS and off-axis electron holography were performed to map the NW elemental composition and magnetic induction as a function of NW growth angle. Comparison of the results reveals that the metal content in FEBID NWs decreases from 0.1% to 0.4% per degree of growth angle, with the most consistent deposition occurring when the chemical reactions are concentrated in an interaction volume that does not exceed the NW diameter. Ferromagnetic NWs can be fabricated with consistent thickness and composition at growth angles up to 60°, by using a low electron beam voltage and a high beam current to reduce the interaction volume and increase the metal content, respectively.

3.1.1. Additive manufacturing of ferromagnetic nanostructures

The environmental impact of conventional electronics can be mitigated by the development of spintronic computing architectures, which are theoretically more energy-efficient when handling digital data [7]. Devices including magnetic RM for data storage [10] or magnetic synapses for artificial neural networks [11] function by moving and storing data as magnetic DWs in ferromagnetic NWs. These designs have been tested in 2D racetracks [10], but by expanding to 3D architectures the component density per chip area can be increased by angling NWs vertically with respect to the substrate [13]. Additionally, the shape anisotropy and symmetry breaking induced by NW curvature [14, 15] can be used to tune magnetic interactions that control magnetic DW movement. Complex 3D NW structures can be fabricated using focused electron beam induced deposition (FEBID), which is an additive manufacturing technique that can locally deposit ferromagnetic NWs with diameters down to 50 nm [65, 120]. Even though the range of fabrication geometries

is generally as unlimited as 3D-printing [79], many functional ferromagnetic structures comprise NWs that are deposited at a constant angle to the substrate [65, 67, 80]. Since the purity and magnetic properties of the FEBID material are generally dependent on the orientation of the electron beam [83], translation of the beam can cause non-uniform composition in the deposited nanostructures [79]. Ensuring that FEBID nanostructures have a uniform composition when fabricating complex geometries is crucial for the design of magnetic devices, which can be controlled by tuning the deposition parameters.

3.1.2. FEBID chemical reactions

FEBID is performed by injecting a precursor gas into the sample chamber of a SEM and irradiating solid material with the electron beam. This process drives the dissociation of precursor gas molecules through irradiation by SEs emitted from the substrate. The reaction products bond with surfaces in the vicinity of the reaction volume, typically forming a deposit of nanocrystalline metal. The primary challenge associated with FEBID is fabricating nanostructures with desired geometries while maintaining high metal purity, e.g., Co, Fe, etc. Inclusion of C & O contaminants and incomplete dissociation of the precursor gas is inherent to the FEBID process, which can result in relatively low metallic content [121] and loss of ferromagnetic properties. Optimising the deposition parameters and inclusion of post-processing stages have been thoroughly investigated to produce deposits with predictable ferromagnetic and charge transport behaviours, required for reliable device operation [42, 82, 122].

The composition of FEBID material is attributed to the balance between multiple chemical reactions occurring at the site where the SEM beam is incident on a substrate [121]. This includes adsorption, which involves the formation of a bond between the precursor gas and the substrate; dissociation of the precursor molecules via bond cleavage; and the desorption of reaction products from the surface. The underlying chemical reactions have been studied both in isolation and as a combined deposition reaction. For the commonly used $Co_2(CO)_8$ precursor gas, autocatalytic adsorption has been observed to occur spontaneously [123], but can also be driven by electron impact (EI) ionisation [121, 124]. Regarding dissociation, mass spectroscopy experiments have shown that EI breaks bonds between Co and organic ligands more frequently, resulting in the creation of ions of the form $Co_2(CO)_8 \rightarrow Co_{1-2}(CO)^{\pm}_{0-8}$ [124]. Calorimetry experiments have also shown that thermal dissociation (TD) at temperatures above 80 °C results in the deposition of pure Co and the desorption of CO gas, $Co_2(CO)_8 \xrightarrow{80^\circ} 2Co\downarrow + 8CO\uparrow$ [125].

Although the FEBID material can contain organic ligands and is not guaranteed to be ferromagnetic, the conventional beam-damage mechanisms of ionisation by scattered electrons and beam-induced heating act to increase the metal content, which can be tuned by controlling the SEM beam [82].

For comparison, the $Fe_2(CO)_9$ precursor gas also undergoes EI ionisation of the form $Fe_2(CO)_9 \rightarrow Fe_{1-2}(CO)_{0-9}^{\pm}$ [126], and TD $Fe_2(CO)_9 \xrightarrow{280^\circ} 2Fe\downarrow + 9CO\uparrow$ above 280°C [125]. Additionally, when $Fe_2(CO)_9$ is exposed to white light, heat, or electron beams [127, 128], it partially converts to $Fe(CO)_5$, which adsorbs autocatalytically [129]. In practice, the process for Fe and Co precursors is similar, but the higher TD temperature for $Fe_2(CO)_9$ requires the use of a higher intensity electron beam to promote TD when depositing Fe NWs.

Experimentally, when the SEM beam is stationary or rastering over a flat substrate, the elemental composition, magnetisation, electrical resistivity, and geometry of the deposited structure can be reproducibly controlled [120]. This is achieved by tuning several deposition parameters, including the accelerating voltage of the electron gun, the SEM beam current, the concentration of precursor gas, and the dwell time at each beam position. Using these methods, more than 90% Co purity has been achieved regularly [122, 130–132]. In comparison, when fabricating geometrically complex nanostructures, the position of the SEM beam can be controlled precisely, but the high intensity required to break metal-carbon bonds and deposit high-purity ferromagnetic metal must be maintained throughout. This is not straightforward when the beam transmits through a 3D sample and induces deposition on multiple layers, therefore, by controlling the deposition parameters, a trade-off must be made between SEM beam energy and current.

The purity of deposited NWs can be further improved by post-growth treatments, which include thermal annealing, electron beam curing [122, 133–135], reactive gas exposure, and combinations of each [136, 137]. Thermal annealing has been the most extensively investigated and successful post-processing treatment for increasing the relative metallic content in FEBID deposits. Temperatures in the 300-600 °C range are observed to induce thermal dissociation of carbonaceous material, which can diffuse and desorb from the deposit surface [83, 138]. This has been studied with Co [139, 140] and Fe [141, 142] precursors, generally resulting in enhanced purity and crystallinity of FEBID deposits. Overall, FEBID of vertical NWs and flat films has been extensively studied to optimise deposition parameters and purification methods.

3.1.3. FEBID 3D printing

The SEM beam can be programmed to slowly translate along a predefined path, which results in NWs growing at an angle (θ) relative to the SEM beam-axis, as illustrated in Figure 3.1a. $\theta = 0°$ corresponds to a NW that is deposited around a stationary SEM beam, and, in this work, is approximately perpendicular to the substrate surface (vertical). A translating beam can be used to fabricate intricate 3D NW structures, such as double-helices, helical latices, Moebius strips, or NW cubes that show curvilinear magnetic interactions [66, 79, 80], and may inform the design of spintronic devices. To fabricate such 3D nanostructures, predictive models are used to generate stream files that control the translation and dwell time of the incident electron beam. Models based on Langmuir-type approaches [143, 144] or atomistic Monte-Carlo [78, 145] have been developed to enable FEBID 3D printing from CAD designs and fabrication of micrometre-sized FEBID structures from Co or Fe. These model types assume that material is deposited in thin layers without affecting the layers underneath, which is inconsistent with the description of the TD reaction and does not predict either the anisotropic growth of angled NWs [79] nor auto-catalysed crystalline growth [129]. Such models are most accurate when TD is limited, and hence lower-purity material is deposited. Methods have been developed to simulate thermal conductance and FEBID TD reactions [79, 146], but they have been tested so far with Pt and Au.

In practice, the material properties of FEBID NWs are tuned depending on the intended application. Such optimisations leverage the observation that NWs exhibit characteristic responses to specific changes in the deposition parameters [82]. Since FEBID precursor gases are chemically similar and the underlying electron scattering interactions are the same [147], the effects of changing deposition parameters are similar for most materials. They can be observed by depositing NW 'A', changing one deposition parameter, and then depositing NW 'B'. The characteristic responses include:

R0. If nothing is changed, A and B are approximately identical. This indicates that the deposition is consistent, and is a necessary condition for the accuracy of FEBID CAD modelling [79, 143, 145].

R1. If the beam current is increased, B will have a larger volume and higher metal purity, as demonstrated for Co and Fe [42, 130, 132, 148]. There is an upper limit to the beam current beyond which randomly oriented crystalline growth is observed [128, 129, 149, 150].

R2. If the beam is defocused, B will have a larger diameter and lower metal purity. This has been observed for Co, Fe, and Pt [82, 147, 151–153]

R3. If B is annealed at a temperature in the 300-600 °C range, its metal purity will increase, as seen for both Co and Fe [139–142].

R4. If the beam accelerating voltage is increased, the geometry of B will be different. If the SEM beam is translating during deposition, the cross-section of B will be more elongated rather than circular. This has been observed for Fe, Co, $FeCo_3$, and Pt [67, 79, 81, 129, 153].

R5. If the speed of beam translation is increased, the metal purity of B will decrease. This is revealed for Co and Fe in this work.

In this work, Co NWs are fabricated with $\theta = 0°$ to test responses R0-R3 and verify that the FEBID system is functioning normally. Then Co and Fe NWs are fabricated with $0° \leq \theta < 90°$ at different accelerating voltages to quantify responses R4 & R5 and test whether R5 is material-agnostic. Furthermore, correlations among θ, metal purity, and magnetic induction in ferromagnetic NWs are measured; to develop methods for improving angled NW composition uniformity and inform the development of FEBID 3D-printing algorithms for ferromagnetic nanostructures.

3.2. Methods for consistent measurement of NW properties

3.2.1. Sample fabrication

A Thermo Fisher Scientific HELIOS Xe plasma focused ion beam (FIB) SEM was used to ion-mill flat substrates from a copper film, which could be electrically grounded during TEM and SEM imaging. NWs were deposited on the copper substrates using FEBID. The gas injection system (GIS) heated solid precursor material to induce sublimation and the precursor gas was injected through the GIS needle positioned at 45° to the substrate, at approximately 100 µm distance from the substrate surface. For FEBID, the $Co_2(CO)_8$ and $Fe_2(CO)_9$ precursors were heated to 29° C and 37° C, respectively. Nine sets of FEBID NWs were fabricated: first, five sets to characterise NWs deposited using a stationary SEM beam as reference samples; and secondly, another four sets

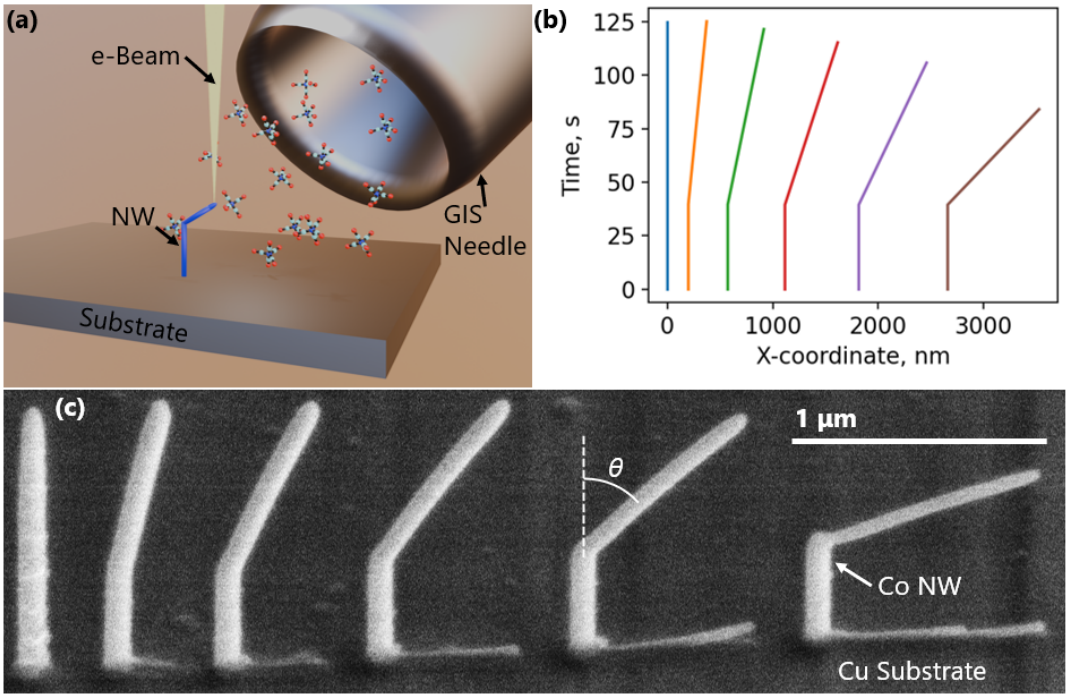

Figure 3.1. FEBID 3D printing process. (a) Schematic diagram of FEBID process, where NW structures are fabricated by injecting precursor gas through the GIS needle and translating the SEM beam along a path defined by stream files. The figure was rendered by Keir Edgar. (b) Streams that define SEM beam position as a function of time, during deposition. (c) SEM image of FEBID Co NWs fabricated by executing the streams in (b), viewed at a 55° sample tilt angle. To fabricate angled structures (c), the beam must be stationary at each position for an amount of time corresponding to (b).

to measure the composition change in NWs deposited with a translating SEM beam. Table 3.1 lists the details of each sample set, including the precursor gas, SEM beam accelerating voltage and beam current. For completeness, the base pressure in the SEM chamber was recorded before and during deposition, and to indicate the reaction rate, the vertical NW height to deposition time ratio is recorded. Compositional analyses and beam conditions for each individual NW are available in appendix B. The arrows in the dataset titles indicate whether the deposition was at $\theta = 0°$ (↑) or $\theta > 0°$ (↗). For each deposition, the SEM beam was focused to achieve minimum NW diameter. The samples were plasma-cleaned with an oxygen-argon mixture for 15 s to reduce amorphous carbon growth during STEM imaging.

The NW structures were fabricated using stream files that encode the SEM beam's X- and Y-deflections (in the substrate plane) as functions of deposition time. Vertical NWs were deposited using a stationary beam for 120 s, whilst angled NWs were deposited

by maintaining the beam stationary for 40 s and then translating it in the X-direction at a constant rate for up to 80 s. The electron beam dwell time at each coordinate is shown in Figure 3.1b. For the $\mathbf{Co}^{\nearrow}_{\mathbf{5\ kV}}$ dataset, each stream in Figure 3.1b translates the SEM beam at a different rate; therefore, the deposited NWs in Figure 3.1c grow at different angles relative to the vertical NW. Samples from all datasets are shown in Figure 3.2. Datasets $\mathbf{Co}^{\uparrow}_{\mathbf{30\ kV}}$, $\mathbf{Co}^{\uparrow}_{\mathbf{5\ kV}}$, $\mathbf{Co}^{\uparrow}_{\mathbf{anneal,\ 30\ kV}}$, $\mathbf{Fe}^{\uparrow}_{\mathbf{30\ kV}}$, and $\mathbf{Fe}^{\uparrow}_{\mathbf{5\ kV}}$ are used to find deposition parameters that enable controlled high-purity deposition of vertical NWs. Datasets $\mathbf{Co}^{\nearrow}_{\mathbf{5\ kV}}$, $\mathbf{Co}^{\nearrow}_{\mathbf{30\ kV}}$, $\mathbf{Fe}^{\nearrow}_{\mathbf{5\ kV}}$, and $\mathbf{Fe}^{\nearrow}_{\mathbf{30\ kV}}$ use the optimised parameters to deposit angled NWs. For calibration, NWs in the dataset $\mathbf{Co}^{\uparrow}_{\mathbf{anneal,\ 30\ kV}}$ were fabricated with lower currents and gas pressures and characterised before and after annealing at 350 °C for 30 min to verify consistency with previous works [42, 82, 140]. In summary, stream files are defined to fabricate angled FEBID NWs with growth angles ranging from 0° to 90°, and are executed using different precursor materials, accelerating voltages, and beam currents.

3.2.2. Elemental mapping

A JEOL ARM200cf operated at 200 kV (University of Glasgow) equipped with a cold field emission gun, a CEOS (Corrected Electron Optical System GmbH) probe corrector and Gatan 965 Quantum ER spectrometer was used to perform STEM EELS elemental mapping. A dual EELS system with a high-speed electrostatic deflector [154, 155] allowed simultaneous acquisition of high-loss and low-loss spectra from select areas of the FEBID NWs. The spectra were acquired using a 0.5 eV/pixel dispersion, 2.5 mm aperture, 29 mrad convergence semi-angle and 36 mrad collection semi-angle. Principal component analysis (PCA) [156] was utilised to remove X-ray signatures and reduce noise in high-loss spectra by reconstructing from the first 150 components, such that PCA would alter quantification results by less than 0.1% in sample areas with high signal-to-noise ratio (SNR), but provide smoothing in areas of low SNR. Spectra with more than 10^4 counts per energy channel in the fitting region were quantified using the Gatan Digital Micrograph elemental quantification plugin [95]. The measurement error stems from the combined contributions of Poisson noise and uncertainties of fitting the Hartree-Slater cross sections [92]. The uncertainty for relative atomic content measurement (atom %) in the thickest part of the NWs is less than 3% per scanned pixel.

Table 3.1. Deposition parameters for FEBID samples. Each sample comprises multiple NWs.

Dataset title	Beam voltage (kV)	Beam current (pA)	Depo. pressure (Pa)	Base pressure (Pa)	Growth rate (nm/s)	Precursor gas
$\mathbf{Co^{\uparrow}_{anneal,\ 30\ kV}}$	30	21 – 340	$0.9 \cdot 10^{-4}$	$0.5 \cdot 10^{-4}$	6 – 10	$Co_2(CO)_8$
$\mathbf{Co^{\uparrow}_{30\ kV}}$	30	170 – 2800	$2.2 \cdot 10^{-4}$	$0.7 \cdot 10^{-4}$	8 – 26	$Co_2(CO)_8$
$\mathbf{Co^{\uparrow}_{5\ kV}}$	5	170 – 2800	$2.2 \cdot 10^{-4}$	$0.7 \cdot 10^{-4}$	11 – 22	$Co_2(CO)_8$
$\mathbf{Fe^{\uparrow}_{30\ kV}}$	30	170 – 11000	$1.5 \cdot 10^{-4}$	$0.2 \cdot 10^{-4}$	6 – 20	$Fe_2(CO)_9$
$\mathbf{Fe^{\uparrow}_{5\ kV}}$	5	170 – 11000	$1.2 \cdot 10^{-4}$	$0.2 \cdot 10^{-4}$	6 – 20	$Fe_2(CO)_9$
$\mathbf{Co^{\nearrow}_{30\ kV}}$	30	690	$2.2 \cdot 10^{-4}$	$0.7 \cdot 10^{-4}$	8	$Co_2(CO)_8$
$\mathbf{Co^{\nearrow}_{5\ kV}}$	5	340	$2.2 \cdot 10^{-4}$	$0.7 \cdot 10^{-4}$	11	$Co_2(CO)_8$
$\mathbf{Fe^{\nearrow}_{30\ kV}}$	30	2800	$0.8 \cdot 10^{-4}$	$0.2 \cdot 10^{-4}$	5	$Fe_2(CO)_9$
$\mathbf{Fe^{\nearrow}_{5\ kV}}$	5	2800	$1.0 \cdot 10^{-4}$	$0.2 \cdot 10^{-4}$	7	$Fe_2(CO)_9$

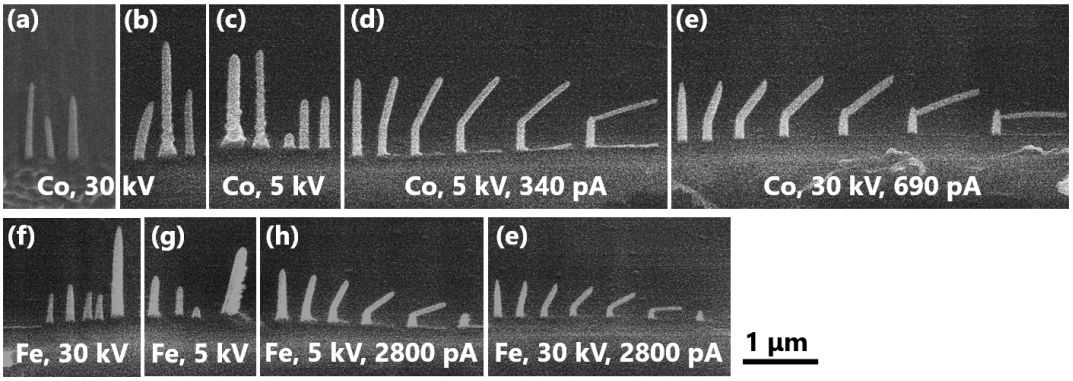

Figure 3.2. SEM images of FEBID NWs that are characterised and compared. (a-e) Respectively, samples $\mathbf{Co^{\uparrow}_{30\ kV}}$, $\mathbf{Co^{\uparrow}_{anneal,\ 30\ kV}}$, $\mathbf{Co^{\uparrow}_{5\ kV}}$, $\mathbf{Co^{\nearrow}_{5\ kV}}$, and $\mathbf{Co^{\nearrow}_{30\ kV}}$. (f-g) Respectively, samples $\mathbf{Fe^{\uparrow}_{30\ kV}}$, $\mathbf{Fe^{\uparrow}_{5\ kV}}$, $\mathbf{Fe^{\nearrow}_{30\ kV}}$, and $\mathbf{Fe^{\nearrow}_{5\ kV}}$. All images were acquired with the sample tilted 55° and are shown at the same scale. High-resolution images are available in appendix B.

A Cartesian coordinate system was defined to describe the cylindrical NWs, with the z-axis parallel to the TEM beam, the y-axis parallel to the NW length, and the x-axis parallel to the projected NW diameter. Figure 3.3 provides an example. The variation along the x-axis in the EELS map Figure 3.3a corresponds to the projected distribution of atomic composition of a NW in dataset $\mathbf{Co}^{\uparrow}_{\mathbf{5\ kV}}$, deposited with a 340 pA beam current. Figure 3.3b shows a modelled compositional map constructed from an NW with the cross-section displayed in Figure 3.3c. The FEBID NWs exhibit a radially layered structure, consistent with a Co (or Fe) rich core and an outer shell rich in C and O. Hence, care must be taken when interpreting EELS maps, as they represent the thickness projection of a radially varying structure, as previously observed [157]. This NW is modelled because it has a smooth surface texture. In this analysis, the Co purity is measured as the average concentration of Co atoms in the central band, corresponding to the volume indicated by dashed lines in Figure 3.3, defined as the 20 nm wide area around the projected centre of mass in the EELS compositional map. To enable comparison, measurements of magnetic induction will also consider only the average magnetic field within this volume.

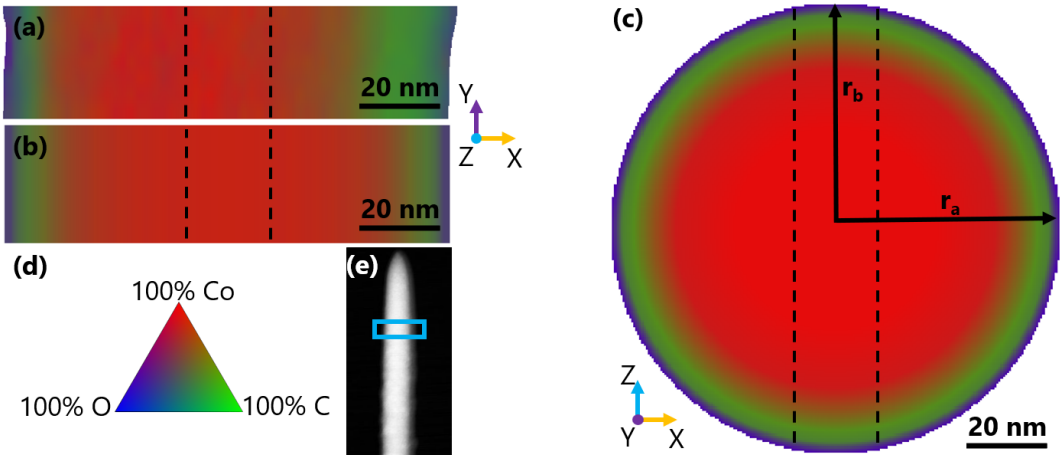

Figure 3.3. Atomic composition map and model. (a) STEM EELS compositional map for a vertical NW in dataset $\mathbf{Co}^{\uparrow}_{\mathbf{5\ kV}}$. (b) Projection of a compositional map, assuming the NW cross-section (c). (c) Model of an elliptical cross-section with a pure Co core, intermediate layers, and outer layers rich in C and O. (d) Colour map for (a), (b), and (c). (e) STEM ADF image identifying the location where (a) was acquired. FEBID NWs are modelled as multi-layered structures with elliptical cross-sections. Black arrows indicate the semi-axes of the ellipse, the insets show the coordinate system, and the dashed lines identify the volume where composition was measured.

A quantitative model that consistently describes the internal composition of all FEBID NWs is not presented in this study, but composition models for illustrative purposes are discussed. The 3D distribution of elemental composition is modelled by assuming that vertical NWs have circular cross-sections with radially varying composition. The radial distributions of Co, C, and O have been approximated by exponential functions with limited success [67], but models that correspond to experimental data more closely can be generated by modelling NWs as multi-layered cylinders. Since EELS maps are projections of the underlying 3D atomic distribution, they can be simulated based on a model of the NW and compared with experimental data, as shown in Figure 3.4. The projection described in Figures 3.4a-c assumes a 25 nm radius core with 100% Co content, linearly interpolated intermediate layers, and a 10 nm shell with an average composition corresponding to the red shaded area in the figures. This projection qualitatively resembles the experimental data shown in Figures 3.4d-f and 3.3, but it does not account for asymmetry.

The compositional model can be used to visualise how the non-magnetic NW shell affects EELS maps taken in projection. The shell composition (Figure 3.4g) can be estimated by assuming that material with $< 40\%$ Co content in Figure 3.4e is not ferromagnetic [140] and represents both the thickness and average composition of a hollow cylinder corresponding to the NW shell. The projected atomic density of the shell can be subtracted from the data (Figure 3.4d) to give partially corrected estimates of atomic composition, as shown in Figure 3.4f. The same algorithm can be applied to modelled data shown in Figures 3.4(a-c), and in both cases indicates that the presence of the shell offsets measurements of Co content by approximately 10%. Comparing simulated EELS maps to experimental data and considering the non-ferromagnetic material present on the surface of the NWs was necessary to generate the model shown in Figure 3.3. 2D elemental mapping was insufficient to automatically generate models, therefore, shell corrections are only illustrative and were not used in the quantitative analysis.

3.2.3. Measurement of NW elliptical cross-section shape

The 3D sample geometry must be known to perform quantitative measurements of magnetic induction. Therefore, NW cross-sectional shapes are described by ellipses as shown in Figure 3.3c, with the semi-major and semi-minor axes of the ellipse labelled r_a

& r_b, respectively. They define a cylinder in 3D space, with coordinates

$$z = r_b \cos(p);\ x = r_a \sin(p). \tag{3.1}$$

Where p is an arbitrary real-valued parameter and z & x are coordinates. When the sample is tilted by an angle γ during SEM imaging, it is equivalent to a rotation around the x-axis. Then, the observed NW width (W) is a tomographic projection [75] of the ellipse, given by

$$W(\gamma) = 2(r_a \cos(p_m)\sin(\gamma) + r_b \sin(p_m)\cos(\gamma)). \tag{3.2}$$

Where $p_m = \arctan\left(\frac{r_b \cos(\gamma)}{r_a \sin(\gamma)}\right)$ is the ellipse parameter corresponding to the point farthest from the origin in the projection plane. The axes can be measured by imaging the sample at $\gamma = 0°$ and $\gamma = 90°$, providing values of $W(0°) = 2r_b$ and $W(90°) = 2r_a$. When the model is accurate, W measurements at intermediate γ values are consistent with equation 3.2. In which case, the projected thickness of the NW during TEM imaging is given by

$$t_z(x) = 2r_a\sqrt{1 - \left(\frac{x}{r_b}\right)^2}. \tag{3.3}$$

This is needed to measure spatially resolved magnetic induction. Tomographic projections from both SEM and TEM were used to calculate t_z because this approach reduces uncertainty and ensures consistency between instruments.

3.2.4. Magnetic characterisation

Off-axis electron holography [37] is performed to reconstruct the magnetic phase shift (φ_m) of an electron wave passing through the sample and calculate magnetic induction ($\boldsymbol{B}$). Electron holograms were acquired using the FEI Titan G2 60–300 TEM at 300 kV (Ernst Ruska Centre for Microscopy and Spectroscopy with Electrons) and a 100 V voltage was applied to the electron biprisim, resulting in a hologram fringe spacing of approximately 3 nm. The total phase shift (φ) was reconstructed using Holoworks [158] and Holoview [159] extensions for the Digital Micrograph Software package [160]. Maps of φ are reconstructed with 5 nm spatial resolution, determined by the size of the virtual aperture selecting the hologram sideband, and have 0.01 rad measurement noise corresponding to the root-mean-square (RMS) difference between two vacuum reference images. Since the z-axis is defined as parallel to the TEM electron beam and the y-axis

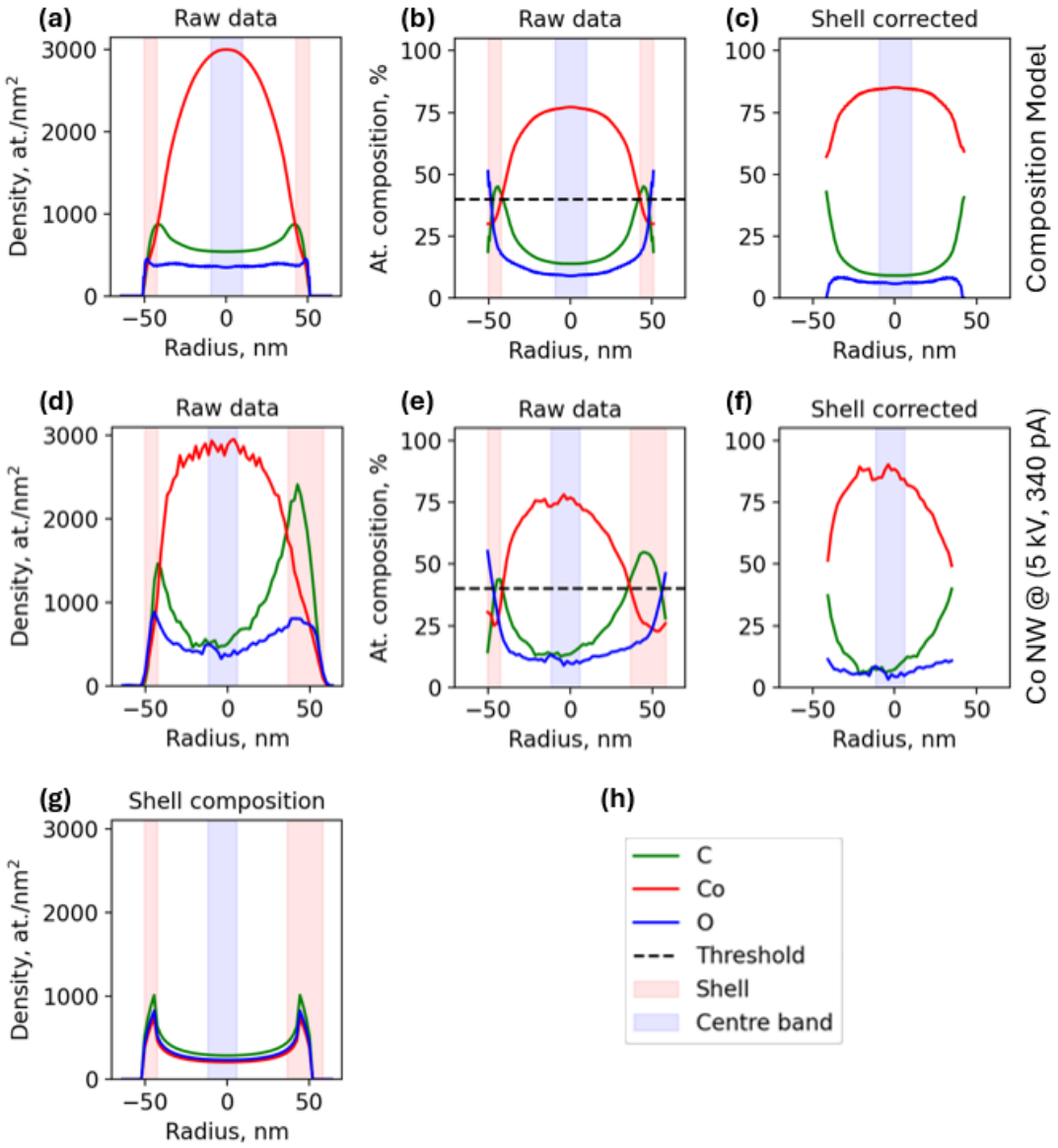

Figure 3.4. Comparison between model and measurement of atomic composition for the NW in Figure 3.3. (a)-(c) A radially symmetric model, qualitatively replicating experimental data in (d)-(f). (d),(e) y-averaged EELS maps of atomic density and composition, respectively. (g) Estimates of the composition of the outer shell of the NW, using experimental data. (c),(f) Composition estimates after subtracting the contribution of the shell, using modelled and experimental data, respectively. (h) Legend. The non-magnetic shell offsets EELS measurements taken in projection by $\sim 10\%$.

is parallel to the NW centreline, the Aharonov-Bohm effect [41] can be expressed as

$$\varphi = \varphi_{el}(V) + \varphi_m(A_z) = \frac{q_e}{\hbar v}\int V dz + \frac{q_e}{\hbar}\int A_z dz. \tag{3.4}$$

Where φ_{el} and φ_m are the electrostatic and magnetic contributions to the total phase shift (φ), respectively, q_e is the charge of an electron, $\hbar$ is the reduced Planck constant, v is the relativistic electron speed, V is the electrostatic potential, A_z is the z-component of the magnetic vector potential, and $\mathrm{d}z$ is a path element along the z-axis. The integral is over the full trajectory of the beam. To separate φ_m from φ_{el}, the NWs are magnetically saturated by tilting the sample to large opposite $\pm 70°$ α-tilt angles, applying a 1T magnetic field using the TEM objective lens, and acquiring φ images at 0° α-tilt angle for the opposite remnant states. Hence, the half-difference of the two φ images corresponds to φ_m. [138] Since $\boldsymbol{B} = \mathrm{curl}(\boldsymbol{A})$, the thickness-averaged magnetic induction component parallel to the y-axis is given by

$$B_y(x) = -\frac{\hbar}{q_e\ t_z}\ \frac{\mathrm{d}\varphi_m}{\mathrm{d}x}. \tag{3.5}$$

where t is the NW thickness in projection along the z-axis, given by equation 3.3. The measurement of B_y is used to compare the strength of magnetic induction fields created inside the NWs.

3.2.5. Micromagnetic simulations

Micromagnetic simulations are performed using Mumax3 [19, 23] to determine magnetisation configurations ($\boldsymbol{M}$) that are energetically stable in cylindrical FEBID NWs comprising nanocrystalline impure Co. To qualitatively evaluate possible $\boldsymbol{M}$ configurations, FEBID NWs can be approximated as uniform cylinders [31, 66]. The exchange stiffness is $A_{ex} = 1.5 \cdot 10^{-11}$ J/m and the saturation magnetisation is $M_s = 8 \cdot 10^5$ A/m, based on previous FEBID simulations [66, 161] and measurements of Co samples of different purities [1, 31, 140]. A cubic mesh with 2.5 nm voxel size is used for an exchange length $l_{ex} = \sqrt{\frac{2A_{ex}}{\mu_0 {M_s}^2}} \approx 6$ nm.

3.3. NW composition variations

3.3.1. Comparison of vertical NWs

To ensure consistency of analysis for all deposits, the vertical FEBID NW samples $\mathbf{Co^{\uparrow}_{30\ kV}}$(Figure 3.5a), $\mathbf{Co^{\uparrow}_{5\ kV}}$, $\mathbf{Fe^{\uparrow}_{30\ kV}}$, and $\mathbf{Fe^{\uparrow}_{5\ kV}}$provided a compositional reference.

Figure 3.5d displays an EELS elemental map acquired from the blue square in Figure 3.5a and reveals the metallic core and carbonaceous shell of the NW, as seen in previous works [42, 140]. In Figure 3.5e, the thickness-averaged cobalt content measured from the central 20 nm band (Figure 3.5d, rectangle) is compared to the other beam currents used for NWs in $\mathbf{Co}^{\uparrow}_{\mathbf{30\ kV}}$, $\mathbf{Co}^{\uparrow}_{\mathbf{anneal,\ 30\ kV}}$, and $\mathbf{Co}^{\nearrow}_{\mathbf{30\ kV}}$samples. The systematic EELS fitting uncertainty is $< 3\%$ for all points. In agreement with previous works, the highest purity NWs are deposited using higher beam currents and exhibit surface nodules attributed to autocatalytic deposition [123, 128, 140, 148]. Figure 3.5f demonstrates that annealing the $\mathbf{Co}^{\uparrow}_{\mathbf{anneal,\ 30\ kV}}$NWs at 350 °C for 30 min is an effective method of increasing mean purity, and correctly focusing the beam is important for depositing with high initial Co content [122, 133]. The compositional analysis agrees with previous observations that the deposition purity scales generally with SEM beam current [120], but high currents result in less consistent surface topologies.

3.3.2. Calibration of angled NW shape and composition measurements

To enable comparison, all NWs are characterised using the same methods. Since NW cross-sections can be elliptical, the NW diameter is measured twice by tilting the SEM stage and acquiring SEM images at $\gamma = 0°$ and $\gamma = 55°$ tilt, shown respectively in Figures 3.6a and 3.6b. The SEM images are acquired using an SE detector and have a 2.2 nm pixel size. The projected NW width is measured as the FWHM of the intensity line profiles in the SEM images, as shown by the lines corresponding to $W(55°)$ and $2r_b$.

STEM EELS elemental maps are acquired with 2 nm resolution to characterise areas of interest, as shown in Figure 3.6c. The sample orientation during (S)TEM imaging is equivalent to a $\gamma = 90°$ tilt, therefore the projected NW widths in the EELS maps can be used to determine r_a. Additionally, the radius of the calibration element (r) is the same in all projections, thus comparison of r measurements indicates that the intensity FWHM in SEM images corresponds to a width in EELS maps where more than 200 at/nm^2 are present in the beam path. Based on EELS thickness measurement, this shows that the SEM detects the NW edge at the position where the projected material thickness is $\sim$0.5 nm, which is significantly below the pixel size and does not require correction. Furthermore, the $W(55°)$ measurement is within two pixel-widths (6 nm) of equation 3.2, showing that the NW cross-sectional shape is consistent with an ellipse that has semi-axes r_a and r_b. Comparisons between NWs will be presented in a later section.

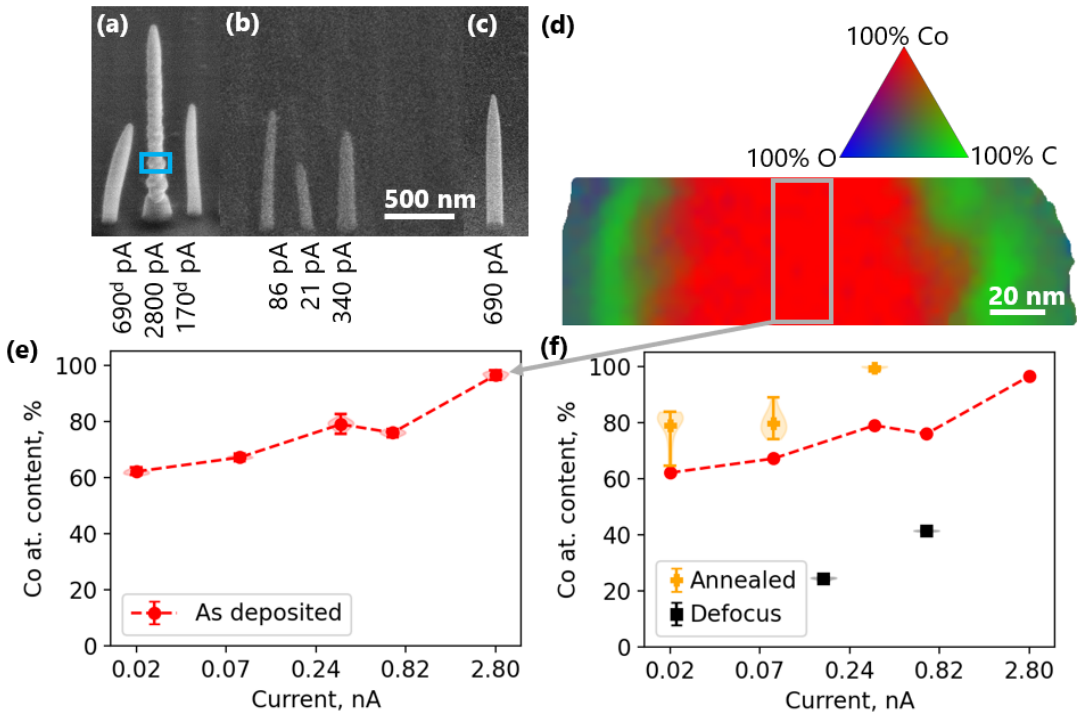

Figure 3.5. Comparison of vertical Co FEBID NWs deposited at 30 kV. (a-c) Vertical, 30 kV NWs from samples $\mathbf{Co}^{\uparrow}_{\mathbf{30\ kV}}$, $\mathbf{Co}^{\uparrow}_{\mathbf{anneal,\ 30\ kV}}$, and $\mathbf{Co}^{\nearrow}_{\mathbf{30\ kV}}$, respectively. The scale is identical in all three images, annotations show the beam current during deposition, and the ^{d} superscript identifies when the SEM beam was defocused. (d) EELS atomic composition map of the NW section corresponding to the blue box in (a). (e) Atomic cobalt content in the NWs before annealing. The error bars represent the range of Co content values measured in the central band. The systematic uncertainty is 3%. (f) Comparison between NWs that are annealed, not annealed, or deposited with a defocused beam. The violin plots represent the distributions of measured values in each central band. The abscissa is $\log_2$ scale.

The deposition consistency is evaluated by ensuring all nanostructures include a NW calibration element deposited with a stationary beam, such as the vertical sections in Figure 3.6b. EELS maps are used to compare Co content in the calibration element, as shown in Figure 3.6d. The violin plots indicate the distributions of Co content measurements in NW centre bands, corresponding to the rectangular boxes in Figure 3.6c. The $\theta = 0°$ NW is the outlier as the SEM beam is stationary, thus it transmits through the NW and irradiates the bottom layers for the entire deposition time. Consistent calibration sections indicate that deposition parameters do not vary significantly across nanostructures, enabling comparison of the angled NW sections. The growth angle θ is defined relative to the SEM optical axis, as shown in Figure 3.6c. Co content in the

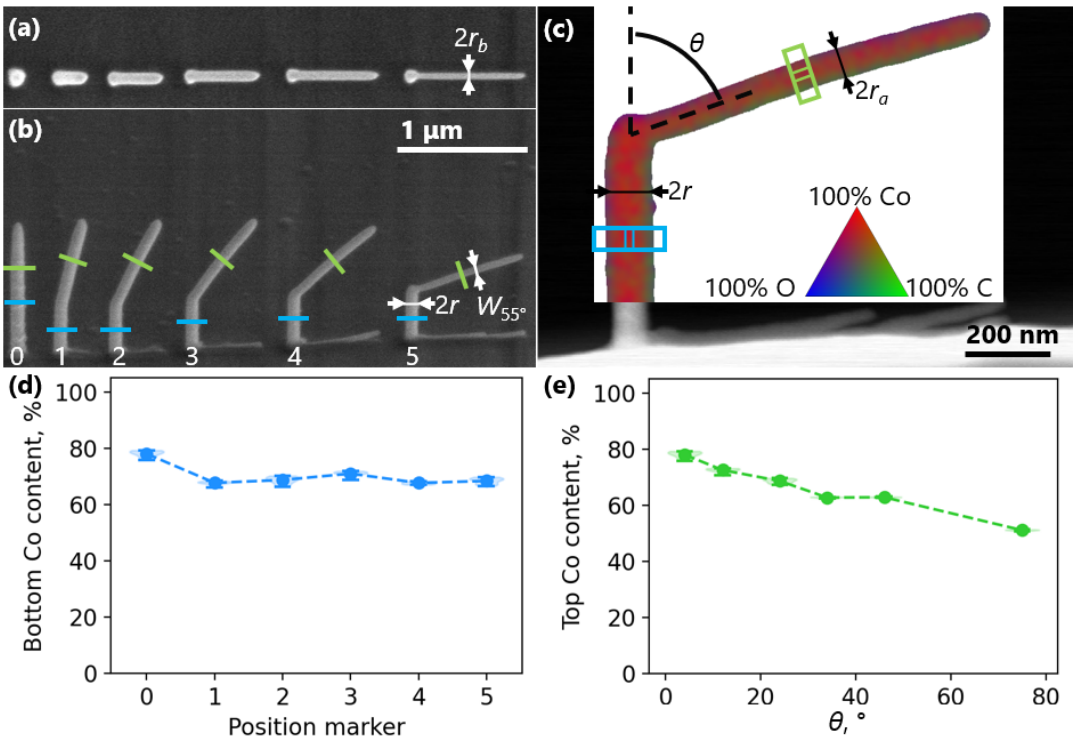

Figure 3.6. Measurement of cross-section shape and Co content for the $\mathbf{Co^{\nearrow}_{5\ kV}}$ sample. (a) 0° tilt SEM image of NWs. (b) 55° tilt SEM image of NWs. The lines indicate the locations of high-resolution STEM EELS scans. (c) STEM EELS map displayed over a STEM ADF map of the 5th NW. The boxes indicate the locations of high-resolution STEM EELS scans, θ is the NW growth angle, and black lines correspond to width measurements relating to equation 3.2. (d) Atomic Co content in NW regions corresponding to the horizontal blue lines in (b), used to verify consistency. (e) Co content in NW regions corresponding to the angled green lines in (b). The NW composition and cross-section shape are characterised to determine the correlation with θ.

angled NWs is compared in Figure 3.6e, showing a negative correlation between Co content and θ.

3.3.3. Compositional analysis of angled NWs

Having established fabrication and characterisation methods consistent with the expected results for vertical NWs, angled NWs are characterised. Figure 3.7 presents the variation of NW composition and shape as a function of θ, for samples $\mathbf{Co^{\nearrow}_{5\ kV}}$, $\mathbf{Co^{\nearrow}_{30\ kV}}$, $\mathbf{Fe^{\nearrow}_{5\ kV}}$, and $\mathbf{Fe^{\nearrow}_{30\ kV}}$(Figure 3.7a), which were fabricated by translating the SEM beam during deposition. Figure 3.7b shows that the mean metal content (Co or Fe) in the 20 nm

central band declines with increasing θ for all NWs. The lowest observed purity loss is 0.1% per degree of growth angle for the $\mathbf{Fe}^{\nearrow}_{\mathbf{5\ kV}}$samples, and the highest is 0.4%/° for the $\mathbf{Co}^{\nearrow}_{\mathbf{30\ kV}}$. The length of r_a is shown in Figure 3.7c, revealing that the NW cross-sectional area shrinks during beam translation. Figure 3.7d displays the r_a/r_b ratio as a function of θ, indicating that the NW cross-section becomes more elliptical if a 30 kV accelerating voltage is used and the beam is translated, confirming previous works [81]. The results show that $\mathbf{Fe}^{\nearrow}_{\mathbf{5\ kV}}$achieves the highest metal content and the most uniform distribution, whilst maintaining a uniform cross-sectional shape.

3.3.4. Micromagnetic simulations of cylindrical FEBID NWs

To investigate magnetic configurations in FEBID NWs, 1 µm long cylinders of FEBID Co are simulated. The diameters are varied in the range from 60 nm to 240 nm, and the initial magnetic states are aligned parallel to the y-axis (red arrow in Figure 3.8), such that the simulation emulates a relaxation after being subject to a saturating external field [19]. Corresponding energetically stable configurations are shown in Figure 3.8. Whilst magnetic flux closure is always visible at the cylinder ends, the majority of the volume is magnetised parallel to the long axis if the cylinder diameter is below 160 nm. For diameters above 160 nm, various vortex configurations are observed because they reduce the magnetostatic energy term. Based on these simulations, the angled NWs in Figure 3.7 are expected to be uniformly magnetised. Hence, the magnitude of $\boldsymbol{B}$ is comparable to B_y and can be calculated from reconstructed φ_m.

3.3.5. Magnetic induction in angled NWs

Figures 3.9 and 3.10 present the relationship between NW growth angle θ, and by implication purity, and the magnetic properties of samples $\mathbf{Co}^{\nearrow}_{\mathbf{5\ kV}}$and $\mathbf{Fe}^{\nearrow}_{\mathbf{30\ kV}}$, respectively. These samples comprise NWs of 0.5 µm to 1.5 µm in length, thus exhibiting magnetic configurations in a range of geometries. Figure 3.9a shows magnetic induction maps reconstructed from electron holography of the $\mathbf{Co}^{\nearrow}_{\mathbf{5\ kV}}$NWs deposited using a 340pA beam current. To create magnetic induction maps, the φ_m images underwent Gaussian smoothing and the cosine was amplified ($\times 5$) to produce magnetic phase contours, and colour wheels are used to show the projected $\boldsymbol{B}$ direction. Figure 3.9b shows line traces of φ_m as a function of θ, from which, after adjusting for variations in NW cross-sectional area, the mean B_y value in the 20 nm centre bands was calculated (Figure 3.9c). The error in $\overline{B_y}$

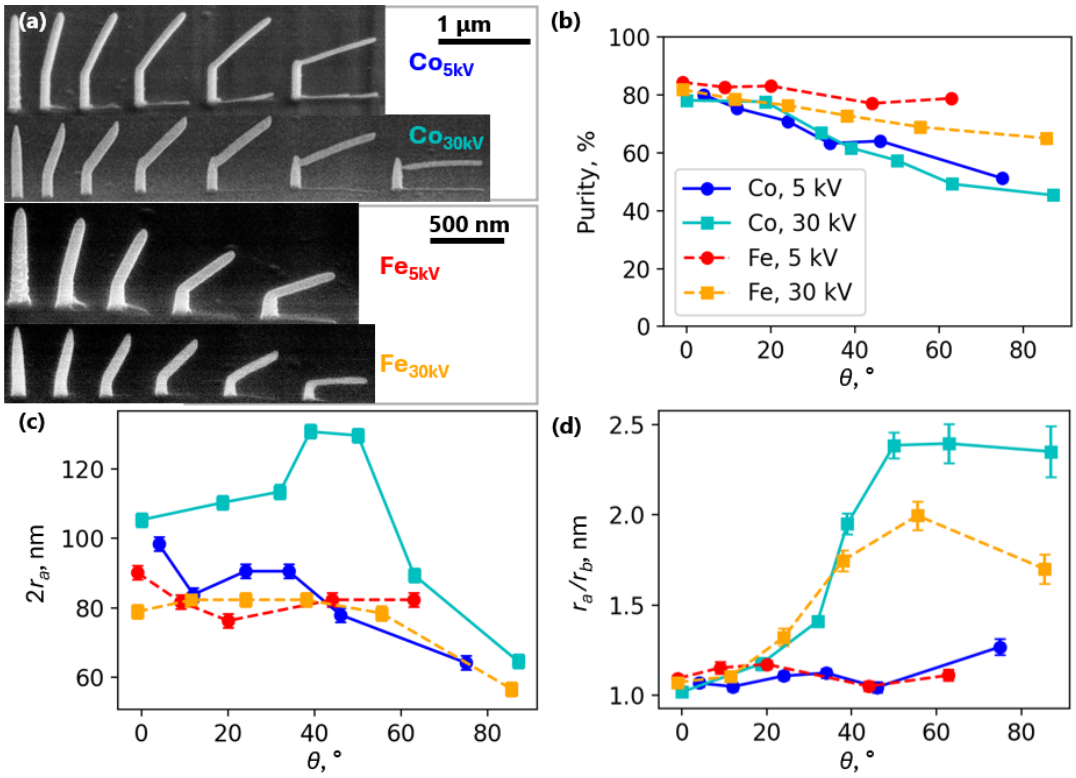

Figure 3.7. Variation in NW composition and shape as a function of growth angle. (a) SEM images of the $\mathbf{Co}_{\mathbf{5\ kV}}^{\nearrow}$, $\mathbf{Co}_{\mathbf{30\ kV}}^{\nearrow}$, $\mathbf{Fe}_{\mathbf{5\ kV}}^{\nearrow}$, and $\mathbf{Fe}_{\mathbf{5\ kV}}^{\nearrow}$NWs. (b) Mean atomic content of metal (Co or Fe) in the NW central bands as a function of θ. Error bars in (b) are not drawn to improve graph readability, but would represent 3% systematic uncertainty and less than 2% random error for each point. (c) The length of the major axis of the elliptical NW cross-section, as a function of θ. Error bars correspond to STEM image pixel size. (d) Ratio of the major and minor axes of the cross-section, as a function of θ. Error bars correspond to one standard deviation of random error. For all tested precursor gases, accelerating voltages, and beam currents, the NW purity and cross-sectional area decrease with increasing beam translation speed.

represents the combined uncertainty of projected NW thickness measurements and the standard deviation of B_y in the central bands. Since the NWs are uniformly magnetised and have a length-to-projected-diameter ratio greater than 5:1, $\overline{B_y}$ is indicative of the saturation induction B_0, which is an intrinsic material property. Based on modelling of the demagnetising fields, the average B_0 is expected to be up to 20% greater than $\overline{B_y}$ for such NW geometries [162]. It should be noted that the lowest-purity NW deposited at $\theta > 70°$ was observed to warp during STEM EELS mapping, creating a site for a magnetic DW to nucleate. Hence, the φ_m line trace was acquired off-centre, so it is in the middle of a uniformly magnetised region.

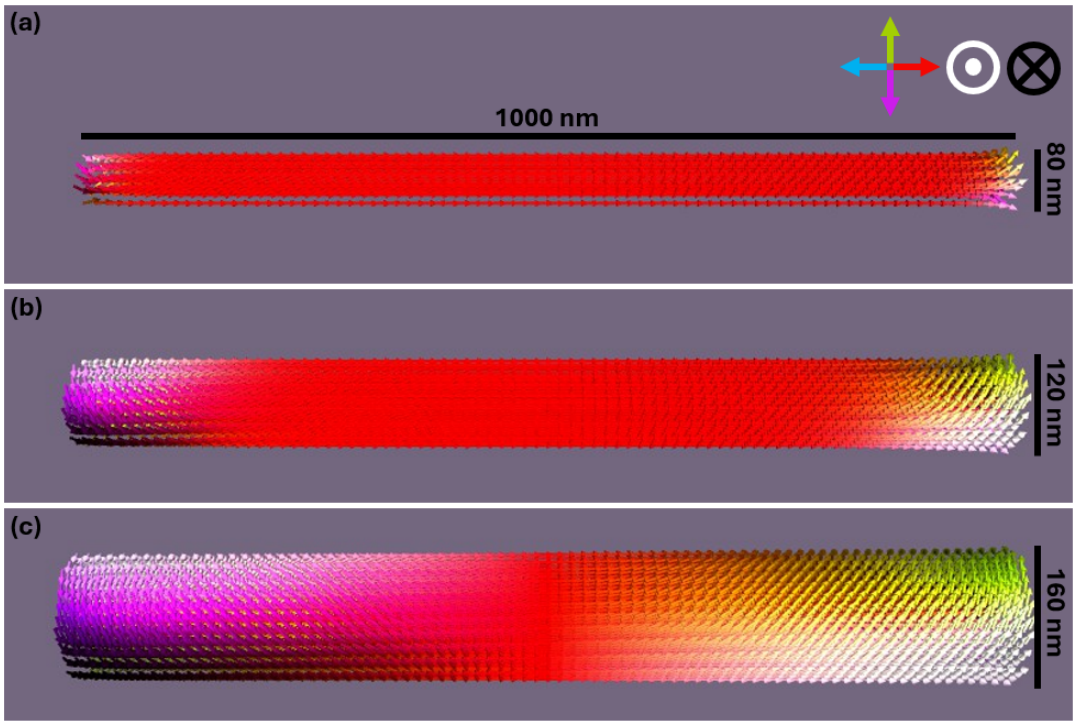

Figure 3.8. Micromagnetic simulations of FEBID Co cylinders. (a), (b), (c) correspond, respectively, to 80 nm, 120 nm, and 160 nm diameter cylinders. In the energetically stable configuration, cylinders with diameters below 150 nm are predominantly magnetised parallel to the long axis. The simulations were performed by Keir Edgar.

For comparison, Figure 3.10 shows magnetic induction maps of the $\mathbf{Fe}^{\nearrow}_{\mathbf{30\ kV}}$NWs deposited using a beam current of 2800pA (Figure 3.10a), line traces of φ_m as a function of θ (Figure 3.10b) and the calculated mean B_y value in the centre bands (Figure 3.10c). In both $\mathbf{Co}^{\nearrow}_{\mathbf{5\ kV}}$and $\mathbf{Fe}^{\nearrow}_{\mathbf{30\ kV}}$samples, the NWs grown at larger angles are observed to create weaker magnetic fields, and the average B_y value reduction is 2 mT and 7 mT per degree of θ, respectively. As noted above, the outliers to this trend occur at $\theta \approx 0°$ in both datasets due to the stationary SEM beam transmitting through the length of the NW for the entire duration of deposition, thereby altering the geometry and composition of the lower layers.

Figure 3.11 summarises the correlation between NW metal content and $\overline{B_y}$ measurement. The data in Figures 3.9c and 3.10 are plotted with respect to the metal content in each angled NW and are compared with the literature. The two blue datapoints in the top right of Figure 3.11a correspond to the thermally annealed NWs and agree with previous works [42, 140] characterising annealed Co FEBID NWs (Figure 3.11a, black

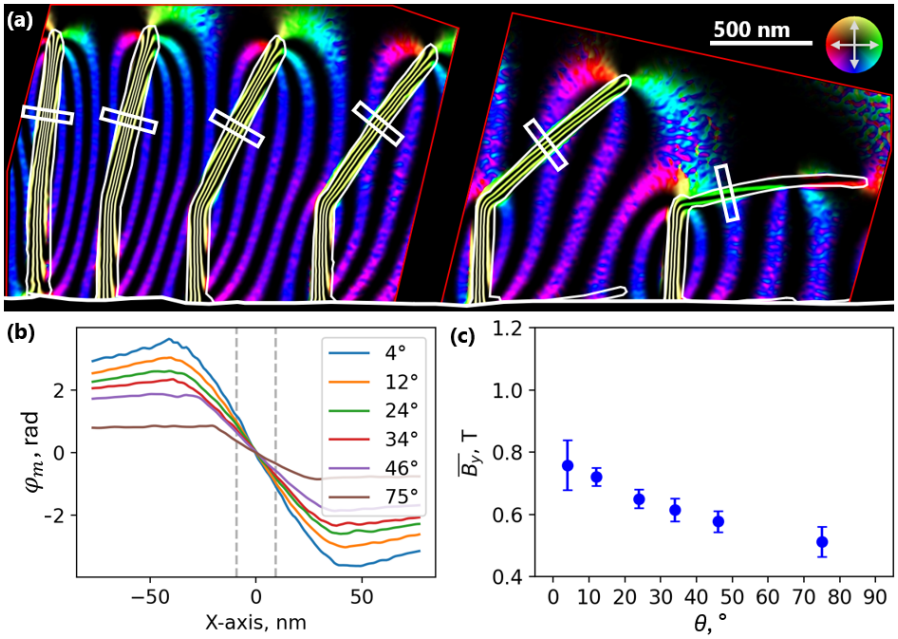

Figure 3.9. Magnetic characterisation of the $Co^{\nearrow}_{5\ kV}$ sample. (a) Magnetic induction map with contour spacings of 1.3 rad. The underlying hologram was acquired by Trevor Almeida. (b) Line traces of φ_m are from areas corresponding to the white boxes in (a). The measured φ_m is consistently smaller for higher θ. The central band is denoted by dashed lines. (c) Correlation between θ and B_y in the central band.

dots and dashed lines). The underlying magnetic induction maps for annealed NWs are shown in Figure 3.12. All other blue datapoints correspond to $\mathbf{Co}^{\nearrow}_{\mathbf{5\ kV}}$NWs, which are not annealed, and lie outside the range of the referenced study. For FEBID NWs, $\overline{B_y}$ is smaller than 1.75 T B_0 for bulk single-crystal Co [131, 163]. For the $\mathbf{Fe}^{\nearrow}_{\mathbf{30\ kV}}$NWs, the values of $\overline{B_y}$ in Figure 3.11c are lower than the 2.1 T value measured for pure bulk iron [164]. $\overline{B_y}$ is lower than B_0 due to contributions from the demagnetising field and represents the average thickness in NWs with radially varying composition, but it is indicative of the variation in effective $\boldsymbol{B}$. Overall, the $\boldsymbol{B}$ field created in ferromagnetic NWs is affected by growth angle due to changes in elemental composition.

3.4. Optimisation for uniform magnetic properties in 3D nanostructures

This study has analysed multiple datasets to identify the optimal SEM conditions for FEBID of angled NW structures and highlighted considerations for designing nanostructures in CAD. Characteristic FEBID NW variations in response to changes in deposition parameters were observed, including increases in metal content with increased SEM beam current, precise focussing of the electron beam, or thermal annealing of the NWs at 350 °C for 30 min [82, 140, 147, 152]. These were all considered to find optimal beam currents for fabricating angled ($0° \leq \theta \leq 90°$) Co and Fe NWs at 5 kV and 30 kV accelerating voltages. In all samples, increasing the SEM beam translation speed characteristically increases θ, but reduces NW cross-section area, metal content, and the magnitude of $\boldsymbol{B}$. The most symmetrical and highest purity angled NWs were deposited using the combination of the lowest tested accelerating voltage (5 kV), the highest beam current (2.8 nA), and the $Fe_2(CO)_9$ precursor.

The SEM beam current is increased by increasing the spot-size [72], which enables more electrons to pass through the condenser aperture at the expense of beam broadening. The corresponding elevation in precursor ionisation and beam-induced heating promotes high-purity deposition, but the NW diameter is increased. The highest beam current of 2.8 nA used in this study resulted in a NW diameter lower than 150 nm. Micromagnetic simulations demonstrated that, in 1 µm long Co cylinders with diameters $\leq$ 150 nm, ($\boldsymbol{M}$) is mostly uniaxially oriented. Hence, small-diameter NWs are investigated due to the enhanced magnetic signal associated with uniaxial magnetic configurations, which is advantageous for spintronic device applications [10]. Additionally, excessively high beam

currents can lead to unpredictable autocatalytic growth (Figure 3.5a). Similarly for the $Fe_2(CO)_9$ precursor, which dissociates to $Fe(CO)_5$ [128] during irradiation, FEBID can produce randomly oriented crystalline iron composed of single-crystal grains up to 1 µm in length [129]. Consequently, the maximum viable beam current is limited by the NW diameter and required growth predictability.

The optimal SEM beam acceleration voltage is often sample-specific because electron energy affects the optical power of SEM lenses, and alters the scattering interaction cross-sections in the NW and the substrate [72, 157]. In this study, a minimum accelerating voltage of 5 kV was used, as lower voltages compromised imaging resolution and reduced the ability to achieve good focus. At 5 kV, the cross-sections of angled NWs are circular (Figure 3.7d) since the interaction volume is comparable to the NW diameter and SEs are generated in a localised spot [74]. At 30 kV, highly elliptical cross-sections are observed due to SEs being generated along a line as the beam transmits through the NW. Additionally, the vertical growth rate in angled NWs is larger at 5 kV compared to 30 kV (Figure 3.7a), whereas Table 3.1 shows an inverse relationship of vertical NWs growing faster at 30 kV than at 5 kV when using high beam currents. This is attributed to the smaller interaction cross-sections of 30 kV electrons [165], resulting in electrons imparting less energy during transmission through the sample surface. Despite sample specificity, the 0.1 – 5 kV range is considered advantageous for FEBID of angled NWs due to the smaller interaction volume, where the incident beam provides an approximately point-like source of SEs [82, 157] and leads to more consistent deposition.

The precursor gas pressure was held constant, with fluctuations not exceeding $2 \cdot 10^{-5}$ Pa, which is believed to have negligible effects on composition or growth rate [130]. The spatial distribution of precursor gas concentration is dependend on GIS alignment [166] and has been observed to affect NW deposition reaction rate, geometry, and atomic composition [130]. Although local gas concentrations were not measured, they are assumed to be constant because GIS alignment and chamber pressure were consistent for all samples.

Of the tested precursors, the $Fe_2(CO)_9$ molecule is more stable than $Co_2(CO)_8$, as indicated by the higher required beam currents (Table 3.1) and threshold temperature for TD [125]. In Figure 3.7b, the elemental composition of Fe NWs, in comparison to CO, is less affected by variations in the SEM beam translation speed. This is attributed to improved confinement of deposition reactions, as molecules outside the immediate vicinity of the SEM beam are less impacted by scattered electrons or conducted heat. It

should be noted that other FEBID precursor gases are available [120], and $HCo_3Fe(CO)_{12}$ has been used to successfully deposit ferromagnetic angled NW structures [67].

NW arrays [66], artificial spin ices [67], and 3D data storage [13] prototypes can be fabricated with FEBID. Achieving uniform composition throughout these structures is essential to ensure reproducible and reliable device performance. We have demonstrated that a uniform material composition and high metal purity can be achieved when the deposition parameters are optimised to confine the reaction volume to dimensions no larger than the NW diameter, whilst using a high beam current. However, NWs grown at angles $\theta > 60°$ from the optic axis exhibit a twofold decrease in magnetic signal due to reduced NW cross-sectional area. It may be possible to correct this in associated CAD modelling software [79] by increasing the diameter, as the NW composition is largely independent of growth angle using the optimised deposition parameters. The observed decrease in metal purity was, on average, 0.1% per degree of θ. Better material uniformity may be achieved by investigating how precursor gas concentration affects angled NWs, or by using accelerating voltages below 5 kV, which would require the introduction of additional sample features to enable fine focus. Additionally, the metal purity and resultant magnetic induction (Figure 3.11) may be increased by thermal annealing observed in vertical NWs (Figure 3.5), but the optimal temperature for preserving nanostructure uniformity would need to be determined. Overall, using high electron beam currents and optimising deposition parameters to limit the reaction volume has significantly improved the uniformity of angled ferromagnetic FEBID NWs, which is beneficial for the fabrication of uniform 3D nanostructures.

3.5. Conclusions

Strategies are discussed for optimising deposition conditions to improve material uniformity in 3D ferromagnetic FEBID nanostructures. This work demonstrates inherent variation in the material properties of angled FEBID NWs deposited with a translating electron beam, as compared to a stationary beam, and shows that these properties can be tuned by adjusting the deposition parameters. Higher-energy electron beams penetrate further into a material, which can delocalise the deposition reactions by irradiating a larger volume. FEBID of angled Co NWs using a 30 kV beam reveals a reduction in cross-section area and a decrease in metal content by up to 0.4% per degree of growth angle relative to the optic axis. TEM characterisation confirms that the reduction of NW

purity results in a corresponding weakening of the magnetic induction. Ensuring uniform NW composition enhances the consistency of spintronic circuit prototypes fabricated with FEBID. Consequently, angled NWs fabricated using different combinations of SEM beam current, accelerating voltage, and precursor gas type were characterised to assess compositional variations. By using the optimum conditions of: 5 kV accelerating voltage; 2.8 nA beam current; and the Fe_2CO_9 precursor gas, the decrease in NW metal content was found to be limited to $0.1\%/^{\circ}$, and the NW cross-sectional shape is preserved for growth angles up to 60°. In summary, the angled NWs (0° to 60°) can be fabricated compositionally uniform and ferromagnetic by tuning the FEBID parameters to confine the deposition reactions to an interaction volume within the NW diameter.

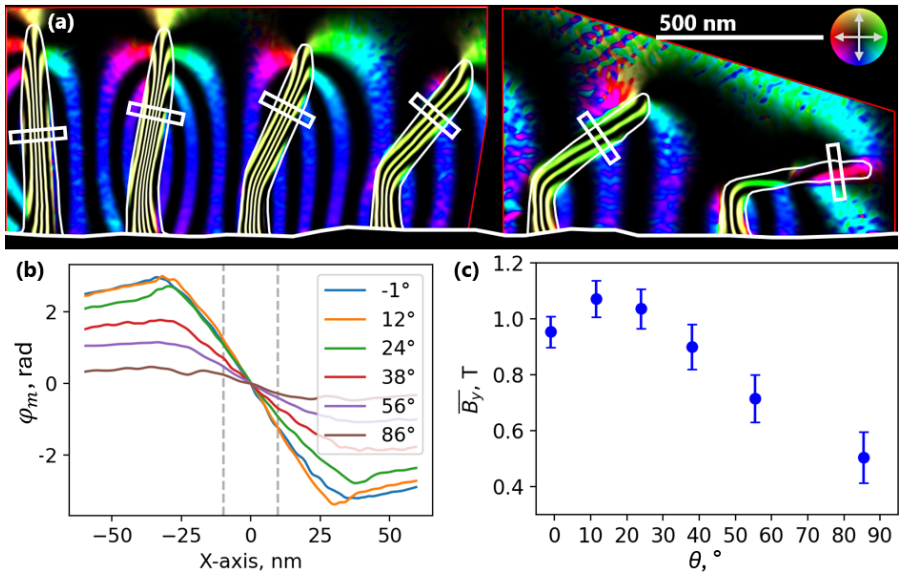

Figure 3.10. Magnetic characterisation of the $\text{Fe}_{30\text{ kV}}^{\nearrow}$ sample. (a) Magnetic induction map with contour spacings of 1.3 rad. The underlying hologram was acquired by Trevor Almeida. (b) Line traces of φ_m are from areas corresponding to the white boxes in (a). The measured φ_m is consistently smaller for higher θ. The central band is denoted by dashed lines. (c) Correlation between θ and B_y in the central band.

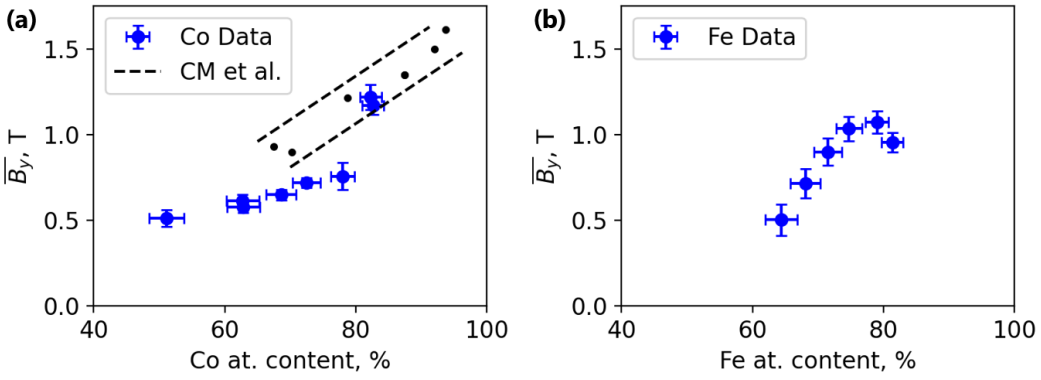

Figure 3.11. Correlations between NW metal composition and associated magnetic properties. (a) Correlation between mean B_y and atomic Co content for FEBID NWs. Black dots and dashed lines indicate the data and range of uncertainties in previous works [42, 140], respectively. (b) Correlation between mean B_y and Fe content for angled FEBID NWs. There is a correlation between metal content and the strength of magnetic fields created by the NWs.

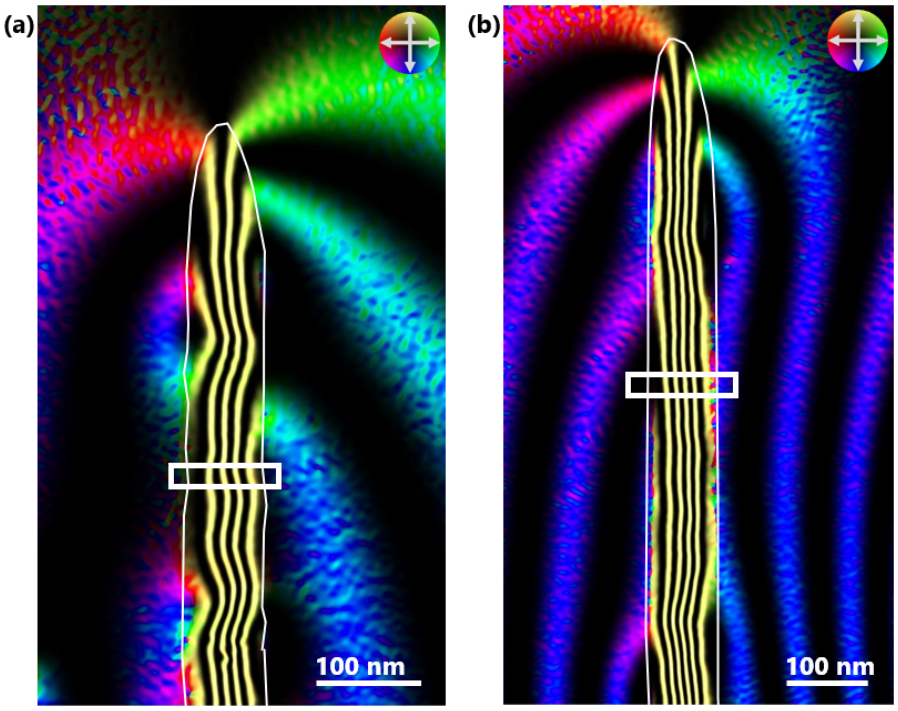

Figure 3.12. Magnetic induction maps of Co NWs annealed at 350 °C for 30 min. (a) and (b) were deposited using 21 pA and 86 pA beam currents, respectively. Contour spacing is 1.3 rad and the inset indicated the direction of projected $\boldsymbol{B}$. Line traces of magnetic phase shift are acquired from the areas corresponding to the white boxes and indicate B_y consistent with previous works [42].

Chapter 4.

Model-Based Iterative Reconstruction of Three-Dimensional Magnetisation in a Nanowire Structure Using Electron Holographic Vector Field Tomography

"I would like to use it as the cover art for the current issue of the journal."

— An editor of Microscopy and Microanalysis, 2025

This chapter was published in Microscopy and Microanalysis [1]. Authors and CRediT:
Aurys Šilinga: software, formal analysis, writing—original draft & editing;
András Kovács: supervision, methodology, writing—review & editing;
Rafal E. Dunin-Borkowski: writing—review & editing;
Kayla Fallon: writing—review & editing;
Stephen McVitie: writing—review & editing;
Trevor P. Almeida: supervision, methodology, writing—review & editing.

4.1. Introduction

Experimental techniques for the characterisation of 3D magnetic spin structures are required to advance the performance of nanoscale magnetic technologies. However, as

component dimensions approach the nanometre range, it becomes ever more challenging to analyse 3D magnetic configurations quantitatively with the required spatial resolution and sensitivity. Here, we use off-axis electron holography and MBIR to reconstruct the 3D magnetisation distribution in an exemplary nanostructure comprising an L-shaped ferromagnetic cobalt NW fabricated using FEBID. The approach involves using off-axis electron holography to record tomographic tilt series of electron holograms, which are analysed to reconstruct electron optical magnetic phase shifts about two axes with tilts of up to $\pm 60°$. A 3D magnetisation vector field that provides the best fit to the tomographic phase measurements is then reconstructed, revealing multiple magnetic domains in the NW. The reconstructed magnetisation is shown to be accurate for magnetic domains that are larger than approximately 50 nm. Higher spatial resolution and improved SNR ratio can be achieved in the future by using more specialised electron microscopes, improved reconstruction algorithms, and automation of data acquisition and analysis.

4.1.1. 3D magnetic characterisation

As a result of advances in material characterisation, fabrication and the discovery of increasingly complex spin textures such as skyrmions and hopfions [167], there has been a drive to explore the properties of 3D magnetic configurations. Spintronic circuits that contain integrated magnetic NWs have been proposed for next-generation data storage applications [10] and as physical components for improving machine-learning efficiency [11]. Spintronic computing is being developed due to its energy efficiency compared to capacitor-based electronics [7]. However, most prototypes have been fabricated using 2D lithographic techniques and the 3D stacking that would benefit commercial implementation has not been optimised. For example, magnetic RM prototypes have demonstrated storage and manipulation of data carried by magnetic domains in 2D patterned NWs. Their extension into 3D NW architectures would increase the storage density per unit area [13]. As prototypes of 3D magnetic architectures are developed, experimental measurements of magnetic structure and domain motion are required to guide further development of RM-type technologies. The observables that are used to characterise ferromagnetic samples are related by the equation

$$\boldsymbol{B} = \mu_0(\boldsymbol{H}(\boldsymbol{M}) + \boldsymbol{M}) \ , \tag{4.1}$$

where $\boldsymbol{M}$ is the magnetisation vector field describing magnetic moment per unit volume, $\boldsymbol{B}$ is the magnetic induction and μ_0 is the vacuum permeability. If no external magnetic fields,

conduction currents or displacement currents are present, then $\boldsymbol{H}$ is the demagnetising field, which is defined by the distribution of $\boldsymbol{M}$. It should be noted that, in general, $\boldsymbol{B}$ permeates all of space whilst $\boldsymbol{M}$ is local to the sample. Here, $\boldsymbol{B}$ arises from the $\boldsymbol{M}$ within the sample, therefore reconstructing $\boldsymbol{M}$ gives a compact and simple local configuration. X-ray imaging currently allows 3D reconstruction of $\boldsymbol{M}$ with sub-50-nm resolution using magnetic laminography [168] and sub-70-nm resolution using Fourier transform holography [169, 170]. Theoretical predictions estimate a resolution for X-ray laminography down to 20 nm [31]. In comparison, phase contrast techniques in the TEM cannot be used to reconstruct $\boldsymbol{M}$ directly, but have been used to measure $\boldsymbol{B}$ with a 3D resolution of 10 nm using electron holographic EH-VFT [48, 104, 171]. Micromagnetic simulations are often used to interpret TEM measurements of $\boldsymbol{B}$ [22, 107]. Here, we use the alternative approach of applying MBIR to reconstruct a magnetisation distribution $\boldsymbol{M}$ from experimental TEM measurements that are sensitive to $\boldsymbol{B}$ rather than $\boldsymbol{M}$. We discuss how magnetic and electrostatic signals obtained from electron phase measurements can be used to improve the accuracy of the reconstruction, as well as practical limitations to resolution and accuracy. In summary, previous works have used EH-VFT to reconstruct B in 3D and theorised how M may be reconstructed. This work shows an experimental reconstruction of M in 3D by applying MBIR to an EH-VFT dataset.

4.1.2. Model-based iterative reconstruction of M

The theoretical development of MBIR for the tomographic reconstruction of $\boldsymbol{M}$ from EH-VFT measurements has been described in detail elsewhere [172]. The most common phase contrast techniques for magnetic imaging in the TEM [44, 45, 173–175], which are often collectively termed Lorentz microscopy, all rely fundamentally on an interpretation of the Aharonov-Bohm effect [41], which describes how the phase of an electron wave is affected by electromagnetic potentials. The interaction of an electron wave travelling with a magnetic induction field $\boldsymbol{B}$ results in an electron phase shift φ_{mag}, where

$$\int \boldsymbol{B} \times \mathrm{d}\boldsymbol{z} = \frac{\hbar}{q_e} \boldsymbol{\nabla} \varphi_{mag} \ , \tag{4.2}$$

e is the electron charge, $\hbar$ is the reduced Planck constant, $\mathrm{d}\boldsymbol{z}$ is a path element in the incident electron beam direction and the phase gradient $\boldsymbol{\nabla}\varphi_{mag}$ is defined in a 2D plane perpendicular to the incident electron beam direction. In principle, MBIR can be applied to results obtained using all Lorentz microscopy techniques, as they are all sensitive

to φ_{mag}. Here, the recovery of φ_{mag} from off-axis electron holograms is described in the Methods section. Typically, $\boldsymbol{H}$ fields are present and therefore $\boldsymbol{B}$ and $\boldsymbol{M}$ are not equivalent. For imaging conditions where $\boldsymbol{H}$ results only from the $\boldsymbol{M}$ configuration, magnetic phase effects are considered to arise from the curl($\boldsymbol{M}$) component parallel to the electron beam direction [176]. This curl($\boldsymbol{M}$) component, which can be regarded as an Amperian current, is the origin of the $\boldsymbol{B}$ component that contributes to the electron phase and is associated only with the sample. The $\boldsymbol{M}$ component of magnetic vortex DWs has been measured under such conditions [177], but it required tilting of the sample to evaluate all of the components of curl($\boldsymbol{M}$). The reconstruction error depends on the type of sample, the angular imaging range and the correction of TEM instrument misalignments. If a nanostructure can be tilted incrementally to high angles and φ_{mag} is detected from all parts of the sample, then all the information that is needed for reconstruction can be obtained from the phase measurements. Simulation-based error estimates for this experiment are discussed in the Methods section and Section 5.3.

The workflow for the reconstruction of $\boldsymbol{M}$ (Figure 4.1) includes: 1) Processing and alignment of experimental data to construct a 3D geometrical model of the sample; 2) MBIR reconstruction of the $\boldsymbol{M}$ distribution that best matches the experimental data; 3) Optimal estimation diagnostics for evaluating reconstruction errors. The theory of applying MBIR for $\boldsymbol{M}$ reconstruction has been developed and tested extensively using simulated datasets [178]. The present work is an experimental development, which addresses several sources of error, such as those caused by sample alignment [179], sample drift, and surface damage. It also builds on other previous work on the 3D reconstruction of $\boldsymbol{M}$ from experimental electron microscopy data [180].

4.1.3. Null spaces in electron phase measurement

In Lorentz microscopy, some configurations of $\boldsymbol{M}$ [181] contribute no signal to experimental measurements made in projection and can be described as null spaces, where $\boldsymbol{M}$ may be reconstructed falsely as being close to zero [182]. In such projections, the vector components of $\boldsymbol{M}$ can sum to zero or have non-zero divergence of $\boldsymbol{M}$. In some cases, tilting the sample can reveal the hidden components. However, divergent components can remain undetectable even when tilting of the sample is used. As a result, some configurations of $\boldsymbol{M}$, such as Néel-type magnetic DWs, cannot be reconstructed fully because they contain some states of $\boldsymbol{M}$ that do not create a detectable TEM signal in any projection, as discussed in Section 5.5. It has been experimentally observed [183]

and mathematically proven [182], that Néel-type DWs in both out-of-plane and in-plane magnetised films include eigenstates of the $\boldsymbol{M}$ distribution that do not result in electron phase shift. Such states cannot be reconstructed without making use of additional constraints, and examples of the application of MBIR to such states are discussed in Section 5.5. It should be noted that null spaces are unlikely to be present in the experimental reconstruction described in this chapter because divergent $\boldsymbol{M}$ configurations are not observed in FEBID Co NWs in either this or previous works [31].

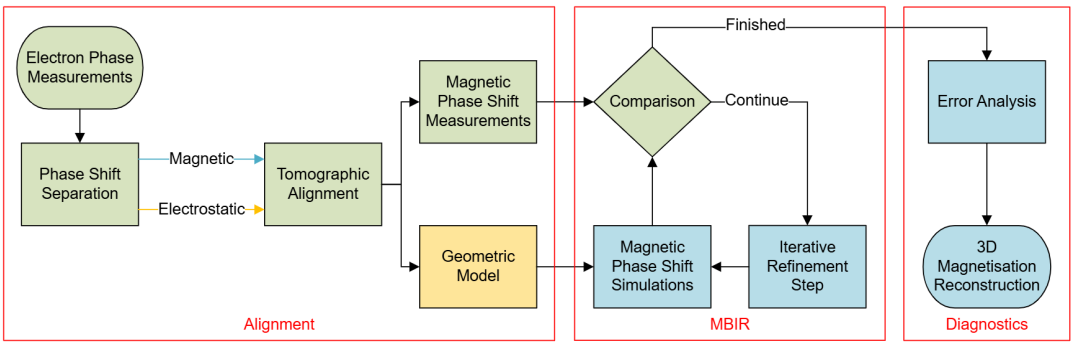

Figure 4.1. Workflow for 3D magnetisation reconstruction. The red boxes indicate the primary processing steps: alignment, reconstruction using MBIR, and diagnostics. The steps are shaded to indicate the data type that is being processed: 2D phase images (green), 3D magnetic vector fields (blue) and a 3D electrostatic scalar field (yellow). Datasets are processed to generate both a geometrical mask that defines where the magnetic material is located and a series of magnetic phase shift measurements corresponding to $\boldsymbol{B}$ field projections. At each iteration, a distribution of $\boldsymbol{M}$ is generated, and then its magnetic phase shift is simulated and compared to the measurements. The iterations are repeated until an optimal $\boldsymbol{M}$ is found. Optimal estimation diagnostics are performed to assess random and systematic errors in the reconstruction. The reconstruction is improved by accurate alignment of the experimental data. Reproduced with permission from [1].

4.2. Methods developed for vector field tomography

4.2.1. Sample fabrication and characterisation

An L-shaped intersection between ferromagnetic cobalt NWs was studied, as it is similar to an element of a 3D RM configuration, in which structural features can act as magnetic DW pinning sites. In order to permit TEM imaging of magnetic states at such pinning sites, free-standing cobalt NWs were fabricated on a copper substrate using focused electron beam deposition (FEBID) in an SEM [42,79]. As shown in Figure 4.2, a precursor

gas is injected into the SEM chamber and cobalt is deposited at locations where the electron beam interacts with the sample. The geometry of the deposited structure is controlled by translating the electron beam in a controlled manner using the SEM scan coils. The structure shown in Figure 4.3a, which consists of two intersecting NWs, was defined using CAD [79] and deposited by electron irradiation of a $Co_2(CO)_8$ precursor in an FEI HELIOS Plasma focused ion beam SEM. Deposition was performed using a 30 kV electron beam with a 690 pA beam current and a 6×10^{-5} Pa chamber deposition pressure. The dimensions and morphology of the sample were determined by imaging the intersection from multiple tilt angles in the SEM, such as the top-down image show in Figure 4.3b. Scanning TEM electron energy-loss spectroscopy (EELS) was used for chemical analysis of the green and red boxed regions marked in Figure 4.3a to obtain an elemental map (Figure 4.3d) and cross-sectional line profiles (Figure 4.3e). The EELS results show that the NW core has a cobalt purity in the range of 45% to 60%, while the surface is covered in a shell of carbon and oxygen. The radial dependence of the cobalt content in the cross-sectional elemental map shown in Figure 4.3e suggests that the deposition was performed in the beam-limited FEBID régime [131], in which the material that receives the highest radiation dose during deposition has the highest purity. Off-axis electron holography was performed to image the local magnetic configuration of the sample. Prior to imaging in the TEM, the sample was saturated magnetically by applying a 1 T magnetic field in the plane of the NW perpendicular to the substrate and relaxed into the magnetic state shown in Figure 4.3c. The magnetic contribution to the phase image records the gradient of the projected in-plane components of $\boldsymbol{B}$, according to Equation 4.2. It is affected by local variations in cobalt purity, projected sample thickness and the orientation of curl($\boldsymbol{M}$). As the present sample contains a head-to-head magnetic DW with a vortex configuration, tomographic reconstruction is needed for full magnetic characterisation.

4.2.2. Electron holographic vector field tomography

In this work, off-axis electron holography [37] is chosen as the preferred magnetic characterisation technique because it retrieves the electron phase shift directly and has a high phase sensitivity of 0.016 radian RMS noise for a 10 s exposure time per phase image. It also causes minimal sample damage when using a low electron flux of 200 e/nm^2/s. Tilt series of off-axis electron holograms for EH-VFT were recorded using an FEI Titan G2 60-300 TEM at 300 kV. A voltage of 100 V was applied to the biprism, resulting

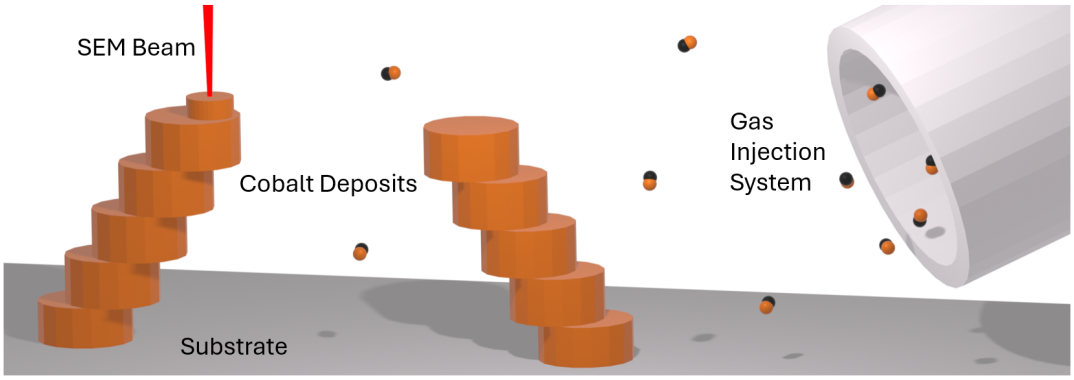

Figure 4.2. FEBID in a SEM. Cobalt is deposited locally where the electron beam interacts with solid material. The electron beam is translated to control the location of the deposited material. Reproduced with permission from [1].

in electron holograms (Figure 4.4a) with an interference fringe spacing of $\sim$3.1 nm, as shown in the left inset to Figure 4.4a. The phase shift (Figure 4.4b) was determined from the inverse FFT of one of the sidebands of each hologram, as shown in the right inset to Figure 4.4a [37, 159, 160]. At each sample position, five holograms with individual exposure times of 2 s were recorded and the corresponding phase images were averaged to reduce the effects of statistical noise. A large TEM pole-piece gap ($\sim$11 mm) and a dedicated tomography holder [179] allowed the sample to be tilted by 360° about the holder axis without removing it from the microscope.

Tilt series of off-axis electron holograms were recorded at 10° tilt increments over two orthogonal arcs. The effective maximum tilt angles were limited to between -60° and 30° and to between -60° and 0°, as the sample was shadowed by the holder and the substrate. At the end of each arc, the sample was inverted relative to the beam and recorded a second time to enable phase shift separation, which will be described later. The second tilt series was recorded to reduce missing wedge artefacts and to prevent projection-based null spaces [182]. Simulations of samples comprising uniformly magnetised NWs and vortex configurations have shown that the use of smaller tilt increments has a negligible impact on reconstruction quality [178]. Furthermore, simulations presented in Chapter 5.4 show that if a 10% difference between the volumes of the sample and its geometrical model is assumed, then the difference between the reconstruction of $\boldsymbol{M}$ and the ground truth is, on average, less than 10% per voxel. In order to separate the electrostatic and magnetic contributions to the phase images, off-axis electron holograms were recorded before and after turning the sample by 180°. This approach changes the sign of the

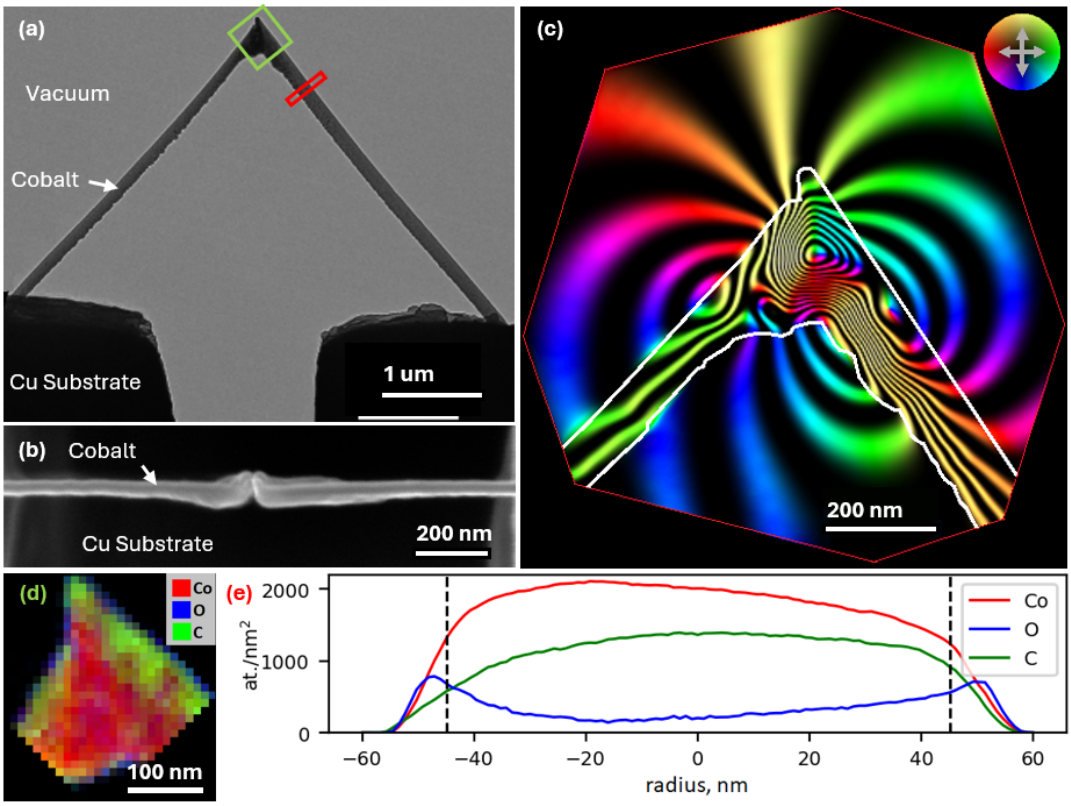

Figure 4.3. Dimensions, morphology and chemical analysis of an L-shaped cobalt nanostructure fabricated using FEBID.(a) Bright-field TEM side-view image. The marked regions correspond to the elemental map (green) and cross-sectional line profile (red) shown in (d) and (e), respectively. (b) SEM top-down image of the tip of the sample. (c) Magnetic phase contour image recorded using off-axis electron holography, displayed as $\cos(6\varphi_{mag})$. The colours show the direction of the projected in-plane $\boldsymbol{B}$ field. The sample outline is marked. (d) EELS elemental map of the tip, showing the distributions of Co, O and C. (e) Cross-sectional EELS elemental line profile, showing that the central 90 nm of the NW has a cobalt content of between 45% and 60%. Reproduced with permission from [1].

magnetic contribution to the total phase shift, based on the expression [41, 184],

$$\begin{aligned} \varphi(x,y) &= \varphi_{el}(V) + \varphi_{mag}(\boldsymbol{A}) \\ &= \frac{2\pi q_e}{\hbar v}\int V(x,y,z)\mathrm{d}z + \frac{2\pi q_e}{\hbar}\int \boldsymbol{A}(x,y,z)\cdot \mathrm{d}\boldsymbol{z}\ , \end{aligned} \tag{4.3}$$

where $\varphi_{el}(V)$ and $\varphi_{mag}(\boldsymbol{A})$ are the electrostatic and magnetic contributions to the phase shift, respectively, v is the relativistic electron speed and $\mathrm{d}z$ and $\mathrm{d}\boldsymbol{z}$ are scalar and vector elements of the electron path, respectively. For a pair of such reversed holograms, half of the sum and half of the difference of the measured phase images represent φ_{el} and

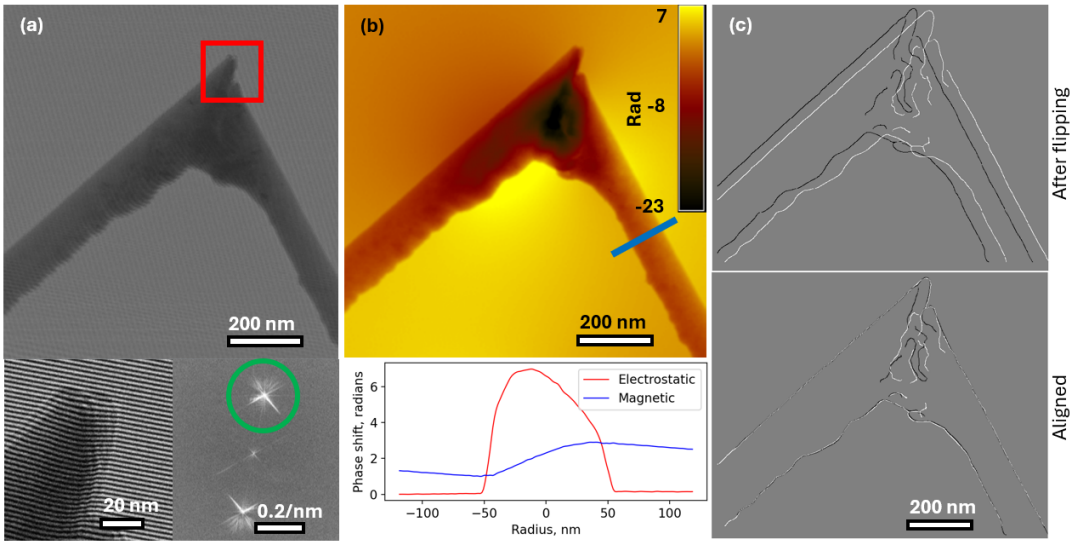

Figure 4.4. Off-axis electron holograms and alignment of phase images. (a) Off-axis electron hologram formed by the interference of two electron waves, one of which has passed through the region of interest on the sample. The insets show a magnified version of the region inside the red box (lower left) and an FFT of the electron hologram (lower right). The green circle in the FFT marks the sideband that was used to used to calculate (b). (b) Total phase image obtained from an inverse FFT of the sideband. The inset shows a line profile of the electrostatic and magnetic contributions to the total phase shift along the blue line. (c) Steps in the alignment of phase images recorded before and after flipping the sample by 180° to separate the electrostatic and magnetic contributions to the phase. Image distortions resulting in misalignment (top) are corrected by applying an affine transformation (bottom). Reproduced with permission from [1].

φ_{mag}, respectively. Unfortunately, physically turning the sample over by 180° introduces misalignments between the phase images. These misalignments were corrected by using an automated Python script to identify matching features at the sample edges [185–187]. Linear distortions caused by the misalignment of the electron optical system of the TEM were corrected by using an affine transformation to provide an optimal match between the edges of each phase image pair, as shown in Figure 4.4c. In the present study, the images were found to be elongated by 2% in a direction that forms a 75° angle with the tilt axis by tilting a calibration sample by 180° and tracking fiducial markers. By applying the affine transformation, phase separation artefacts were reduced to below the noise level, such that they were not detectable in line profiles. This approach ensures a consistent separation of φ_{el} and φ_{mag}, as shown in the inset to Figure 4.4b. It should be noted, that all necessary software packages are listed in Appendix A, examples of

intermediate steps of the hologram-to-phase calculation are shown in Chapter 2.6, and the processing steps of phase shift separation are illustrated in Figure 4.5.

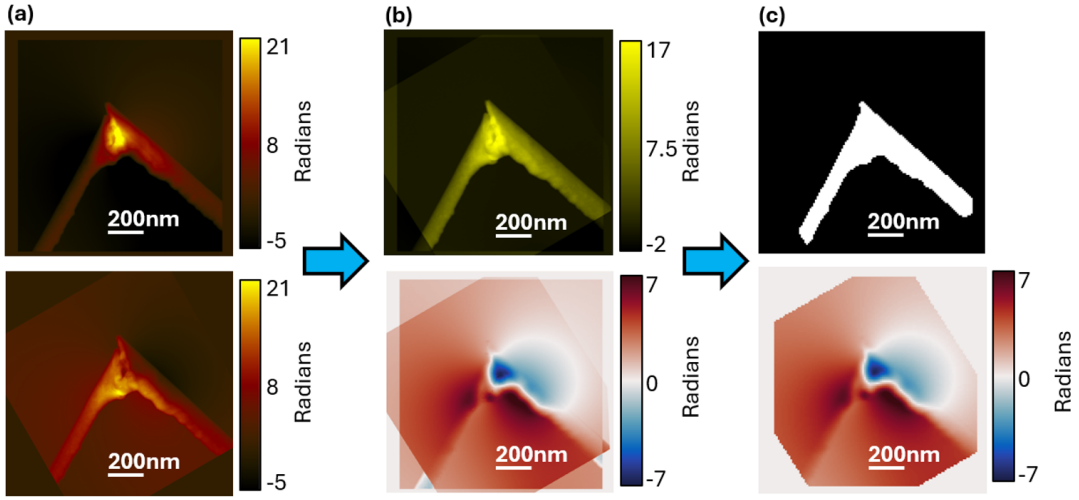

Figure 4.5. Separation of electrostatic and magnetic electron phase shift. (a) Total phase shift images at -3.7° tilt (top) and 176° tilt (bottom). Both images were rotated such that the electron beam is out-of-plane, and have been aligned with sub-pixel precision using the edge detection method. (b) The images in (a) are added & divided by two to calculate φ_{el} (top), and subtracted & divided by two to calculate φ_{mag} (bottom). (c) Both images are further processed before reconstruction with MBIR. A threshold is applied to the φ_{el} to define the sample outline (top). φ_{mag} is rebinned from 0.65 nm pixel size to 10.2 nm pixel size to reduce reconstruction computation time, and the overlap region of images in (a) is set as the confidence mask. Reproduced with permission from [1].

4.2.3. Alignment of phase images

As each φ_{mag} image can have non-rectangular borders or include pixels at which the hologram-to-phase calculation resulted in errors, a confidence mask was used to identify the areas in each image that contain φ_{mag} measurements. The φ_{el} image was first flattened to remove background ramps resulting from effects such as electron-beam-induced charging and the perturbed reference wave. A threshold was then used to define a mask that identified where the sample is located at each tilt angle. If elemental mapping was performed, as shown in Figure 4.3e, then the threshold could be fine-tuned to include only ferromagnetic material in the mask. These binary masks were used for aligning the phase images in each tilt series.

Since the present phase images have a spatial resolution of no better than 6 nm due to the chosen hologram fringe spacing, tomographic reconstruction was found to be highly sensitive to small image misalignments. Furthermore, the sample orientation was not known precisely during acquisition, as only relative tilt angles between phase images $\Delta\theta_i$ were measured. The projection positions shown in Figure 4.6a were therefore refined by using an axial-symmetry-based implementation of the common lines method [188]. As illustrated in Figure 4.6b, at every sample tilt angle $\Delta\theta_i$ there is a unique projection orientation α_i, and the two are related *via* geometrical parameters: ϕ is the observed detector rotation relative to the sample tilt axis; θ_0 is the starting tilt of the sample; α_0 is the sample orientation at 0° tilt. α_i can be measured by finding the sample symmetry axis from the electrostatic phase maps, as shown in Figure 4.6c. The equation

$$\tan(\alpha_i + \phi) = \tan(\alpha_0 + \phi)\cos(\theta_0 + \Delta\theta_i) \tag{4.4}$$

is then true for all projections and can be solved to find unknown constants (α_0, ϕ, θ_0) defining the absolute sample orientation. For a single tilt series $i \in [1, \ldots, n]$ and, if the number of projections $n > 3$, the system of equations is over-defined and can be solved numerically by using multivariate minimisation [189]. Once they have been aligned, the electrostatic phase images can be back-projected to compute a scalar CT reconstruction, as shown in Figure 4.6d, which defines the geometry of the sample. In order to correct for missing wedge artefacts, the geometrical model (Figure 4.6d) can be cropped to match the sample dimensions observed in the SEM images (Figure 4.3b). The refined model is used in the reconstruction of $\boldsymbol{M}$ to define where the magnetic material is located. As the alignment algorithm is imperfect, blurring of features is observed and the 3D spatial resolution of the CT reconstruction is poorer than the 6 nm 2D resolution of the phase images. As using a smaller voxel size did not improve the resolution of $\boldsymbol{M}$, the reconstruction uses a 10.2 nm voxel size.

4.2.4. Three-dimensional reconstruction of $\boldsymbol{M}$

In order to reconstruct the 3D distribution of $\boldsymbol{M}$, a forward model was used to simulate tilt series of magnetic phase images based on the geometrical 3D model of the sample (Figure 4.6d) [190]. In order to determine the best-fitting values of $\boldsymbol{M}$ in the model that would simultaneously satisfy all of the magnetic phase measurements, a cost function that

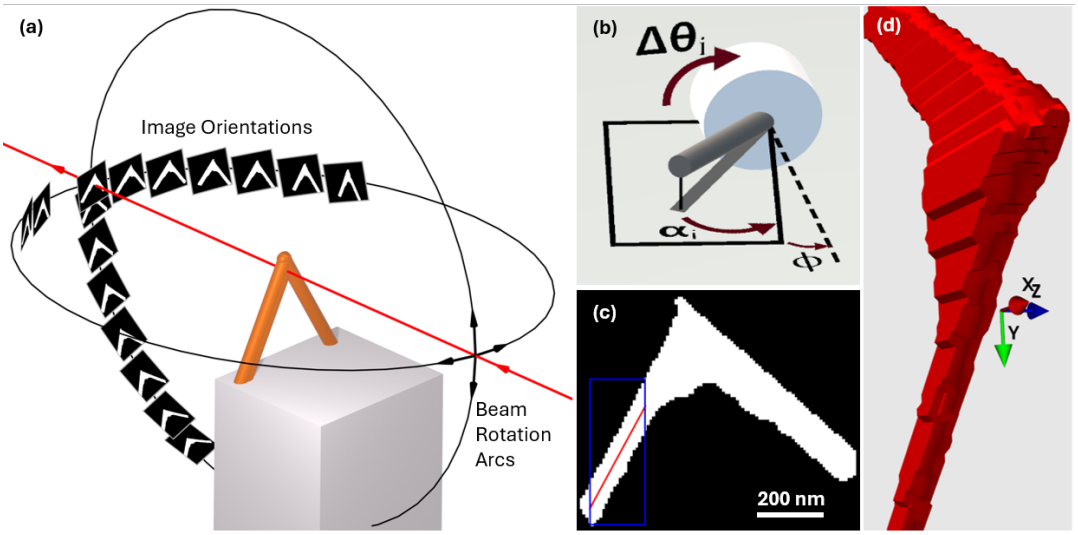

Figure 4.6. Alignment of tilt series of phase images and generation of a 3D geometrical model of the sample. (a) Schematic diagram showing the angular position and sample outline of each magnetic phase image used in the reconstruction. The direction of the electron beam is shown in red. The arcs of rotation of the sample are shown in black. (b) Rotations that define the projections for a conically-symmetrical element, showing the sample tilt $\Delta\theta_i$, the projection direction α_i and the rotation between the detector and the tilt axis ϕ. (c) The centre of an axially-symmetrical part of the sample can be identified in each projection and used to align the projections. (d) 3D tomographic reconstruction of the masks in the aligned projections performed to generate a model representing the sample geometry. A 10.2 nm voxel size was used because features smaller than 10x10x10 nm cannot be resolved due to tomographic misalignment and using smaller voxel sizes would not improve the spatial resolution. Reproduced with permission from [1].

could be minimised to determine the closest fit was defined according to the expression

$$\begin{aligned} C = &\sum_i \left(\varphi_{i,meas} - \varphi_{i,sim}(\boldsymbol{M})\right)^2 \\ &+ \lambda_1 \sum_j (\boldsymbol{\nabla} M_j \cdot \boldsymbol{\nabla} M_j) + \lambda_2 \mathrm{var}(|\boldsymbol{M}|) \ , \end{aligned} \tag{4.5}$$

where C is the cost to minimise, M_j are the magnetisation vector field components, φ_i are the phase image pixels, λ are the regulariser weights, $\boldsymbol{\nabla}$ is the gradient operator and "var" is the variance operator. As there are multiple equivalent solutions, regularising terms were added to favour solutions that exhibit a low gradient and a low variance in the magnitude of $\boldsymbol{M}$. The low gradient was chosen to favour ferromagnetic solutions,

while the low variance was chosen to favour solutions comprising similar materials. The cost function was minimised by using a CG method [191] and initialised with $\boldsymbol{M} = 0$. The regulariser weights (λ in Eq. 4.5) could be varied over 3 orders of magnitude and the reconstruction retained the same features, confirming that the solution was measurement-based. The reconstructed 3D distribution of $\boldsymbol{M}_{rec}$ was obtained for $\lambda_1 = 1$, which is the minimum value needed to lift the degeneracy between ferromagnetic and ferrimagnetic order, while $\lambda_2 = 0.1$ reduces surface artefacts without affecting the rest of the reconstruction.

Figure 4.7a shows that the sample cotains multiple magnetic domains and that the magnitude of $\boldsymbol{M}_{rec}$ is greatest at the lower part of the intersection (denoted by the length of the arrows), in agreement with the radial cobalt distribution shown in Figure 4.3e. In order to view the positions of magnetic DWs inside the structure, angles between pairs of neighbouring vectors were computed. The maximum angles are shown in Figure 4.7b. An angle of $\sim 90°$ identifies the core of the vortex DW, while the dashed blue line shows the direction of the core, which corresponds to the curl($\boldsymbol{M}_{rec}$) direction in sub-volumes around the vortex core. The magnetic vortex state occupies the full ~ 200 nm x 200 nm x 100 nm volume of the NW intersection. The U-shaped vortex core has a length of 350 nm. Figure 4.7c-d shows z slices extracted from $\boldsymbol{M}_{rec}$ at the full resolution of the reconstruction, containing intersections with the vortex magnetic DW.

4.2.5. Diagnostics of the reconstruction

The influence of noise on the resolution of the reconstruction was assessed by using a Fourier shell correlation. This approach involved halving the 3D $\boldsymbol{M}_{rec}$ dataset through random sampling and interpolating the missing values. Figure 4.8 displays an estimate of the SNR per spatial frequency band in the 3D reconstruction volume. The correlation is plotted relative to the $\frac{1}{2}$ bit SNR threshold commonly used in X-ray tomography [192]. It reveals that any feature larger than 14.8 nm has sufficient SNR to be interpreted directly. The resolution limit of ~ 1.5 pixels due to noise is regarded as conservative, since noise is suppressed in regularised reconstructions. Hence, systematic uncertainties are also considered. If the angle between neighbouring atomic spins is larger than 30°, then the micromagnetic energy expressions are no longer valid [22]. The maximum spin angle in Figure 4.7b corresponds to the positions of DWs and suggests that the calculations are valid in most of the sample, although voxels at the core of the vortex are not resolved.

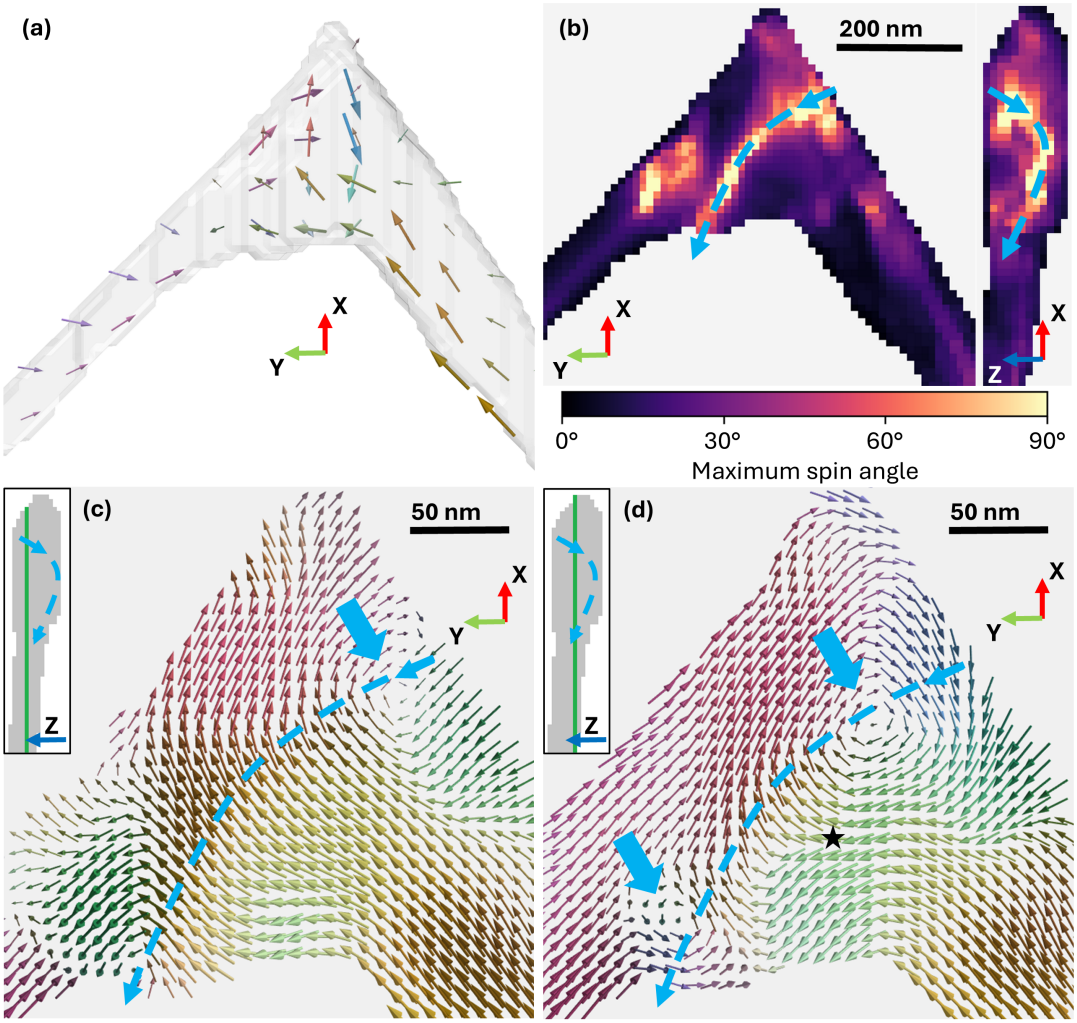

Figure 4.7. Reconstructed 3D magnetisation distribution M_{rec} in the cobalt nanostructure. The reconstruction is a 3D vector field, which maps the directions and magnitudes of the magnetic moments inside the sample. (a) 3D $\boldsymbol{M}_{rec}$ vector field. (b) Maximum angle between neighbouring spins, projected along the z and y axes. The dashed lines follow the core of the vortex-type magnetic DW. (c, d) Single-plane slices of the $\boldsymbol{M}_{rec}$ vector field shown with full spatial resolution. The insets mark the locations of the slices. The vortex core is marked as in (b). Blue arrows mark where the slices intersect the vortex core, which intersects the top slice (c) once and the bottom slice (d) twice. The star in (d) denotes a voxel selected for diagnostics of the reconstruction. Reproduced with permission from [1].

Other uncertainties can be identified by using optimal estimation diagnostics [193], by assuming that all $\boldsymbol{M}$ vectors and phase image pixels have probability density functions that can be described by a normal distribution. The reconstructed magnetisation $\boldsymbol{M}_{rec}$ can be expressed as the true distribution of $\boldsymbol{M}$ transformed by an averaging kernel matrix

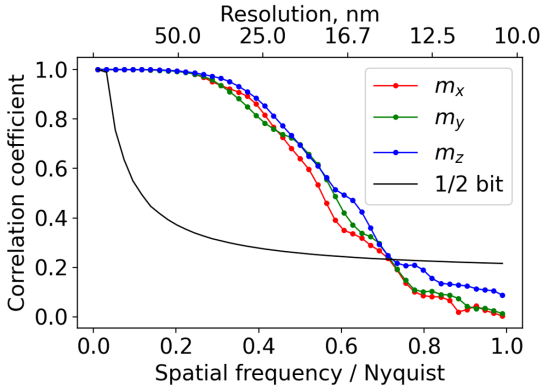

Figure 4.8. Fourier shell correlation. Evaluation shows that reconstructed features larger than 14.8 nm can be interpreted directly. Reproduced with permission from [1].

A, which is further affected by measurement errors ϵ, according to the error gain matrix G:

$$\boldsymbol{M}_{rec} = A\boldsymbol{M} + G\epsilon \ . \tag{4.6}$$

A and G were determined for the $\boldsymbol{M}_{rec}$ vector denoted by a star in Figure 4.7d, which has $\mu_0 M_s = 0.78$ T and is well resolved with a maximum spin angle of 13°. G is used for linear error propagation because it expresses the error on a single $\boldsymbol{M}_{rec}$ vector as a function of error on every pixel in experimental phase measurements. The phase measurement noise of 0.016 rad per pixel was determined by calculating the standard deviation of the vacuum measurements and is mapped by G to a $\mu_0 M_s$ error of 0.001 T. The experimental and simulated phase images used in the cost function in Eq. 4.5 cannot match perfectly due to experimental misalignments, resulting in a residual distribution Figure 4.9 corresponding to a RMS error of 0.38 rad. Forcing the reconstruction to match any one image perfectly would, on average, introduce a perturbation that maps to a $\mu_0 M_s$ error of 0.009 T. A is a measure of spatial averaging during the reconstruction and shows that, in order to calculate a single $\boldsymbol{M}_{rec}$ vector, information is taken from a volume around the central position, as illustrated in Figure 4.10. For this voxel, the point spread function has an average FWHM of 43 nm. The evaluation of A is equivalent to changing the value of one voxel of $\boldsymbol{M}_{rec}$ and repeating the reconstruction to quantify systematic errors. As error propagation and perturbation mapping for other voxels yields similar results, the $\mu_0 M_s$ measurement precision is determined to be 0.01 T per pixel and the spatial resolution to be better than 50 nm.

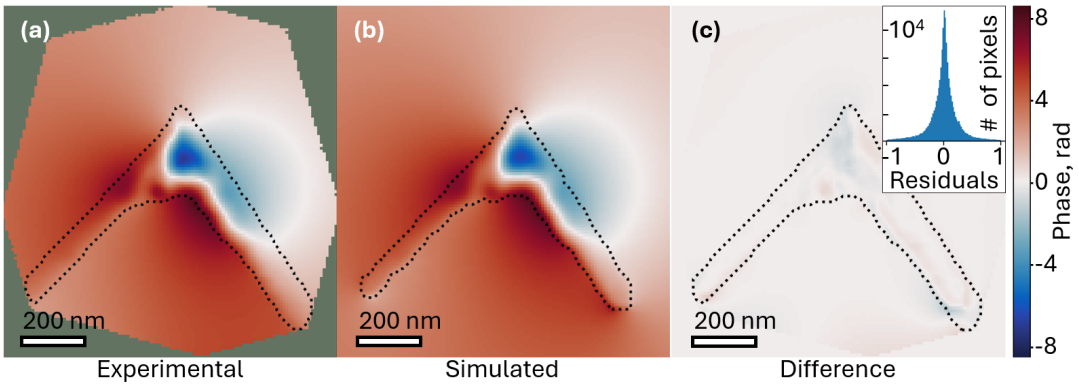

Figure 4.9. Magnetic phase shift reconstruction for a sample tilt angle of -3.7°. (a) Experimental magnetic phase image. (b) Magnetic phase image calculated from the reconstructed magnetisation distribution. (c) Difference between (a) and (b). The inset shows the distribution of residual differences for magnetic phase images at all tilt angles. The residuals are used to estimate the $\boldsymbol{M}_{rec}$ reconstruction uncertainty. Reproduced with permission from [1].

For the present dataset, it would have been possible to perform the reconstruction with a voxel size of 5.1 nm instead of 10.2 nm. However, smaller voxels would have been affected more strongly by noise and phase image misalignments, resulting in reduced precision per pixel. During reconstruction, gradient regularisation is needed to obtain ferromagnetic solutions. However, it also suppresses noise, applies smoothing to sharp features, and can be adjusted to vary the trade-off between precision and spatial resolution. If the precision for smaller voxels were to be increased to 0.01 T by adjusting the regulariser weights, it would result in a similar spatial resolution, which is largely independent of voxel size for voxels smaller than 10 nm. This behaviour is attributed to remaining uncorrected phase image misalignments, which result in the smoothing of features in the reconstruction. By using a 10.2 nm voxel size, the MBIR algorithm computes a reconstruction in 3 hours using one core of an Intel i7 CPU. The algorithm optimisations are discussed in the Chapter 5.2. Achieving a higher resolution would require more advanced image drift and distortion correction, optimised reconstruction software that computes faster, and the cumulative acquisition of larger datasets.

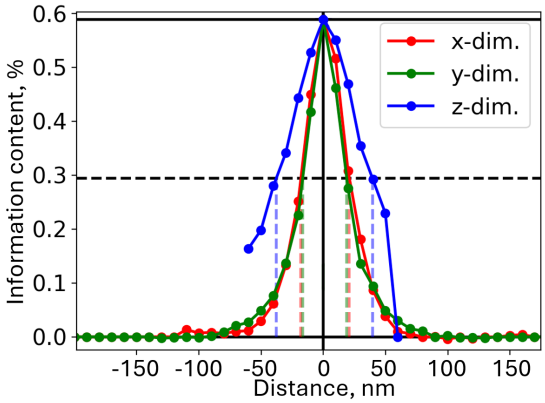

Figure 4.10. 3D point spread function, showing the spatial distribution of information content for the voxel denoted by a star in Figure 4.7d. For the present dataset and reconstruction procedure, the information contained at this point in space is spread over a volume with an average FWHM of 43 nm, in part due to computational limitations. Reproduced with permission from [1].

4.3. Numerical accuracy of three-dimensional magnetisation reconstruction

4.3.1. Uniform region reconstruction

As described in the preceding section, EH-VFT and MBIR were used to record and reconstruct the 3D distribution of $\boldsymbol{M}_{rec}$ in a sample comprising two intersecting NWs. Figure 4.3e shows that the NWs contain a mixture of cobalt and organic compounds, which transitions from a 60% cobalt content in the core to a pure carbon shell at the surface. Since the cobalt is dispersed within the carbon matrix in nanocrystalline form [140] and bulk cobalt has $\mu_0 M_s = 1.75$ T [140], the NWs should exhibit $\mu_0 M_s < 1.1$ T, as observed for the NW distribution in Figure 4.11. The few outliers with $\mu_0 M_s > 1.1$ T are likely to be artefacts at the interface between the magnetic material and the vacuum region, where magnetic voxels that are designated as non-magnetic force the reconstruction to increase the value of M_s locally. In other parts of the sample, surface voxels contain non-magnetic material where M_s is close to zero. Surface reconstruction artefacts are present in part because missing wedge correction for the geometrical model is not perfect, as discussed in the Chapter 5.4. The threshold for creating the 3D geometrical model shown in Figure 4.6d was refined after the first reconstruction, so that similar amounts of over- and underestimating surface artefacts were present. A discussion of the threshold for the geometrical model and a line trace showing surface artefacts are included in

Figure 4.12. Such surface artefacts are also identifiable for the full sample, as voxels with $\mu_0 M_s > 1.75$ T, as shown in the histogram in Figure 4.11. Such errors could be reduced in the future by using smaller voxels and improved tomographic alignment and distortion removal algorithms. Both NWs have single magnetic domain configurations at a distance of 200 nm from the intersection, with $\mu_0 M_s = 0.7 \pm 0.2$ T in the left NW and $\mu_0 M_s = 0.5 \pm 0.2$ T in the right NW. M_s has previously been measured for varying cobalt contents of FEBID NWs [140,194], but the measurements were corrected to exclude the non-magnetic shell. The latter correction can be replicated by assuming that in Figure 4.3e the compositional line profile corresponds to a circular-cross-section NW with a 100-nm-diameter magnetic core, resulting in an estimated average cobalt content of 61% with 4% standard deviation, which would correspond to $\mu_0 M_s = 0.5 \pm 0.1$ T. The reconstructed value of $\boldsymbol{M}_{rec}$ is consistent with the predicted values, but shows a higher standard deviation due to surface artefacts.

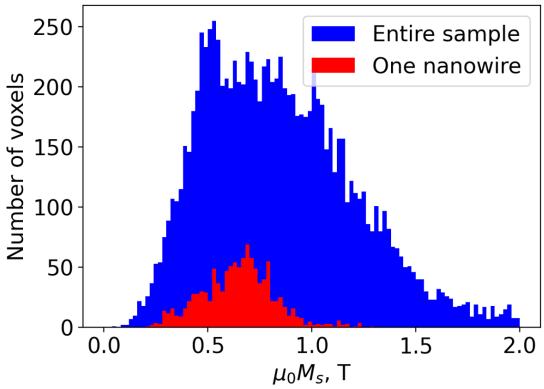

Figure 4.11. Distribution of magnitudes of the reconstructed magnetisation distribution $\boldsymbol{M}_{rec}$. Shown for all of the voxels in the sample in blue and for the voxels in the NW on the left side of Figure 4.7a in red. The bin size is 0.02 T. The distributions result from material composition variations and reconstruction artefacts. Reproduced with permission from [1].

4.3.2. Multi-domain reconstruction

The primary advantage of reconstructing $\boldsymbol{M}_{rec}$ is to allow the visualisation of local variations in magnetic domains and the twisting of magnetic DWs. Figure 4.7a and Figure 4.3c are projected along the z axis. The close-to-anti-parallel $\boldsymbol{M}_{rec}$ vectors in Figure 4.7a explain the phase shift variations at the NW intersection in Figure 4.3c. The curl($\boldsymbol{M}_{rec}$) direction in Figure 4.7b shows that in Figure 4.3c only part of the vortex has its curl oriented close to the z axis, while the other part is more in-plane and requires

imaging about a second tilt axis for a sufficient signal to be detected. The magnetic vortex core is curved to favour its positioning at the protrusion at the bottom of the intersection, which is considered to be a DW pinning site. The limited spatial resolution is evident in Figure 4.7c, where the vortex core has a lower value of M_s than the surrounding material due to spatial averaging of vector components of opposite sign. This averaging is a result of the regularisation in Eq. 4.5, in which the preferential selection of solutions with low gradients introduces smoothing. Although this smoothing is necessary to constrain solutions for $\boldsymbol{M}_{rec}$ to retain ferromagnetic ordering, the averaging of anti-parallel vectors offsets M_s values at the vortex core. In the present experiment, the M_s offset due to spatial averaging is negligible when compared to variations in material composition. The elemental map shown in Figure 4.3d indicates that the cobalt content at the intersection is elevated to $70 \pm 15\%$, with a predicted $\mu_0 M_s = 0.8 \pm 0.5$ T [31, 140, 194], in close agreement with the value of $\mu_0 M_s = 0.9 \pm 0.3$ T measured from the reconstruction. The correlation between M_s and atomic Co content agrees with previous work, and the distributions are shown in the supplementary Figure 4.12. The magnetic DW occupies the full box ~ 200 nm width of the intersection, which is comparable to the ~ 100 nm magnetic DW width of transverse head-to-head DWs that previously observed using magnetic X-ray laminography in 80% purity FEBID cobalt NW double helixes [31]. In summary, MBIR has provided accurate measurements of M_s for a U-shaped vortex magnetic DW of width 200 nm, but is less sensitive to sub-50 nm M_s variations in the present study due to limitations in spatial resolution and sensitivity that can be overcome in future experiments.

4.4. Applicability of EH-VFT reconstruction to other datasets

4.4.1. Algorithm improvements

The 3D spatial resolution of the reconstruction could be improved significantly by reducing the voxel size, as this would reduce the extent of spatial averaging. Since imposing ferromagnetic ordering requires a comparison of neighbouring voxels, the resolution is limited to approximately three times the voxel size. Therefore, a 3D resolution of 3 nm would be possible if a 1 nm voxel size were used. Such a resolution improvement would increase the computation time by a factor of one thousand. However, the MBIR algorithm

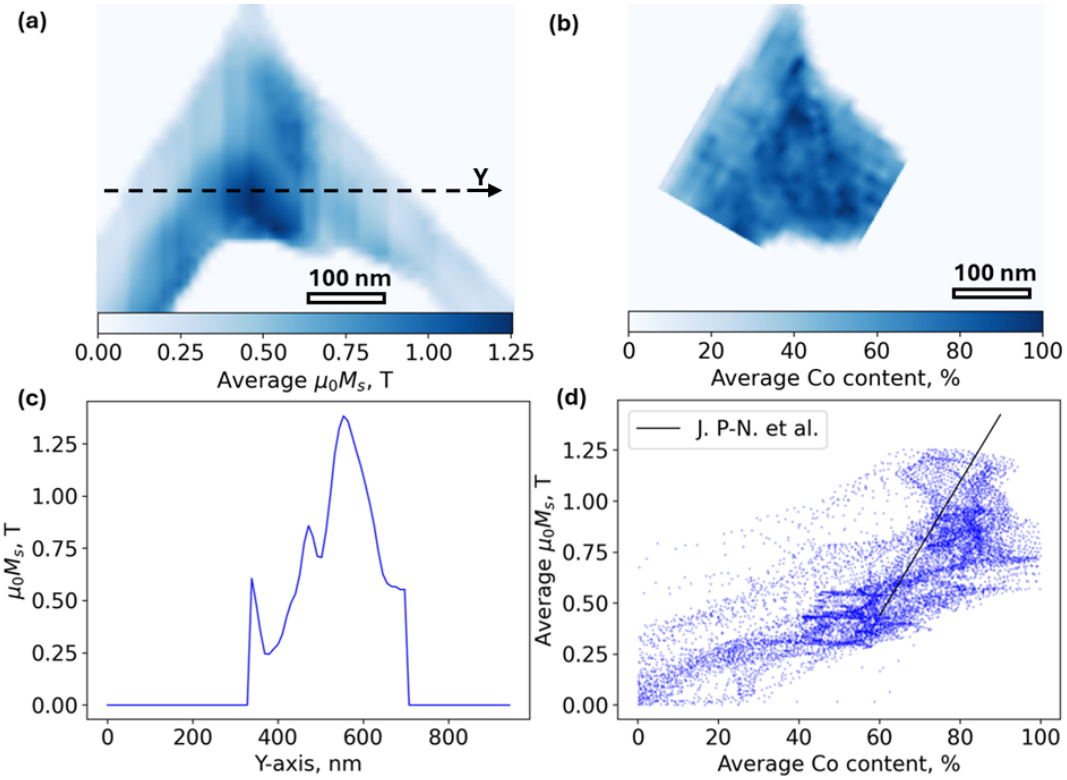

Figure 4.12. Correlation between $\boldsymbol{M}$ reconstruction and EELS mapping. (a) Average $\boldsymbol{M}$ magnitude projected at 0° tilt. (b) EELS scan showing projected Co atomic content at 0° tilt. The image was interpolated and rotated to match the scale and number of pixels in image (a). (c) Linetrace showing $\boldsymbol{M}$ magnitude for one line of voxels in the reconstruction. The z-coordinate of the line trace is in the centre of the reconstructed volume, and the x-coordinate position and y-coordinate extent correspond to the dashed line in image (a). (d) correlation between overlapping pixels in images (a) and (b). The data points are semi-transparent to show overlap, and a calibration between the atomic Co content and $\boldsymbol{B}$ in high-aspect-ratio FEBID NWs [140] is shown in black. (c) shows an artefact on the left side, which is attributed to surface digitisation and is believed to be the result of general tomographic misalignment. If the geometrical model were too small, artefacts on both sides would be expected. The majority of data points in (d) are close to predictions from previous work, and there are similar amounts of under- and over-estimates attributed to artefacts in reconstruction or alignment of images (a) and (b). The points showing non-zero M_s when Co content is less than 40% do not follow the expected trend and are believed to correspond to areas where ferromagnetic and paramagnetic materials overlap in projection, or regions where inaccurate values are assigned to vacuum due to limited spatial resolution. Overall, most reconstructed data points agree with previous works, even though some artefacts are present. Reproduced with permission from [1].

can be parallelised to benefit from computing on dedicated servers and CG minimisation could be optimised by a linear least squares solver to reduce the number of minimisation steps if the variance regularisation in Equation 4.5 was removed [189]. The current symmetry-based tomographic alignment shows up to 10 nm image alignment errors when applied to samples comprising more than a single cylindrical NW. More general algorithms would be suitable for other samples [188, 195]. Off-axis electron holography can provide measurements of phase shift with sub-nm spatial resolution by reducing the interference fringe spacing on a dedicated electron microscope [37], ultimately with atomic spatial resolution in magnetic-field-free conditions [39].

4.4.2. Outlook

The present study provides a quantitative reconstruction of the 3D distribution of $\boldsymbol{M}$ for a cobalt nanostructure using EH-VFT. Similar datasets have previously been used to reconstruct 3D distributions of $\boldsymbol{B}$ [48, 49, 105]. 3D reconstructions of $\boldsymbol{M}$ were tested for a range of NWs of varying purity. A NW intersection was chosen for this paper, as it combines the complexity arising from the non-uniformity of the material with the possibility of projection-based null spaces from a 3D vortex magnetic DW. The reconstruction is shown to be accurate based on 16 projections with a 10° angular spacing over two tilt axes with sub-50-nm spatial resolution. For other nanostructures, the reconstruction of $\boldsymbol{M}$ is likely to be possible if the following conditions are met:

- The sample geometry must be defined. Errors arising from an inaccurate geometrical model are discussed in Chapter 5.4.
- The phase shift arising from all components of $\boldsymbol{M}$ must be measured. In general, two complete tilt series are necessary. In the case of uniform NWs and vortex states, lower tilt ranges are viable, but the reconstruction error is then increased, as discussed in Chapter 5.3.
- There should ideally not be external magnetic fields, or conduction or displacement currents, in the sample, in order to ensure that the measured phase shift is solely due to $\boldsymbol{M}$.
- The sample must be ferromagnetic. This is a requirement for the MBIR algorithm.

If null spaces are present, then they only affect the corresponding sub-volume, as discussed in Chapter 5.5. The ferromagnetic nanostructure shown in this paper satisfies the above

conditions because the sample dimensions were measured during fabrication and were used to correct for missing wedge artefacts in the geometrical model, while the configurations of $\boldsymbol{M}$ that are present in the sample do not create null spaces and can, in principle, be reconstructed with an error of less than 1% when imaged over $\pm 60°$ tilt arcs. I addition, the sample is isolated from other material that may accumulate charge or be magnetised.

Previous works have shown 2D reconstructions of $\boldsymbol{M}$ [196, 197], while an alternative MBIR implementation [180] has provided only a qualitative 3D reconstruction. Micromagnetic simulations [69, 107] are a common approach to 3D quantification, but require a knowledge of the magnetic properties of the material, whereas MBIR can, in special cases, reconstruct $\boldsymbol{M}$ without such prior knowledge. Quantitative measurements have been reported using both X-ray and neutron tomography [30, 31, 168–170], with a spatial resolution of 50 nm for X-ray laminography. MBIR results agree with X-ray tomography and micromagnetic simulations of similar FEBID nanostructures [31]. When computational limitations are resolved to improve spatial resolution, MBIR would be uniquely suited to characterise 3D magnetic nanostructures, such as NW junctions, interfaces in nanoparticles, Bloch-type skyrmions on curved surfaces, and hopfions. In total, this method reconstructs projections of $\boldsymbol{B}$, projections of electrostatic potential, 3D distributions of $\boldsymbol{M}$, and 3D geometry of nanostructures.

4.5. Conclusions

MBIR has been applied and further developed to measure the 3D distribution of magnetisation $\boldsymbol{M}$ in a FEBID ferromagnetic nanostructure from multiple projections of the magnetic induction field recorded using off-axis electron holography. The effect of null space limitations on the uniqueness and accuracy of the reconstruction has been assessed. The results agree with X-ray tomography of similar structures. Optimal estimation diagnostics show that the reconstruction has a precision of 0.01 T at each voxel. The present spatial resolution of several tens of nanometres is restricted primarily by computational limitations and can be improved greatly in future experiments (towards the atomic scale) by using a smaller voxel size, more specialised electron microscopes, and improved image processing.

Chapter 5.

The Feasibility and Interpretability of Model-Based Iterative Reconstruction of Magnetisation in Three Dimensions

"After a little algebra."
— Edmundas Kuokštis, 2015

5.1. Introduction

The mathematical derivation of 3D magnetisation reconstruction assumes that projections are acquired over two orthogonal 360° arcs, and that $\boldsymbol{M}$ is mostly non-divergent [178]. In practice, these assumptions may not be met, which can introduce statistical uncertainty into the reconstruction or create artefacts. Therefore, simulations are used to evaluate the types of errors that arise when performing MBIR with imperfect datasets. In this chapter, models of common nanostructures are generated, the corresponding EH-VFT datasets are simulated with a limited number of projections, MBIR is performed, and the reconstructions are compared with ground truth. Hence, it is shown how numerical accuracy is affected by limited sample tilt ranges, 3D geometric model precision, and null spaces.

5.2. MBIR simulation framework

Fundamentally, MBIR is a least-squares fitting algorithm that was optimised for the simultaneous fitting of millions of discrete magnetic moments, equivalent to a $\boldsymbol{M}$ distribution in 3D space. During MBIR, a forward model F is used to calculate a tilt series of simulated magnetic phase images that correspond to a magnetisation distribution $\boldsymbol{M}$ [190].

$$\varphi_{1,calc},\ \ldots,\ \varphi_{n,calc} = F(\boldsymbol{M}). \tag{5.1}$$

Conversely, if $\boldsymbol{M}$ is not known and phase shift measurements $\varphi_{1,meas},\ \ldots,\ \varphi_{n,meas}$ are available, a corresponding $\boldsymbol{M}$ distribution can be determined by minimising a cost function of the form

$$C = \sum_i \left(\varphi_{i,meas} - \varphi(\boldsymbol{M})_{i,calc}\right) + \lambda_1(\nabla\odot\boldsymbol{M}\cdot\nabla\odot\boldsymbol{M}) + \lambda_2\ \mathrm{var}(|\boldsymbol{M}|). \tag{5.2}$$

Where C is the cost, λ are the regulariser weights, $\nabla\odot$ is the element-wise gradient operator and 'var' is the variance operator. Since $\boldsymbol{M}$ is represented by many discrete variables, regularising terms are used to ensure numerical stability as C converges to its minimum value. The minimisation converges to a solution more rapidly if the regularising terms also decrease as the solution is approached. For example, a low $\boldsymbol{M}$ gradient is favoured in ferromagnetic materials, and a small $|\boldsymbol{M}|$ variance is optimal in samples containing similar materials. The cost function is minimised by using a preconditioned CG method [198] to find the optimal $\boldsymbol{M}$. In the phase object approximation, the forward model for phase image calculation can be written in the form [190]

$$\varphi(x,y)_{i,calc} = -\frac{\mu_0}{2\Phi_0}\iint \frac{(y-y')\ M_x(x,y) - (x-x')\ M_y(x,y)}{(x-x')^2+(y-y')^2}\mathrm{d}x'\mathrm{d}y'. \tag{5.3}$$

Where Φ_0 is a magnetic flux quantum and M_x & M_y are the x and y components of the $\boldsymbol{M}$ projection in plane i, respectively. The use of a geometrical model to describe the sample defines the bounds of the integral, thus limiting the number of magnetisation voxels required for the calculation. Furthermore, the numerical convolution algorithm for Equation 5.3 can be optimised by implementing it in reciprocal space. Instead of evaluating the integral for each projected magnetisation pixel, the pixels can be assumed to be magnetised disks, for which the phase shift can be expressed analytically. All of the phase image pixels can then be calculated simultaneously by convolving the phase

contribution from a magnetised disk with all the positions of the magnetic moments. This approach improves the scaling of the execution time from being proportional to N^4 to $N^2 \log(N)$, where N is the number of magnetisation voxels. Overall, $\boldsymbol{M}$ reconstruction is a large-scale least-squares fitting problem, which uses iterative algorithms to fit an equation that projects and convolves a 3D distribution of magnetic moments to calculate phase shifts in multiple projections. This calculation is non-trivial, therefore care must be taken when interpreting results, and systematic sources of error are investigated by performing simulations.

5.3. Reconstruction of simulated uniformly-magnetised NWs

Simulations have previously been used to assess how the tilt range, tilt increment, and initial orientation of the sample can affect the accuracy of 3D $\boldsymbol{M}$ reconstruction [178]. It was found that a magnetic vortex state can be reconstructed with an average error below 1%, regardless of the orientation of the sample, by acquiring two orthogonal tilt series each spanning $\pm 60°$. For comparison, the sample described in Chapter 4 contains both a magnetic vortex state and uniformly-magnetised regions. In this instance, imaging was performed over two tilt series with 10° tilt increments and tilt ranges of $-60°$ to 30° and $-60°$ to 0° around the x- and y-axes, respectively.

To assess reconstruction errors in uniformly magnetised regions of the sample, 400 nm-long, 50 nm × 50 nm square-section NWs were simulated with select magnetisation orientations and voxel size of 2.5 nm. In the simulations presented below, a 0° tilt orientation corresponds to the electron beam travelling along the z-axis, as shown in Figure 5.1, and $\mu_0|\boldsymbol{M_{sim}}| = 1\text{T}$ without loss of generality. The simulated NW is considered the ground truth $\boldsymbol{M_{sim}}$, from which phase images are calculated using the MBIR forward model. In order to reveal computational errors, the output phase images are then used to reconstruct a $\boldsymbol{M}$ distribution that is subtracted from the ground truth. The errors are displayed as $\frac{\boldsymbol{M_{sim}}-\boldsymbol{M}}{|\boldsymbol{M_{sim}}|} \cdot 100\%$. It is initially assumed that the 3D geometric model of the sample is known, but the effects of an imperfect geometry reconstruction will be discussed in Section 5.4.

Figure 5.1a presents a simulation of a NW magnetised along the x-axis, where a phase measurement acquired at 0° tilt angle yields the phase contour map shown in Figure 5.1b.

Using the same tilt increments and ranges for the experiment described in Chapter 4, Figure 5.1c shows that the distribution of $\boldsymbol{M}$ determined by MBIR produces an error below 3% in the majority of the NW's volume, except for a small number of voxels at the corners. The average error in the magnitude of $\boldsymbol{M}$ from the NW cross-section is below 1%, as shown in Figure 5.1d. If the direction of $\boldsymbol{M}$ is oriented along the y-axis (Figure 5.2a), then a smaller total phase shift is detected, as evident in Figure 5.2b. Figure 5.2c shows that the errors in the magnitude of $\boldsymbol{M}$ determined using MBIR are again largest at the sample corners, whilst Figure 5.2d reveals that the average error in the cross-section is also below 1%. When the direction of $\boldsymbol{M}$ is oriented along the z-axis, as shown in Figure 5.3a, no magnetic phase shift is detected at 0° (Figure 5.3b). Figure 5.3c again confirms that the largest errors are located at the sample corners, whilst Figure 5.3d demonstrates that the average error in the cross-section is also below 1%.

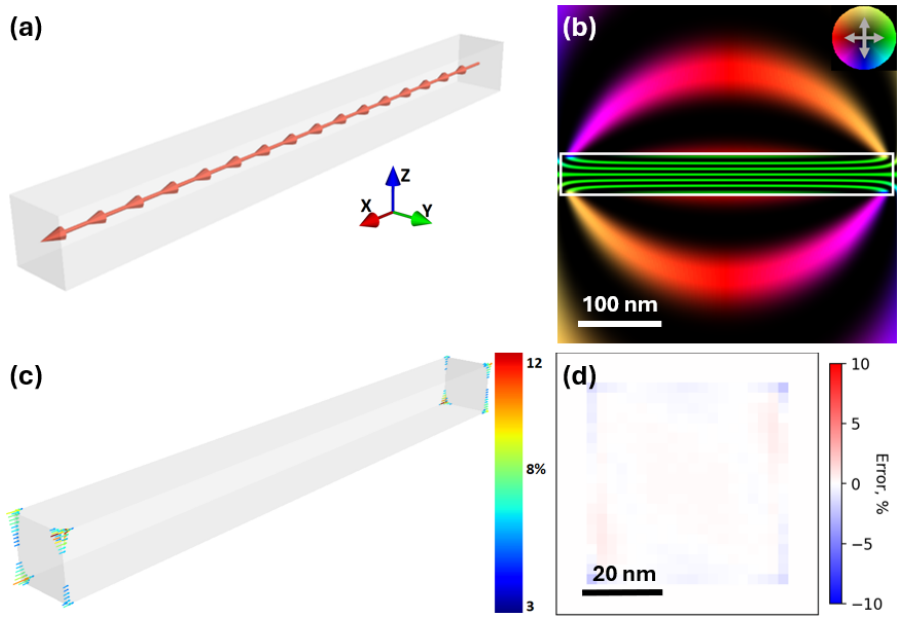

Figure 5.1. Reconstruction of a simulated NW magnetised along the x-axis. (a) Model showing the sample geometry and the $\boldsymbol{M}$ direction. (b) Phase contour map at 0° tilt, coloured to show the direction of the projected in-plane $\boldsymbol{B}$ field (inset), displayed as $\cos(12\varphi_m)$. The sample outline is marked in white. (c) $\boldsymbol{M}$ vectors reconstructed with error greater than 3%. (d) Average $\boldsymbol{M}$ magnitude error in the cross-section. The greatest errors are at the corners of the NW, where the separation of $\boldsymbol{M}$ and $\boldsymbol{H}$ is most ambiguous. Reproduced with permission from [1].

When using the same tilt range as in Chapter 4, these three simulations demonstrate that the average error in the magnitude of the reconstructed $\boldsymbol{M}$ is less than 1% for uniformly magnetised NWs. Reconstruction errors close to the NW surface are attributed

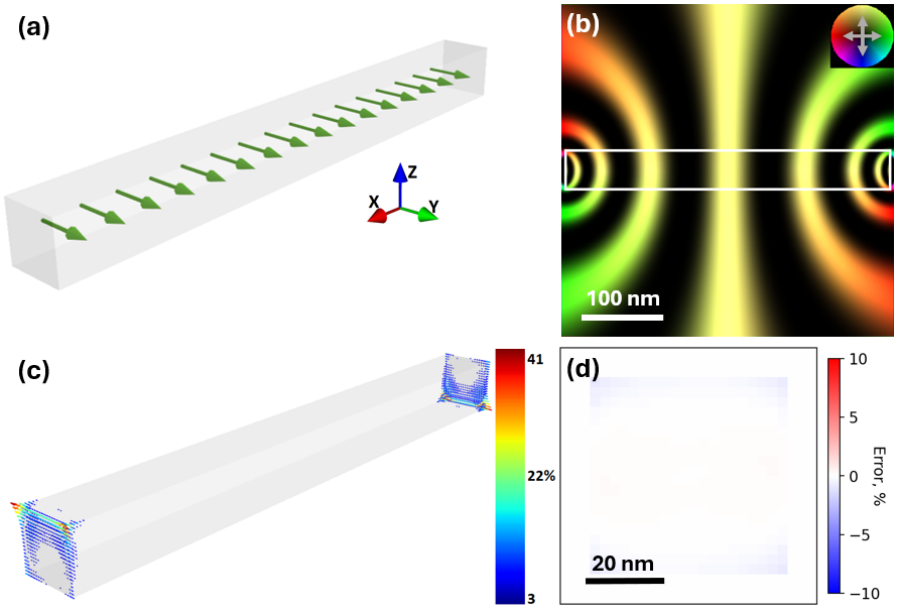

Figure 5.2. Reconstruction of a simulated NW magnetised along the y-axis. (a) Model showing sample geometry and $\boldsymbol{M}$ direction. (b) Phase map at 0° tilt, displayed as $\cos(12\varphi_m)$ and coloured to show the direction of in-plane $\boldsymbol{B}$. The sample outline is marked in white. (c) $\boldsymbol{M}$ reconstruction error. (d) Average $\boldsymbol{M}$ magnitude error in the cross-section. Reproduced with permission from [1].

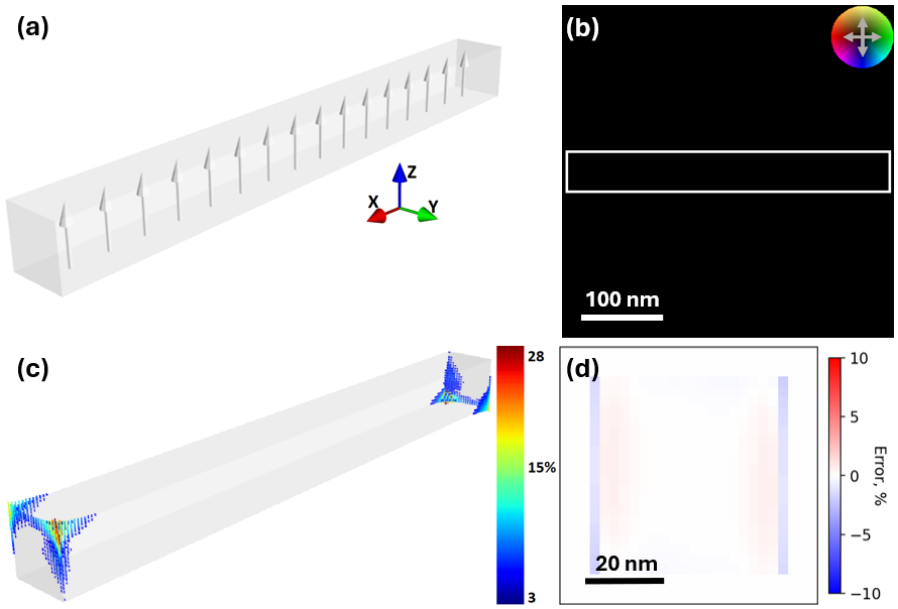

Figure 5.3. Reconstruction of a simulated NW magnetised along the z-axis. (a) Model showing sample geometry and $\boldsymbol{M}$ direction. (b) Phase map at 0° tilt, displayed as $\cos(12\varphi_m)$ and coloured to show the direction of in-plane $\boldsymbol{B}$. The sample outline is marked in white. (c) $\boldsymbol{M}$ reconstruction error. (d) Average $\boldsymbol{M}$ magnitude error in the cross-section. Reproduced with permission from [1].

to the effects of digitisation (i.e., finite pixel size), and the limited and asymmetrical tilt range, which affects spatial resolution at the interface between vacuum and sample [178]. Additionally, the reconstruction is less accurate at the sample corners, where the $\boldsymbol{H}$ field is strong, as seen in Figure 5.2b, and discontinuous (Equation 4.1). This is attributed to the localised mixing of $\boldsymbol{H}$ and $\boldsymbol{M}$ signals, centred at locations of discontinuous $\boldsymbol{H}$, and extending over a distance shorter than the spatial resolution (8 nm). The mixing of signals is notably increased if there is insufficient projection data to fully constrain the reconstruction. In summary, MBIR acts to find a distribution of $\boldsymbol{M}$ that minimises the error between the simulated and input phase images, but the solutions are indeterminate when using limited tilt ranges. In the simulations presented, the least constrained voxels located at the corners exhibit the largest errors.

5.4. Uncertainty due to the missing wedge in tomographic datasets

The geometrical model defines the spatial location of the magnetic sample and hence affects the reconstruction. If the geometrical model of the square-cross-section NW in Figure 5.4a was generated from experimental electron holograms with an inaccurate missing wedge correction, it would typically be larger than the fabricated NW. The edges of the NW appeared to be diffuse in the experimental images, due to uneven surface texture and variations in material composition. This blurring often results in a $\sim$5 nm uncertainty in determining the position of the NW surface and limits the precision of any missing-wedge correction, as discussed in Chapter 4. For this reason, a 5 nm error was introduced during the missing wedge correction in the following simulation (Figure 5.4) using the ground-truth model defined in Section 5.3. Figure 5.4b shows a cross-section of a partially-corrected model generated for the same orientations as Section 5.3. Since the model incorrectly treats select regions of vacuum as magnetic material, the reconstructed distribution of $\boldsymbol{M}$ exhibits errors near the NW surfaces due to spatial averaging. Figure 5.4c reveals that while the peak of the distribution matches the correct value for the NW, spatial averaging at the vacuum/NW interface spreads the range of $|\boldsymbol{M}|$ values. Figure 5.4d displays the average error in the cross-section, which is influenced by an overestimation of the vacuum values and a reduction of the values in the nearby material. The reconstructed distribution has a mean value of $\mu_0|\boldsymbol{M}| = 0.92$ T and a standard deviation of 0.14 T. Overall, the results show that if surface errors are

present, the reconstruction of a uniform magnetic domain produces a distribution of $|\boldsymbol{M}|$ values, albeit one in which the peak is close to the true value.

Taken together, the simulations show that a uniformly-magnetised NW can be reconstructed with an average error below 1% for the imaging orientations used in the sections above. However, errors in the geometrical model of the NW can cause the vacuum and material $\boldsymbol{M}$ values to combine near the surface. The extent of spatial averaging is specified by the spatial resolution (8 nm), which is determined using methods discussed in Section 4.2.5. Quantitative measurements are shown to be statistically significant when the average value of $\boldsymbol{M}$ is calculated from a volume larger than the spatial resolution.

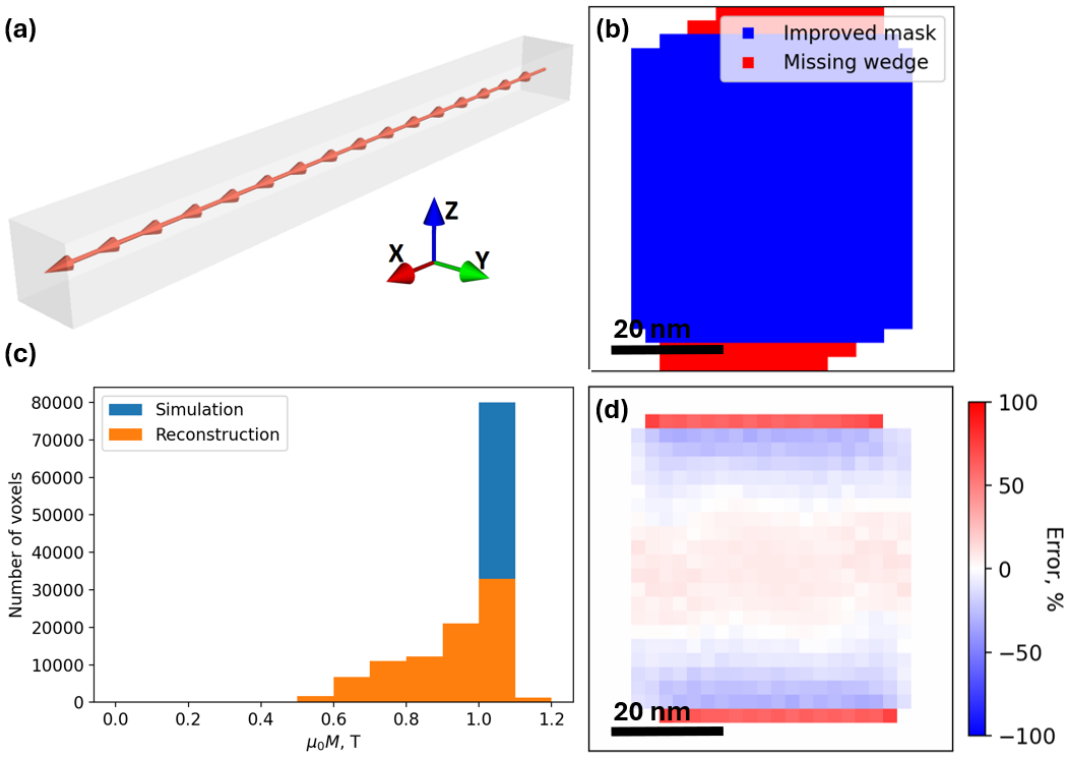

Figure 5.4. Reconstruction of a simulated NW with incomplete missing wedge correction. (a) Model showing sample geometry and $\boldsymbol{M}$ direction. (b) Reconstructed geometrical model, showing the effect of the missing wedge in a cross-section. (c) Reconstructed $\boldsymbol{M}$ magnitude distribution if the missing wedge is not corrected fully. (d) Average $\boldsymbol{M}$ magnitude error in a cross-section, showing false values assigned to vacuum and a reduced signal in voxels close to the false region. The surface voxels are incorrect if there are errors when generating the geometrical model. Reproduced with permission from [1].

5.5. Reconstruction of simulated null spaces

Some distributions of $\boldsymbol{M}$, like Bloch points [199], are invisible to LTEM, and therefore act as an excellent test example for extreme cases of 3D $\boldsymbol{M}$ reconstruction. As shown by Equation 4.2, LTEM is fundamentally sensitive to the $\boldsymbol{B}$ field, which is the sum of $\boldsymbol{M}$ and $\boldsymbol{H}$, as per Equation 4.1. Non-zero distributions of $\boldsymbol{M}$ can exist where the associated $\boldsymbol{B} = 0$. Such distributions often correspond to volumes of material where $\boldsymbol{M}$ is divergent ($\nabla \cdot \boldsymbol{M} \neq 0$), and are accepted to be invisible to LTEM imaging techniques [181]. Consequently, the MBIR algorithm is coded to reconstruct visible signals only, assigning a value of $\boldsymbol{M} \approx 0$ to any volume that does not produce a phase shift.

The inability to experimentally distinguish between $\nabla \cdot \boldsymbol{M} \neq 0$ and $\boldsymbol{M} = 0$ indicates that some $\boldsymbol{M}$ information is lost during LTEM measurements. In simulations, physical processes that cause information loss correspond to non-invertible mathematical operations in the MBIR forward model. Information can be lost in two stages during phase image simulations of a given $\boldsymbol{M}$: first, when projecting $\boldsymbol{M}$, and second, when convolving the projected distribution of $\boldsymbol{M}$ with a kernel to obtain the corresponding φ_m [181, 182]. As described in [182], information loss from projection can be avoided by using two complete tilt series. However, information loss during phase calculation is unavoidable, as certain distributions of $\boldsymbol{M}$ correspond to eigenstates of a null space and can be added to any reconstruction without changing the corresponding phase images. As null space eigenstates cannot be recovered using the current implementation of MBIR, null spaces can show $\boldsymbol{M} \approx 0$ after reconstruction. In practice, null space eigenstates are only known to exist in some ferromagnetic nanostructures, such as fully divergent configurations [182] and Néel-type magnetic DWs [58]. Here, several such configurations are simulated and compared to a simulation of an L-shaped NW structure.

5.5.1. Information loss due to projection

The effect of projection-based information loss is illustrated in Figure 5.5, which shows simulated magnetic phase images of vortex-type magnetic DWs located in the NW centres. The NWs have a diameter of 100 nm, an aspect ratio of 10:1 and $\mu_0 |\boldsymbol{M}| = 1$ T. The phase images shown in Figures 5.5b3 and c3 are indistinguishable when phase measurement noise exceeds 0.1 %, despite corresponding to different configurations of $\boldsymbol{M}$. To facilitate a successful reconstruction, the sample must be tilted, as shown in Figure 5.5a. In the null space simulations below, complete tilt series (360° tilt range) are

simulated to prevent information loss from projection; this ensures that any loss during reconstruction is attributed solely to the phase calculation.

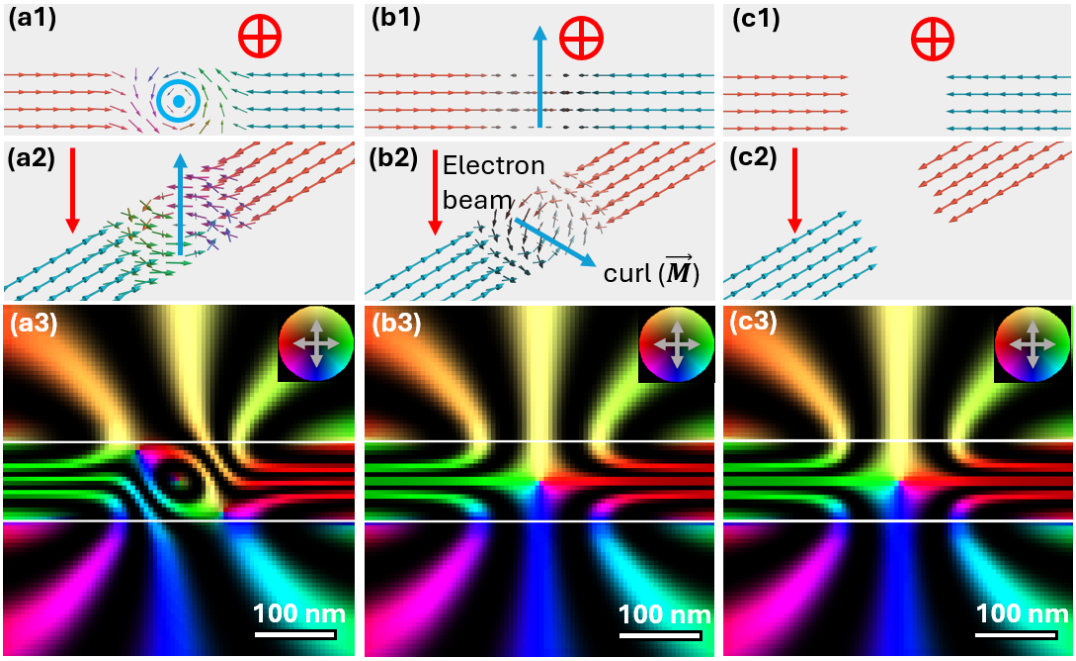

Figure 5.5. Simulated magnetic phase images of non-unique signals in vector field projections. (a1), (b1), (c1) Projections of $\boldsymbol{M}$ in the electron beam direction. (a2), (b2), (c2) Isometric projections of $\boldsymbol{M}$. The red arrows show the direction of the electron beam. The blue arrows show the direction of curl($\boldsymbol{M}$) at the core of a vortex-type magnetic DW. (a3), (b3), (c3) Corresponding magnetic phase contour images, displayed as $\cos(5\varphi_{mag})$, coloured to show the direction of the projected in-plane $\boldsymbol{B}$ field (inset). The magnetic vortex states only affect the electron phase if curl($\boldsymbol{M}$) has a component parallel to the electron beam direction. Therefore, in (a) the magnetic vortex is imaged perfectly, but in (b) the magnetic DW introduces no phase shift and is indistinguishable from the non-magnetic material represented in (c). Reproduced with permission from [1].

5.5.2. Information loss due to divergent magnetisation

While an infinitely-long, first-order Halbach cylinder produces no magnetic signal in TEM in any projection direction [182,200], a Halbach cylinder of finite length does. Figure 5.6a shows a simulation of a 40-nm-long, 40-nm-diameter cylinder with $\mu_0 \left|\boldsymbol{M}_{\boldsymbol{sim}}\right| = 1$ T, in which $\boldsymbol{M}_{\boldsymbol{sim}}$ is oriented radially outward and has non-zero divergence at all points (Figure 5.6b). Phase images were simulated for two orthogonal 360° tilt arcs with 10° increments, including projections parallel (Figure 5.6c) and perpendicular (Figure 5.6d)

to the central axis of the cylinder. Although no magnetic phase shift is expected in Figure 5.6c, a small residual signal close to the surface of the cylinder is present due to digitisation effects (i.e., finite pixel size). In Figure 5.6d, no signal would be detected when the cylinder is infinitely long. However, because the cylinder has a finite length, a detectable phase shift is present. The simulated phase images were used to reconstruct $\boldsymbol{M}$, which is compared to the ground truth of the simulation input. Figures 5.7a and 5.7b show the reconstructed distributions of $\boldsymbol{M}$ in cross-section at the surface of the cylinder. The magnitude of $\boldsymbol{M}$ is up to twice that of the input, likely because discontinuities in $\boldsymbol{H}$ creates more significant artefacts in regions with little-to-no signal from $\boldsymbol{M}$. Figures 5.7c and 5.7d show the reconstructed cross-section of the null space in the middle of the cylinder, where the magnitude of $\boldsymbol{M}$ is 90% lower than the input. $\boldsymbol{M}$ is also rotated towards the direction of $\boldsymbol{H}$. The simulation shows that such configurations, in which $\boldsymbol{M}$ is divergent at all points, cannot be reconstructed successfully without the use of additional constraints.

Similar null spaces have been observed when imaging Néel-type magnetic DWs in thin films that exhibit the interfacial Dzyaloshinskii–Moriya interaction [58, 183, 201]. In order to evaluate possible reconstruction errors, a 100 nm x 100 nm x 50 nm film containing a Néel-type magnetic DW was simulated, as shown in Figures 5.8a and 5.8b. Phase images were simulated for two orthogonal 360° tilt arcs with 10° increments. A magnetic phase shift from the uniformly-magnetised parts of the film is detected in all of the projections, as shown in Figures 5.8c and 5.8d. The reconstruction shows $< 1\%$ average error in the uniformly-magnetised parts of the film. However, some signal is missing in the magnetic DW itself. Figures 5.9a and 5.9b show that the reconstruction has a 15% error at the surface of the magnetic DW. $\boldsymbol{M}$ is also not separated fully from $\boldsymbol{H}$ at the corners of the film. Figures 5.9c and 5.9d show the null space inside the film, where up to 75% of the signal is lost in the core of the DW. This loss of signal depends on the magnetic DW width. The simulations show that, in thin films, only uniform regions around Néel-type magnetic DWs can be reconstructed quantitatively, without the use of additional constraints. In addition, qualitative measurement of the magnetic DW orientation would require a $\pm 60°$ tilt range, in accordance with previous simulations [178].

Néel-type magnetic DWs may also be present in NW structures. The magnetic DW width in cobalt NWs has been observed to be ~ 100 nm [31] and the rotation of $\boldsymbol{M}$ in the DW may be smaller than 180°. A Néel-type magnetic DW was simulated in an L-shaped, 600-nm-long, 100-nm-wide, square-cross-section NW, as shown in Figures 5.10a and

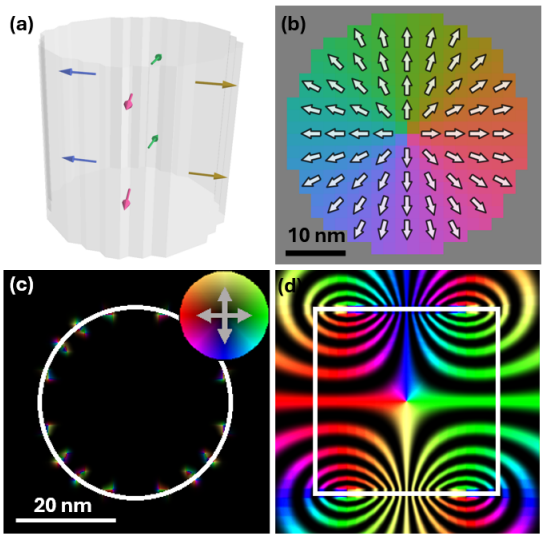

Figure 5.6. Simulated magnetic phase images of a divergent Halbach cylinder. (a) Model showing the sample geometry and the $\boldsymbol{M}$ direction. (b) $\boldsymbol{M}$ distribution in a cross-section of the sample. (c) Phase map simulated with an electron beam parallel to the central axis of the cylinder. (d) Phase map simulated with an electron beam perpendicular to the central axis of the cylinder. The phase maps are coloured to show the direction of the projected in-plane $\boldsymbol{M}$ field (inset), displayed as $\cos(200\varphi_{mag})$. The sample outline is marked in white. Reproduced with permission from [1].

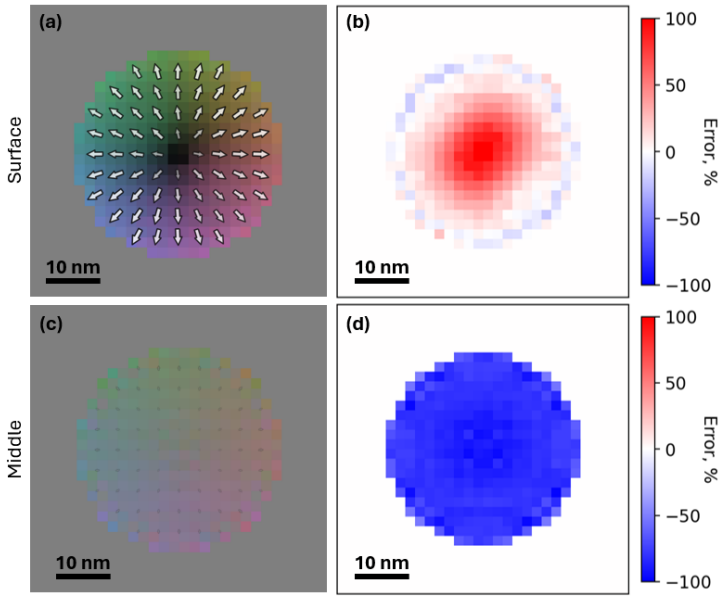

Figure 5.7. Reconstruction of a simulated divergent Halbach cylinder. (a) Reconstructed $\boldsymbol{M}$ cross-section at the surface. (b) $\boldsymbol{M}$ magnitude error at the surface, showing an overestimate of up to 110%. (c) Reconstructed $\boldsymbol{M}$ cross-section in the middle of the cylinder. (d) $\boldsymbol{M}$ magnitude error in the middle, showing a 90% loss of signal. Reproduced with permission from [1].

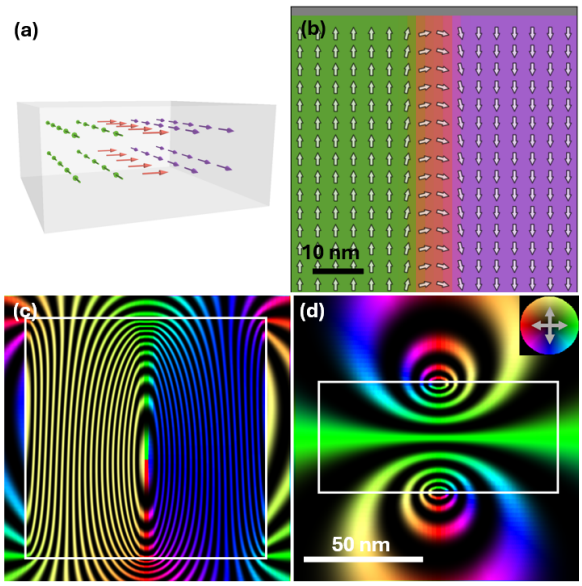

Figure 5.8. Simulated magnetic phase images of a Néel-type magnetic DW. (a) Model showing the sample geometry and $\boldsymbol{M}$ direction (viewed from the side). (b) $\boldsymbol{M}$ distribution in a slice of the sample close to the edge (viewed from the top). (c) Top-down phase contour map. (d) Sideways phase contour map. The magnetic phase contour images are coloured to show the direction of the projected in-plane $\boldsymbol{M}$ field (inset), displayed as $\cos(40\varphi_{mag})$. Reproduced with permission from [1].

5.10b. Phase images were simulated for two orthogonal 360° tilt arcs with 10° increments, including the projections shown in Figures 5.10c and 5.10d. The reconstruction in Figure 5.11 shows that the full volume of the reconstruction acquires an average error of $\sim 1\%$. As displayed in Figure 5.11d, as signal loss in the middle of the magnetic NW is up to 5%, suggesting that null space effects in such NWs can be less than signal loss in thin film Néel-type DWs.

5.6. Conclusions

As described in Chapter 4, simulations have previously been used to show that magnetic vortex states do not result in null spaces if they are imaged close to the direction of the curl of the magnetic vortex [178]. In the absence of a significant null space contribution, any errors associated with the separation of $\boldsymbol{M}$ and $\boldsymbol{H}$ are expected to be less than the $\sim 2\%$ reconstruction random error observed in Section 4.2.5.

Overall, simulations were used to identify two major types of systematic artefacts and two corresponding methods for identifying their contributions. First, it was observed that the reconstructed $\boldsymbol{M}$ signal can mix with vacuum and $\boldsymbol{H}$ signals, but this spatial (and signal) averaging is limited to volumes smaller than the spatial resolution of the reconstruction. Therefore, quantitative measurements should be performed by considering the average $\boldsymbol{M}$ in a magnetic domain no smaller than the spatial resolution in all dimensions. Secondly, it was identified that divergent $\boldsymbol{M}$ is not detected by LTEM techniques, and therefore, is reconstructed as an absence of signal corresponding to $\boldsymbol{M} \approx 0$. In summary, MBIR can only reconstruct $\boldsymbol{M}$ distributions that create a detectable phase shift signal, and only features larger than the 3D spatial resolution limit can be interpreted quantitatively.

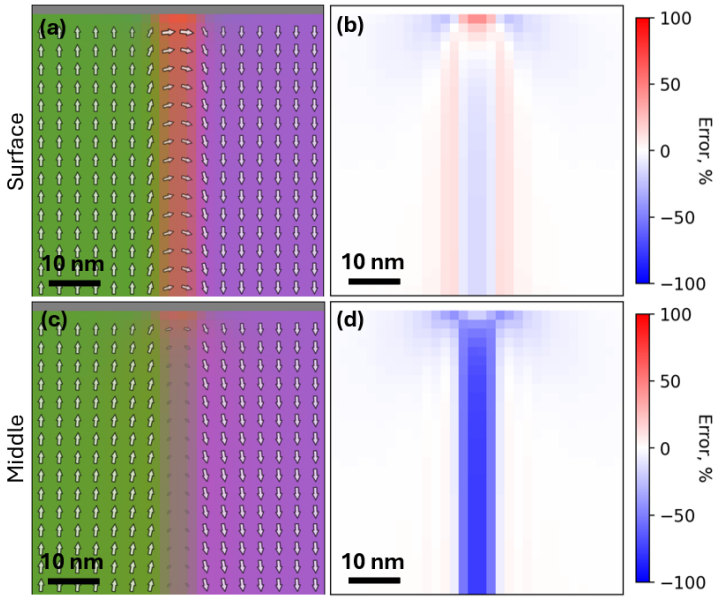

Figure 5.9. Reconstruction of a simulated Néel-type magnetic DW. (a) Reconstructed $\boldsymbol{M}$ slice at the surface. (b) $\boldsymbol{M}$ magnitude error at the top surface (c) Reconstructed $\boldsymbol{M}$ slice in the middle of the film. (d) $\boldsymbol{M}$ magnitude error in the middle of the film. There is a null space in the core of the Néel-type magnetic DW. Reproduced with permission from [1].

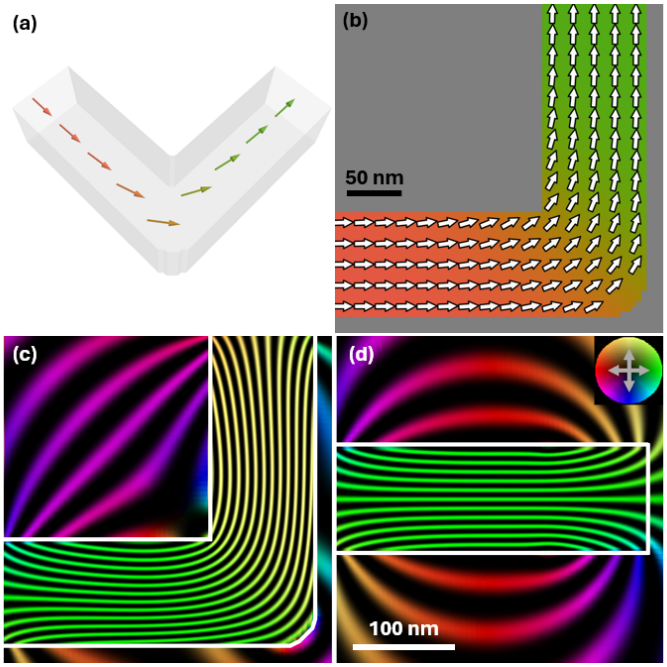

Figure 5.10. Simulated magnetic phase images of a NW with a Néel-type magnetic DW. (a) Sample geometry. (b) $\boldsymbol{M}$ distribution in a slice of the sample. (c) Top-down phase map. (d) Phase map from the side. The phase maps are coloured to show the direction of the projected $\boldsymbol{B}$ (inset), displayed as $\cos(6\varphi_{mag})$. Reproduced with permission from [1].

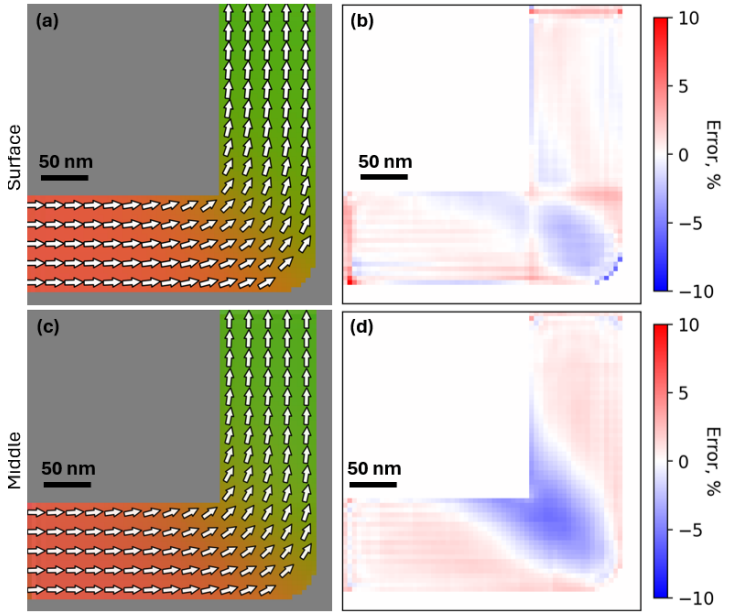

Figure 5.11. Reconstruction of a simulated NW with a Néel-type magnetic DW. (a),(c) Reconstructed $\boldsymbol{M}$ slices, respectively, at the surface and in the middle. (b),(d) $\boldsymbol{M}$ magnitude error, respectively, at the surface and in the middle. There is $< 5\%$ signal loss in the core of the DW. Reproduced with permission from [1].

Chapter 6.

Summary and Outlook

The main theme of this work is the development of methods that extend the fabrication and characterisation of ferromagnetic nanostructures from 2D to 3D. Chapter 1 summarises the recent history of spintronics development. Specifically, how planar ferromagnetic nanostructures have been applied to develop non-volatile high-density data storage technologies [8, 9], and how spin transfer torque has been used to translate magnetic DWs to perform stochastic computations [11] or store data in a magnetic RM-based shift-register [10]. Investigations of 3D nanomagnetism have found that if the planar nanocircuits underpinning these technologies are fabricated on curved surfaces or as free-standing 3D structures, the micromagnetic interactions that affect spintronics applications can be tuned by adjusting the geometry of the 3D nanostructure [14, 15]. The development of fabrication and characterisation methods that can extend to the third spatial dimension is a necessary part of 3D nanomagnetism research. This novel area of research is increasingly significant because, in this decade, the quantum-mechanical limit has been reached for the size of transistors in conventional computer chips [3, 5]. Hence, novel technologies with applications in nanoscale computer hardware, like 3D spintronics, are being developed.

Accurate theoretical descriptions and the computational tools to apply them are key to the development of 3D nanomagnetism. The description of atoms as individual magnets coupled by interatomic interactions between their magnetic moments, and the generalisation of this to the $\boldsymbol{M}$ field, is a successful theory for describing properties of ferromagnetic nanostructures [17, 23]. Applying theories defined on the atomic scale to nanoscale samples requires the use of computational methods, which frequently rely on cost minimisation algorithms. Since standard techniques, like least-squares fitting and determining minimum energy states in micromagnetic simulations, are implemented

by finding function parameters that minimise a scalar value, the principles of industry-standard CG algorithms are presented [191, 202].

Chapter 2 introduces conventional electron microscopy nano-characterisation techniques, which detect interactions between the electron beam and the sample with spatial resolution down to a few pm. As the first step in all experiments, an SEM is used to scan large areas of the sample surface and characterise the topography [74]. Additionally, the space around the sample is used to mount additional instruments and allows a large range of movement, such as using a sample stage that can tilt up to 55° for tomographic imaging. For sample preparation, an ion beam is used to mill material, and a GIS allows the use of FEBID for the fabrication of Co and Fe nanostructures [120]. A STEM is used to analyse electron scattering, either by using an ADF detector to image materials or using a spectrometer to map elemental distributions. By modelling the inelastic scattering, the number of atoms of each chemical element in a material can be determined [92]. To complement these characterisations, the LTEM method of off-axis electron holography is applied to reconstruct the electron phase shift, which is sensitive to the $\boldsymbol{B}$ field. In combination, these techniques are used for large-scale mapping of sample geometry, both additive & subtractive manufacturing, quantitative measurement of elemental composition, and reconstruction of magnetic fields. Even though this is a small subset of the capabilities of each instrument, it is sufficient to comprehensively characterise ferromagnetic nanostructures and correlate measurements to uncover underlying physical phenomena.

Chapter 3 presents optimisations to the FEBID method used to fabricate 3D ferromagnetic nanostructures. It is found that FEBID NWs fabricated at an angle relative to the beam-axis by translating the beam exhibit a different material composition than vertical NWs. For NWs grown at angles from 0° to 90° relative to the beam-axis, the decrease in metal content in the NW core was measured to be up to 0.4% per degree of growth angle, but was improved to 0.1%/° by optimising the deposition parameters. This was achieved by tuning the SEM beam accelerating voltage to limit beam transmission through the sample, such that the interaction volume would be no larger than the NW diameter. This optimisation also improved the uniformity in NW cross-section shape and $\boldsymbol{B}$ fields created by Co and Fe NWs angled up to 60°. As a nanoscale additive manufacturing technique, FEBID is uniquely suited for prototyping of 3D ferromagnetic nano circuits, and the performance consistency of such spintronic prototypes is improved by ensuring uniformity in the deposited material.

Chapter 4 demonstrates that the 3D $\boldsymbol{M}$ field can be reconstructed using LTEM techniques [1]. The $\boldsymbol{M}$ inside a free-standing L-shaped FEBID Co NW sample is reconstructed and compared to expected values based on previous X-ray tomography experiments [31] and characterisation of elemental composition [42]. By using sample-edge matching to correct image distortions, common-lines-based alignment of tomographic projections, and an MBIR algorithm, the $\boldsymbol{M}$ is reconstructed with a 50 nm spatial resolution in 3D. The measurement precision for uniform magnetic domains larger than 50 nm is $1e^4$ A/m. The main limitations in spatial resolution were computational and may be solved by optimising the software to use a smaller voxel size and more advanced tomographic alignment algorithms. Since the resolution is systematically limited to 3x the pixel size, given a suitable LTEM tomographic dataset, atomic resolution 3D $\boldsymbol{M}$ reconstruction is possible using MBIR. This work shows that the MBIR algorithms that underlie the development of powerful X-ray tomography techniques [169, 203] can be applied with electron microscopy to characterise vector fields in 3D. EH-VFT can be applied, as described, to reconstruct 3D $\boldsymbol{M}$ in nanoparticles, spintronic NW circuits, and prototypes of 3D data storage devices [13]. Furthermore, the MBIR framework can be extended to simultaneously reconstruct all signals present in electron holograms, such that a single tomographic dataset could be used to characterise the locations of scattering defects, the charge distribution, $\boldsymbol{M}$, and all electromagnetic fields & potentials obtained by applying Maxwell's equations to the reconstructed distributions. With continued development, tomographic LTEM can become a technique for comprehensive, multi-signal 3D nanoscale characterisation.

Chapter 5 discusses simulations used to evaluate systematic sources of error and computational artefacts in EH-VFT reconstructions. Simulations confirm that the spatial averaging observed in Section 4.2.5 results from the use of the MBIR regularising term that ensures reconstruction convergence to ferromagnetic $\boldsymbol{M}$ distributions. The spatial averaging is observed as a "blurring" of neighbouring $\boldsymbol{M}$ vector components and a mixing of $\boldsymbol{M}$ & $\boldsymbol{H}$ signals, but the errors are localised in volumes smaller than the systematic spatial resolution limit (3x voxel size) and the average simulated reconstruction error is $< 1\%$, when compared to the ground truth. Additionally, divergent $\boldsymbol{M}$ distributions that are invisible to LTEM techniques [181] are simulated. It is observed that MBIR reconstructs only those 3D $\boldsymbol{M}$ distributions that produce a detectable phase-shift signal. Hence, errors are observed at points where $\boldsymbol{M}$ is divergent. Due to spatial averaging, the systematic reconstruction error is below 1% only for magnetic domains larger than the spatial resolution in all dimensions. This shows that MBIR implementation exhibits no unconventional computational artefacts, and the uncertainties

in EH-VFT 3D reconstructions can be described using conventional parameters, such as signal strength and spatial resolution.

In conclusion, methods for both the optimised fabrication of 3D ferromagnetic NW structures and characterisation of their 3D $\boldsymbol{M}$ configurations have been developed. By optimising FEBID such that the SEM beam acts like a point source of SEs, uniform cross-section geometries and material compositions are achieved in NWs angled from 0° to 60° relative to the beam axis. To characterise 3D $\boldsymbol{M}$ configurations in spintronic prototypes fabricated using FEBID, an EH-VFT reconstruction algorithm was developed that showed a 50 nm spatial resolution. Simulations do not show unexpected computational artefacts in the MBIR algorithm, thus atomic resolution 3D $\boldsymbol{M}$ reconstructions should be possible for high-resolution EH-VFT datasets. As the significance of novel 3D nanotechnologies grows, this work develops dedicated techniques for 3D prototyping of spintronic devices and for the characterisation of 3D electromagnetic fields up to atomic resolution.

Appendix A.

Software packages

The primary scientific software packages used in this work. Their repositories and relevant accompanying publications (if available) are listed here.

- MBIR-TEM. MBIR-based magnetisation reconstruction package guiding the workflow [1]. Repository: `https://github.com/AurysSilinga/MBIR-TEM`
- F3ast. FEBID modelling package used for sample fabrication with CAD [79]. Repository: `https://github.com/skoricius/f3ast`
- Gatan DigitalMicrograph with Holoview and HoloWorks plugins. Hologram-to-phase reconstruction [159, 160]. Repository: `http://www.dmscripting.com`
- Hyperspy. Interface between DigitalMicrograph and Python, with interactive image manipulation in Python [186]. Repository: `https://hyperspy.org/`
- Scikit-image. Canny edge detection and image manipulation for phase shift separation [185]. Repository: `https://scikit-image.org/`
- fpd. Image feature matching for phase shift separation and RANSAC-algorithm-based background removal for tomographic alignment [187]. Repository: `https://gitlab.com/fpdpy/fpd`
- Scipy. Error function minimisation for tomographic alignment [189]. Repository: `https://scipy.org/`
- Jutil. CG minimisation for MBIR. Repository: `https://jugit.fz-juelich.de/j.ungermann/jutil`

- Pyramid. MBIR simulations [172]. Repository: `https://iffgit.fz-juelich.de/empyre/empyre/-/tree/pyramid-master`
- Mumax. Micromagnetic simulations [23]. Repository: `https://mumax.github.io/`

Appendix B.

EELS maps

The following tables and figures uniquely identify each FEBID NW and display the underlying compositional maps related to the data in Chapter 3. To facilitate comparison, the figures are annotated. In SEM images, solid blue lines indicate areas where STEM EELS maps are acquired for analysis. Dashed black lines represent STEM EELS maps obtained for calibration, which are not shown here but are available in the data repository. In the maps of atomic composition, blue shading corresponds to the central band, where the mean value is taken to represent average projected Co (or Fe) content. Since this thesis and previous works [42] do not detect ferromagnetism in NWs with less than 40% Co content, red shading indicates the presumed non-magnetic outer shell of NWs. In summary, angled FEBID NWs are asymmetric and exhibit non-trivial spatial distributions of material composition. Therefore, it is shown detail how the data points in Chapter 3 were acquired.

B.1. Dataset $Co^{\uparrow}_{30\ kV}$

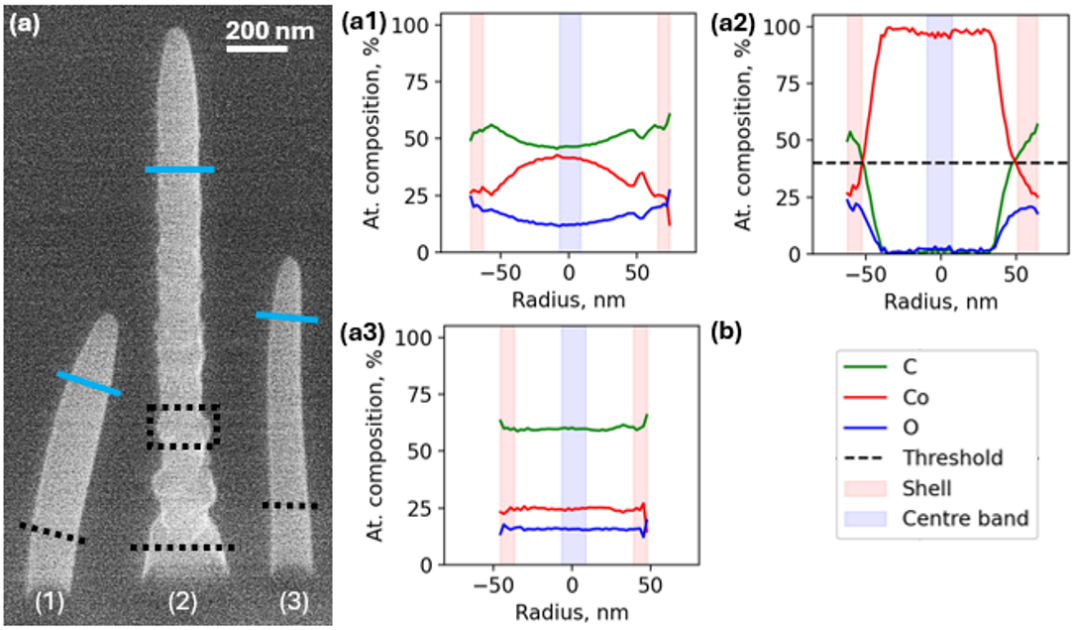

Figure B.1. Characterisation of sample $Co^{\uparrow}_{30\ kV}$. (a) SEM image labelling the NWs and showing areas mapped with STEM EELS. (a1-a3) Compositional maps of the corresponding NWs. (b) Legend.

Table B.1. $Co^{\uparrow}_{30\ kV}$.

NW position marker	(1)*	(2)	(3)*
SEM beam current, pA	690	2800	170

*Deposited with an out-of-focus beam.

B.2. Dataset $Co^{\uparrow}_{\text{anneal, 30 kV}}$

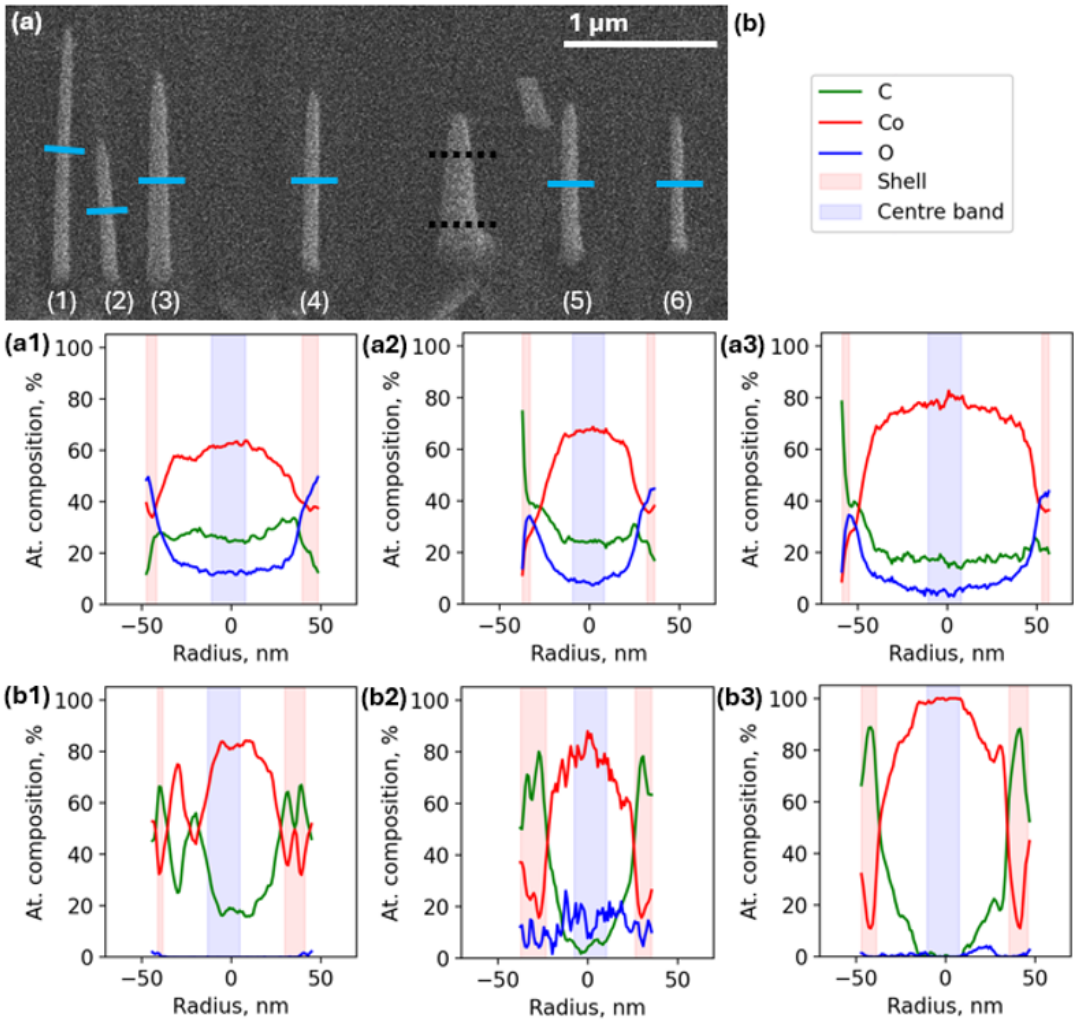

Figure B.2. Characterisation of sample $Co^{\uparrow}_{\text{anneal, 30 kV}}$. (a) SEM image labelling the NWs and showing areas mapped with STEM EELS. (a1-a3) Compositional maps of the corresponding NWs. (b1-b3) Compositional maps of the corresponding NWs after annealing for 30 min at 350 °C (b) Legend.

Table B.2. $Co^{\uparrow}_{\text{anneal, 30 kV}}$.

NW position marker	(1)	(2)	(3)	(4)	(5)	(6)
SEM accelerating voltage, kV	30	30	30	15	5	5
SEM beam current, pA	86	21	340	86	86	21

B.3. Dataset $Co^{\uparrow}_{5\ kV}$

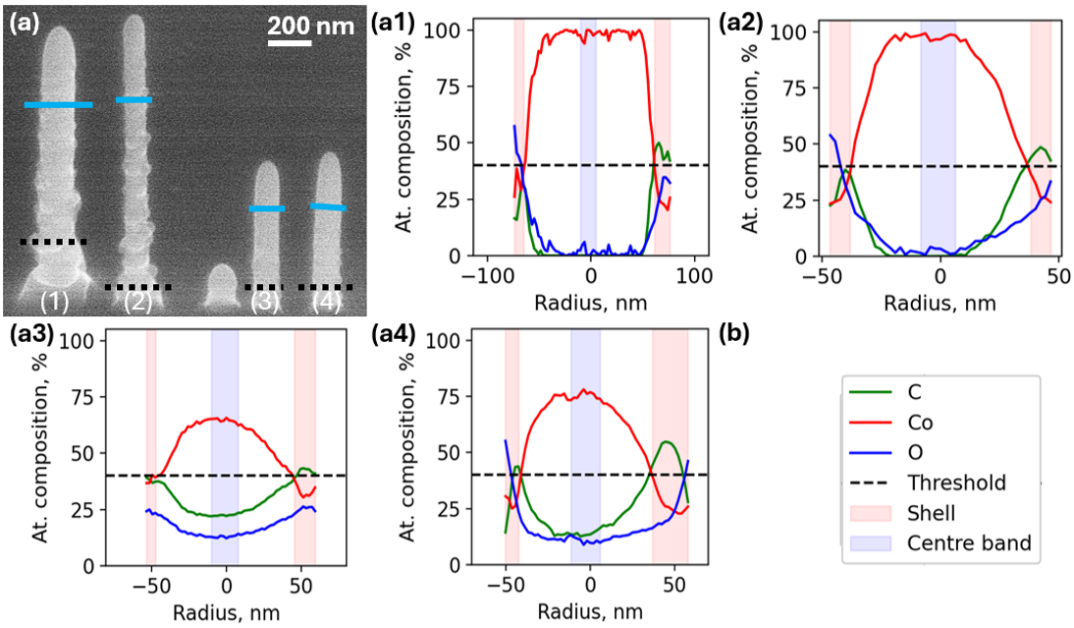

Figure B.3. Characterisation of sample $Co^{\uparrow}_{5\ kV}$. (a) SEM image labelling the NWs and showing areas mapped with STEM EELS. (a1-a4) Compositional maps of the corresponding NWs. (b) Legend.

Table B.3. $Co^{\uparrow}_{5\ kV}$.

NW position marker	(1)	(2)	(3)	(4)
SEM beam current, pA	2800	690	170	340

B.4. Datasets $Fe^{\uparrow}_{5\ kV}$ and $Fe^{\uparrow}_{30\ kV}$

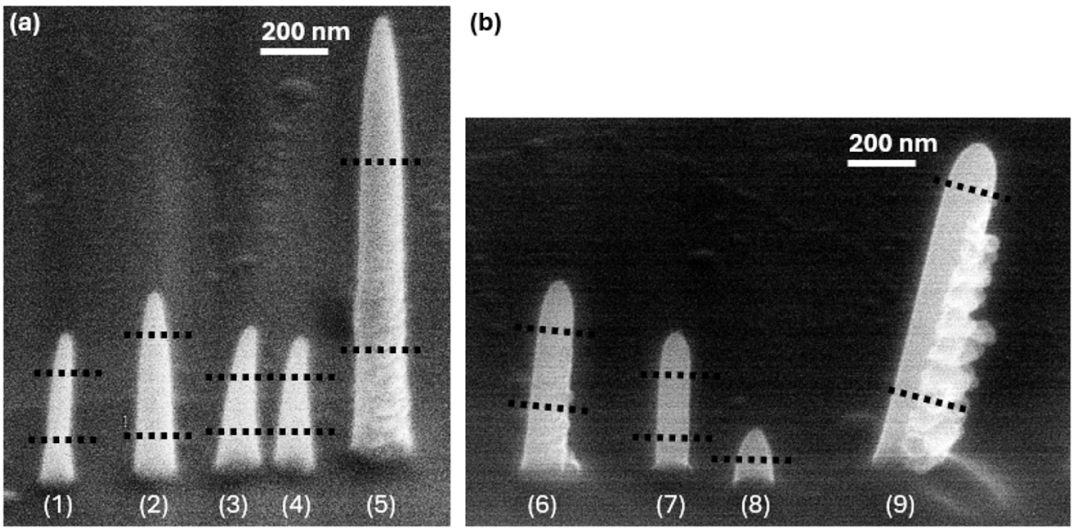

Figure B.4. Characterisation of samples $Fe^{\uparrow}_{30\ kV}$ and $Fe^{\uparrow}_{5\ kV}$. (a-b) SEM images labelling the NWs and showing areas mapped with STEM EELS. The dataset is only required to qualitatively observe autocatalytic growth and variations of NW diameter.

Table B.4. $Fe^{\uparrow}_{30\ kV}$ and $Fe^{\uparrow}_{5\ kV}$.

NW position marker	(1)	(2)	(3)	(4)	(5)	(6)	(7)	(8)	(9)
SEM accelerating voltage, kV	30	30	30	30	30	5	5	5	5
SEM beam current, pA	690	2800	170	170	11000	2800	690	170	11000

B.5. Dataset $Co^{\nearrow}_{30\ kV}$

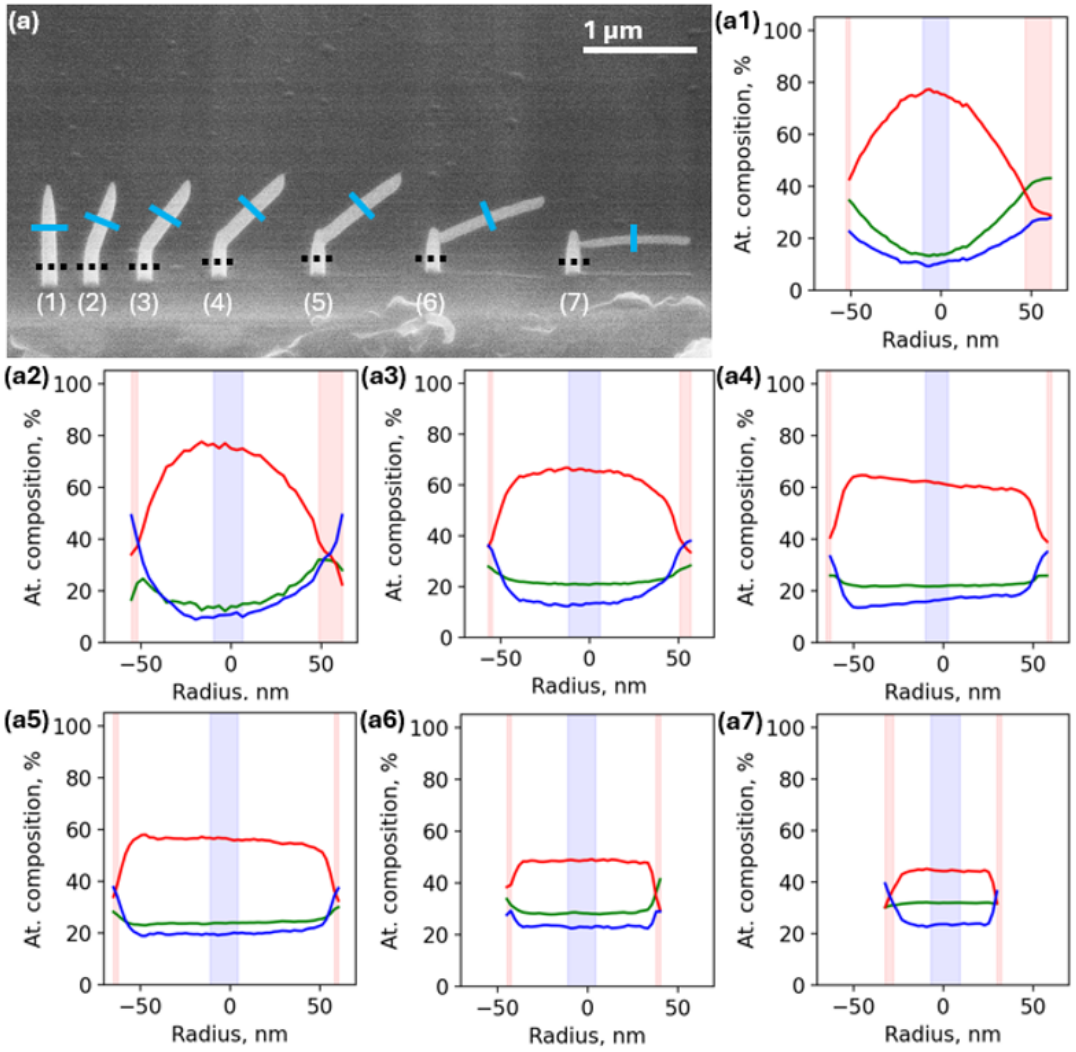

Figure B.5. Characterisation of samples $Co^{\nearrow}_{30\ kV}$. (a) SEM image labelling the NWs and showing areas mapped with STEM EELS. (a1-a7) Compositional maps of the corresponding NWs. Uses the same legend as Figures B.1-B.3.

B.6. Dataset $Co^{\nearrow}_{5\ kV}$

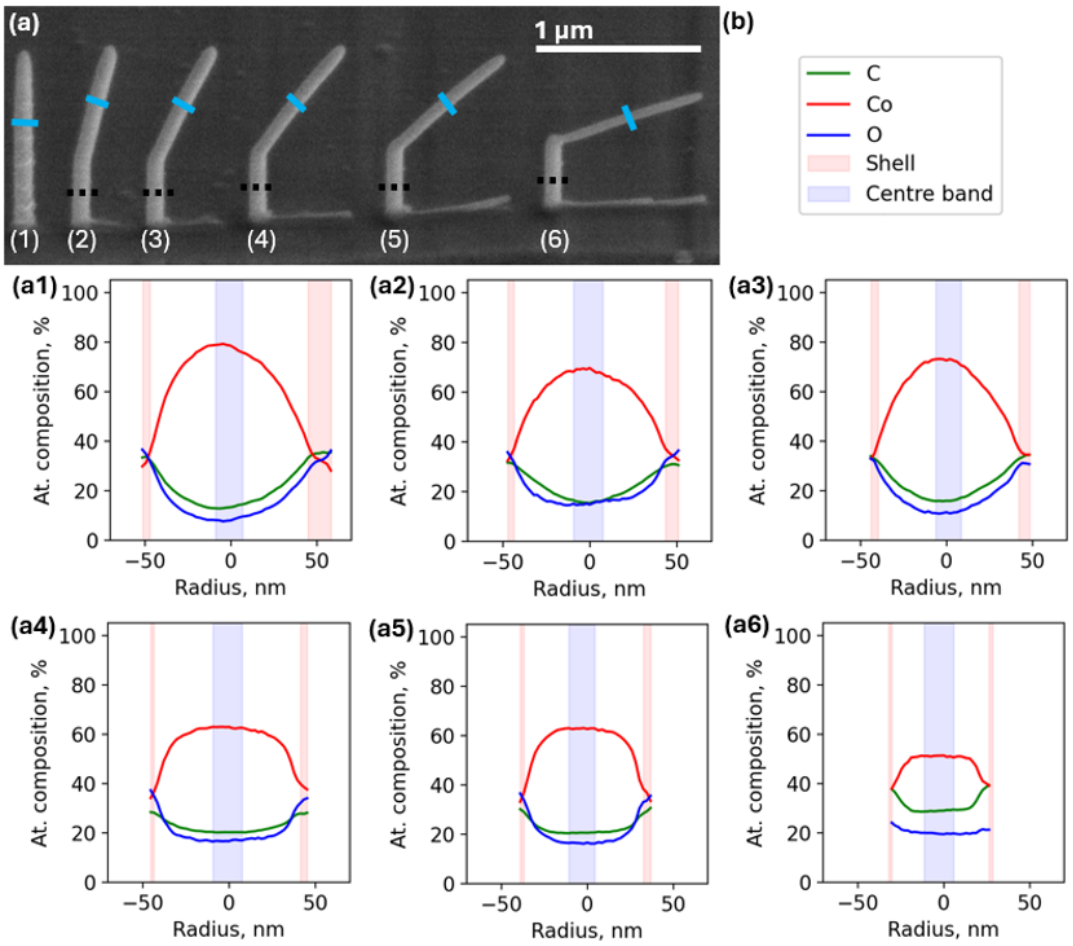

Figure B.6. Characterisation of samples $Co^{\nearrow}_{5\ kV}$. (a) SEM image labelling the NWs and showing areas mapped with STEM EELS. (a1-a6) Compositional maps of the corresponding NWs. (b) Legend.)

B.7. Dataset $Fe^{\nearrow}_{30\ kV}$

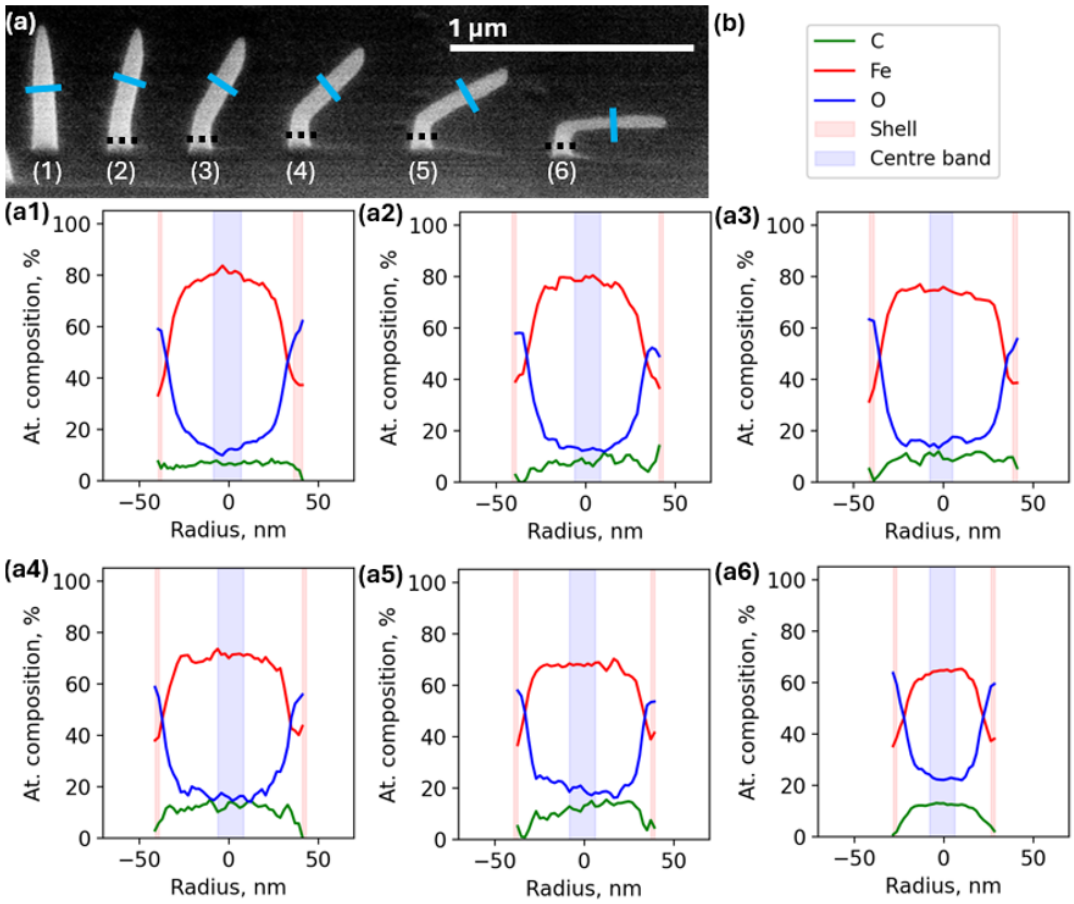

Figure B.7. Characterisation of samples $Fe^{\nearrow}_{30\ kV}$. (a) SEM image labelling the NWs and showing areas mapped with STEM EELS. (a1-a6) Compositional maps of the corresponding NWs. (b) Legend.)

B.8. Dataset $Fe^{\nearrow}_{5\ kV}$

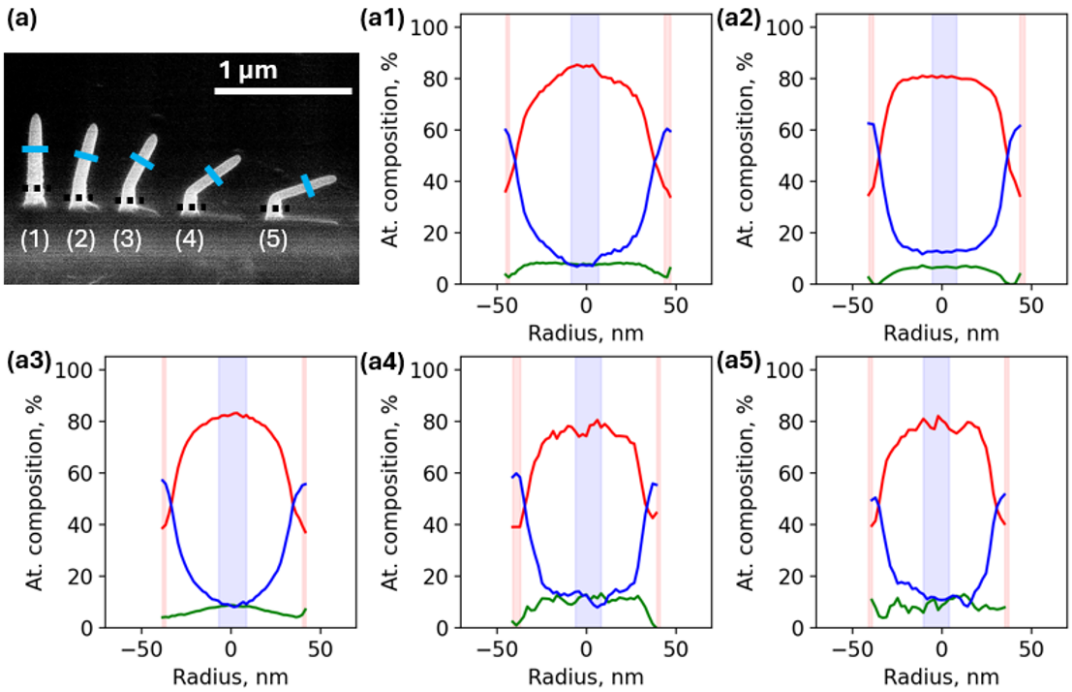

Figure B.8. Characterisation of samples $Fe^{\nearrow}_{5\ kV}$. (a) SEM image labelling the NWs and showing areas mapped with STEM EELS. (a1-a5) Compositional maps of the corresponding NWs. Uses the same legend as Figure B.7.

Bibliography

[1] A. Šilinga, A. Kovács, S. McVitie, R. E. Dunin-Borkowski, K. Fallon, and T. P. Almeida. Model-Based Iterative Reconstruction of Three-Dimensional Magnetization in a Nanowire Structure Using Electron Holographic Vector Field Tomography. *Microscopy and Microanalysis*, 31(3), May 2025. doi:10.1093/mam/ozaf043.

[2] G. E. Moore. Cramming more components onto integrated circuits, Reprinted from Electronics, volume 38, number 8, April 19, 1965, pp.114 ff. *IEEE Solid-State Circuits Society Newsletter*, 11(3):33–35, September 2006. doi:10.1109/N-SSC.2006.4785860.

[3] E. Track, N. Forbes, and G. Strawn. The End of Moore's Law. *Computing in Science & Engineering*, 19(2):4–6, March 2017. doi:10.1109/MCSE.2017.25.

[4] J. Shalf. The future of computing beyond Moore's Law. *Philosophical Transactions of the Royal Society A: Mathematical, Physical and Engineering Sciences*, 378(2166):20190061, January 2020. doi:10.1098/rsta.2019.0061.

[5] F. Zhu, P. Xu, and J. Zong. Moore's Law: The potential, limits, and breakthroughs. *Applied and Computational Engineering*, 10(1):307–315, September 2023. doi:10.54254/2755-2721/10/20230038.

[6] A. Hirohata, K. Yamada, Y. Nakatani, I.-L. Prejbeanu, B. Diény, P. Pirro, and B. Hillebrands. Review on spintronics: Principles and device applications. *Journal of Magnetism and Magnetic Materials*, 509:166711, September 2020. doi:10.1016/j.jmmm.2020.166711.

[7] D. E. Nikonov, G. I. Bourianoff, and P. A. Gargini. Power Dissipation in Spintronic Devices Out of Thermodynamic Equilibrium. *Journal of Superconductivity and Novel Magnetism*, 19(6):497–513, August 2006. doi:10.1007/s10948-006-0148-9.

[8] S. Mao, Y. Chen, F. Liu, X. Chen, B. Xu, P. Lu, M. Patwari, H. Xi, C. Chang,

B. Miller, D. Menard, B. Pant, J. Loven, K. Duxstad, S. Li, Z. Zhang, A. Johnston, R. Lamberton, M. Gubbins, T. McLaughlin, J. Gadbois, J. Ding, B. Cross, S. Xue, and P. Ryan. Commercial TMR heads for hard disk drives: characterization and extendibility at 300 gbit2. *IEEE Transactions on Magnetics*, 42(2):97–102, February 2006. doi:10.1109/TMAG.2005.861788.

[9] J. DeBrosse, D. Gogl, A. Bette, H. Hoenigschmid, R. Robertazzi, C. Arndt, D. Braun, D. Casarotto, R. Havreluk, S. Lammers, W. Obermaier, W. Reohr, H. Viehmann, W. Gallagher, and G. Muller. A high-speed 128-kb MRAM core for future universal memory applications. *IEEE Journal of Solid-State Circuits*, 39(4):678–683, April 2004. doi:10.1109/JSSC.2004.825251.

[10] S. S. P. Parkin, M. Hayashi, and L. Thomas. Magnetic Domain-Wall Racetrack Memory. *Science*, 320(5873):190–194, April 2008. doi:10.1126/science.1145799.

[11] M. O. A. Ellis, A. Welbourne, S. J. Kyle, P. W. Fry, D. A. Allwood, T. J. Hayward, and E. Vasilaki. Machine learning using magnetic stochastic synapses. *Neuromorphic Computing and Engineering*, 3(2):021001, June 2023. doi:10.1088/2634-4386/acdb96.

[12] G. Gubbiotti, A. Barman, S. Ladak, C. Bran, D. Grundler, M. Huth, H. Plank, G. Schmidt, S. van Dijken, R. Streubel, O. Dobrovoloskiy, V. Scagnoli, L. Heyderman, C. Donnelly, O. Hellwig, L. Fallarino, M. B. Jungfleisch, A. Farhan, N. Maccaferri, P. Vavassori, P. Fischer, R. Tomasello, G. Finocchio, R. Clérac, R. Sessoli, D. Makarov, D. D. Sheka, M. Krawczyk, R. Gallardo, P. Landeros, M. d'Aquino, R. Hertel, P. Pirro, F. Ciubotaru, M. Becherer, J. Gartside, T. Ono, P. Bortolotti, and A. Fernández-Pacheco. 2025 roadmap on 3D nanomagnetism. *Journal of Physics: Condensed Matter*, 37(14):143502, February 2025. doi:10.1088/1361-648X/ad9655.

[13] K. Gu, Y. Guan, B. K. Hazra, H. Deniz, A. Migliorini, W. Zhang, and S. S. P. Parkin. Three-dimensional racetrack memory devices designed from freestanding magnetic heterostructures. *Nature Nanotechnology*, 17(10):1065–1071, October 2022. doi:10.1038/s41565-022-01213-1.

[14] R. Streubel, P. Fischer, F. Kronast, V. P. Kravchuk, D. D. Sheka, Y. Gaididei, O. G. Schmidt, and D. Makarov. Magnetism in curved geometries. *Journal of Physics D: Applied Physics*, 49(36):363001, August 2016. doi:10.1088/0022-3727/49/36/363001.

[15] R. Hertel. Curvature-induced magnetochirality. *SPIN*, 03(03):1340009, September 2013. doi:10.1142/S2010324713400092.

[16] H. Young and R. Freedman. *University Physics with Modern Physics, Global Edition*. Pearson Education Ltd., Harlow, UK, 2019. 978-1-292-31481-5.

[17] D. Porter and M. Donahue. Standard Problems in Micromagnetics. In *Compendium on Electromagnetic Analysis*, pages 285–324. World Scientific, June 2020. doi:10.1142/9789813270268_0009.

[18] C. Abert. Spintronics in Micromagnetics. In *Handbook of Materials Modeling*, pages 985–1008. Springer, Cham, 2020. doi:10.1007/978-3-319-44677-6_76.

[19] J. J. Joos, P. Bassirian, P. Gypens, J. Mulkers, K. Litzius, B. Van Waeyenberge, and J. Leliaert. Tutorial: Simulating modern magnetic material systems in mumax3. *Journal of Applied Physics*, 134(17):171101, November 2023. doi:10.1063/5.0160988.

[20] M. A. Ruderman and C. Kittel. Indirect Exchange Coupling of Nuclear Magnetic Moments by Conduction Electrons. *Physical Review*, 96(1):99–102, October 1954. doi:10.1103/PhysRev.96.99.

[21] V. V. Mazurenko, Y. O. Kvashnin, A. I. Lichtenstein, and M. I. Katsnelson. A DMI Guide to Magnets Micro-World. *Journal of Experimental and Theoretical Physics*, 132(4):506–516, April 2021. doi:10.1134/S1063776121040178.

[22] M. J. Donahue and R. D. McMichael. Exchange energy representations in computational micromagnetics. *Physica B: Condensed Matter*, 233(4):272–278, June 1997. doi:10.1016/S0921-4526(97)00310-4.

[23] A. Vansteenkiste, J. Leliaert, M. Dvornik, M. Helsen, F. Garcia-Sanchez, and B. Van Waeyenberge. The design and verification of MuMax3. *AIP Advances*, 4(10):107133, October 2014. doi:10.1063/1.4899186.

[24] A. Fernández-Pacheco, R. Streubel, O. Fruchart, R. Hertel, P. Fischer, and R. P. Cowburn. Three-dimensional nanomagnetism. *Nature Communications*, 8(1):15756, June 2017. doi:10.1038/ncomms15756.

[25] R. Hertel. Computational micromagnetism of magnetization processes in nickel nanowires. *Journal of Magnetism and Magnetic Materials*, 249(1):251–256, August 2002. doi:10.1016/S0304-8853(02)00539-5.

[26] O. Lee, R. Msiska, M. A. Brems, M. Kläui, H. Kurebayashi, and K. Everschor-Sitte. Perspective on unconventional computing using magnetic skyrmions. *Applied Physics Letters*, 122(26):260501, June 2023. doi:10.1063/5.0148469.

[27] M. Yan, C. Andreas, A. Kákay, F. García-Sánchez, and R. Hertel. Fast domain wall dynamics in magnetic nanotubes: Suppression of Walker breakdown and Cherenkov-like spin wave emission. *Applied Physics Letters*, 99(12):122505, September 2011. doi:10.1063/1.3643037.

[28] D. A. Dugato, W. B. F. Jalil, R. Cardias, M. Albuquerque, M. Costa, T. P. Almeida, K. Fallon, A. Kovács, S. McVitie, R. E. Dunin-Borkowski, and F. Garcia. Curved Nanomagnets: An Archetype for the Skyrmionic States at Ambient Conditions. *Nano Letters*, 25(22):8901–8908, June 2025. doi:10.1021/acs.nanolett.5c00773.

[29] D. Sanz-Hernández, L. Skoric, M. Cascales-Sandoval, and A. Fernández-Pacheco. Probing 3D magnetic nanostructures by dark-field magneto-optical Kerr effect. *Journal of Applied Physics*, 133(4):043901, January 2023. doi:10.1063/5.0132250.

[30] A. Hilger, I. Manke, N. Kardjilov, M. Osenberg, H. Markötter, and J. Banhart. Tensorial neutron tomography of three-dimensional magnetic vector fields in bulk materials. *Nature Communications*, 9(1):4023, October 2018. doi:10.1038/s41467-018-06593-4.

[31] C. Donnelly, A. Hierro-Rodríguez, C. Abert, K. Witte, L. Skoric, D. Sanz-Hernández, S. Finizio, F. Meng, S. McVitie, J. Raabe, D. Suess, R. Cowburn, and A. Fernández-Pacheco. Complex free-space magnetic field textures induced by three-dimensional magnetic nanostructures. *Nature Nanotechnology*, 17(2):136–142, February 2022. doi:10.1038/s41565-021-01027-7.

[32] D. B. Williams and C. B. Carter. The Transmission Electron Microscope. In D. B. Williams and C. B. Carter, editors, *Transmission Electron Microscopy: A Textbook for Materials Science*, pages 3–22. Springer US, Boston, MA, 2009. doi:10.1007/978-0-387-76501-3_1.

[33] E. J. R. Vesseur, J. Aizpurua, T. Coenen, A. Reyes-Coronado, P. E. Batson, and A. Polman. Plasmonic excitation and manipulation with an electron beam. *MRS Bulletin*, 37(8):752–760, August 2012. doi:10.1557/mrs.2012.174.

[34] Y. M. Goh, J. Schwartz, E. Rennich, T. Ma, B. Kerns, and R. Hovden. Con-

tamination of TEM Holders Quantified and Mitigated With the Open-Hardware, High-Vacuum Bakeout System. *Microscopy and Microanalysis: The Official Journal of Microscopy Society of America, Microbeam Analysis Society, Microscopical Society of Canada*, 26(5):906–912, October 2020. doi:10.1017/S1431927620001762.

[35] S. Tanuma, C. J. Powell, and D. R. Penn. Calculations of electron inelastic mean free paths. IX. Data for 41 elemental solids over the 50 eV to 30 keV range. *Surface and Interface Analysis*, 43(3):689–713, 2011. doi:10.1002/sia.3522.

[36] D.-N. Le and H. T. Nguyen-Truong. Analytical Formula for the Electron Inelastic Mean Free Path. *The Journal of Physical Chemistry C*, 125(34):18946–18951, September 2021. doi:10.1021/acs.jpcc.1c05212.

[37] R. E. Dunin-Borkowski, A. Kovács, T. Kasama, M. R. McCartney, and D. J. Smith. Electron Holography. In P. W. Hawkes and J. C. H. Spence, editors, *Springer Handbook of Microscopy*, pages 767–818. Springer International Publishing, Cham, 2019. doi:10.1007/978-3-030-00069-1_16.

[38] A. Silinga, C. S. Allen, J. Barthel, C. Ophus, and I. MacLaren. Measurement of Atomic Modulation Direction Using the Azimuthal Variation of First-Order Laue Zone Electron Diffraction. *Microscopy and Microanalysis*, 29(5):1682–1687, October 2023. doi:10.1093/micmic/ozad089.

[39] T. Tanigaki, T. Akashi, T. Yoshida, K. Harada, K. Ishizuka, M. Ichimura, K. Mitsuishi, Y. Tomioka, X. Yu, D. Shindo, Y. Tokura, Y. Murakami, and H. Shinada. Electron holography observation of individual ferrimagnetic lattice planes. *Nature*, 631(8021):521–525, July 2024. doi:10.1038/s41586-024-07673-w.

[40] P. Grundy and R. Tebble. Lorentz electron microscopy. *Advances in Physics*, 17(66):153–242, March 1968. doi:10.1080/00018736800101286.

[41] Y. Aharonov and D. Bohm. Significance of Electromagnetic Potentials in the Quantum Theory. *Physical Review*, 115(3):485–491, August 1959. doi:10.1103/PhysRev.115.485.

[42] C. Magén, J. Pablo-Navarro, and J. M. De Teresa. Focused-Electron-Beam Engineering of 3D Magnetic Nanowires. *Nanomaterials*, 11(2):402, February 2021. Number: 2 Publisher: Multidisciplinary Digital Publishing Institute. doi:10.3390/nano11020402.

[43] A. Petford-Long and J. Chapman. Lorentz Microscopy. In H. Hopster and H. P.

Oepen, editors, *Magnetic Microscopy of Nanostructures*, pages 67–86. Springer, Berlin, Heidelberg, 2005. doi:10.1007/3-540-26641-0_4.

[44] A. Kohn, A. Habibi, and M. Mayo. Experimental evaluation of the 'transport-of-intensity' equation for magnetic phase reconstruction in Lorentz transmission electron microscopy. *Ultramicroscopy*, 160:44–56, January 2016. doi:10.1016/j.ultramic.2015.09.011.

[45] M. Krajnak, D. McGrouther, D. Maneuski, V. O. Shea, and S. McVitie. Pixelated detectors and improved efficiency for magnetic imaging in STEM differential phase contrast. *Ultramicroscopy*, 165:42–50, June 2016. doi:10.1016/j.ultramic.2016.03.006.

[46] S. McVitie, D. McGrouther, S. McFadzean, D. A. MacLaren, K. J. O'Shea, and M. J. Benitez. Aberration corrected Lorentz scanning transmission electron microscopy. *Ultramicroscopy*, 152:57–62, May 2015. doi:10.1016/j.ultramic.2015.01.003.

[47] M. Lehmann and H. Lichte. Electron Holography. In C. B. Carter and D. B. Williams, editors, *Transmission Electron Microscopy: Diffraction, Imaging, and Spectrometry*, pages 215–232. Springer International Publishing, Cham, 2016. doi:10.1007/978-3-319-26651-0_8.

[48] D. Wolf, N. Biziere, S. Sturm, D. Reyes, T. Wade, T. Niermann, J. Krehl, B. Warot-Fonrose, B. Büchner, E. Snoeck, C. Gatel, and A. Lubk. Holographic vector field electron tomography of three-dimensional nanomagnets. *Communications Physics*, 2(1):1–9, July 2019. doi:10.1038/s42005-019-0187-8.

[49] G. R. Lewis, D. Wolf, A. Lubk, E. Ringe, and P. A. Midgley. WRAP: A wavelet-regularised reconstruction algorithm for magnetic vector electron tomography. *Ultramicroscopy*, 253:113804, November 2023. doi:10.1016/j.ultramic.2023.113804.

[50] B. M. Averick, R. G. Carter, G.-L. Xue, and J. J. More. The MINPACK-2 test problem collection. Technical Report ANL/MCS-TM–150-Rev., Argonne National Lab., IL, June 1992. doi:10.2172/79972.

[51] J. Nocedal and S. J. Wright. Fundamentals of Unconstrained Optimization. In *Numerical Optimization*, pages 10–29. Springer, New York, NY, 2006. doi:10.1007/978-0-387-40065-5_2.

[52] M. J. D. Powell. An efficient method for finding the minimum of a function of several

variables without calculating derivatives. *The Computer Journal*, 7(2):155–162, January 1964. doi:10.1093/comjnl/7.2.155.

[53] R. Fletcher and C. M. Reeves. Function minimization by conjugate gradients. *The Computer Journal*, 7(2):149–154, January 1964. doi:10.1093/comjnl/7.2.149.

[54] C. C. Paige and M. A. Saunders. LSQR: An Algorithm for Sparse Linear Equations and Sparse Least Squares. *ACM Transactions on Mathematical Software*, 8(1):43–71, March 1982. doi:10.1145/355984.355989.

[55] I. A. Tasiu, M. P. Islam, M. K. Prity, N. M. Tasniya, D. Samar, A. U. Mariya, H. Zhou, and J.-W. Gao. Spintronics technology: A comprehensive review of materials, applications, and future trends. *Journal of Science: Advanced Materials and Devices*, 11(1):101087, March 2026. doi:10.1016/j.jsamd.2025.101087.

[56] J. N. Chapman. The investigation of magnetic domain structures in thin foils by electron microscopy. *Journal of Physics D: Applied Physics*, 17(4):623, April 1984. doi:10.1088/0022-3727/17/4/003.

[57] A. Masseboeuf, C. Gatel, P. Bayle-Guillemaud, A. Marty, and J.-C. Toussaint. Lorentz microscopy mapping for domain wall structure study in FePd thin films. *Ultramicroscopy*, 110(1):20–25, December 2009. doi:10.1016/j.ultramic.2009.08.006.

[58] M. J. Benitez, A. Hrabec, A. P. Mihai, T. A. Moore, G. Burnell, D. McGrouther, C. H. Marrows, and S. McVitie. Magnetic microscopy and topological stability of homochiral Néel domain walls in a Pt/Co/AlOx trilayer. *Nature Communications*, 6(1):8957, December 2015. doi:10.1038/ncomms9957.

[59] M. A. Basith, S. McVitie, D. McGrouther, and J. N. Chapman. Reproducible domain wall pinning by linear non-topographic features in a ferromagnetic nanowire. *Applied Physics Letters*, 100(23):232402, June 2012. doi:10.1063/1.4724210.

[60] T.-A. Óvári, G. Ababei, G. Stoian, S. Corodeanu, H. Chiriac, and N. Lupu. Direct observation of magnetic domain walls in glass-coated submicronic amorphous wires. *Scientific Reports*, 14(1):5728, March 2024. doi:10.1038/s41598-024-56359-w.

[61] K. Pei, S. Liu, L. Yang, E. Zhang, R. Zhang, C. Yang, L. Ai, Z. Li, F. Xiu, and R. Che. Controllable Domain Walls in Two-Dimensional Ferromagnetic Material Fe3GeTe2 Based on the Spin-Transfer Torque Effect. *ACS Nano*, 15(12):19513–19521, December 2021. doi:10.1021/acsnano.1c06361.

[62] J. C. Slonczewski. Current-driven excitation of magnetic multilayers. *Journal of Magnetism and Magnetic Materials*, 159(1):L1–L7, June 1996. doi:10.1016/0304-8853(96)00062-5.

[63] H. S. Park, J. S. Baskin, and A. H. Zewail. 4D Lorentz Electron Microscopy Imaging: Magnetic Domain Wall Nucleation, Reversal, and Wave Velocity. *Nano Letters*, 10(9):3796–3803, September 2010. doi:10.1021/nl102861e.

[64] S. Koraltan, F. Porrati, R. Kraft, S. Barth, M. Weigand, C. Abert, D. Suess, M. Huth, and S. Wintz. Reconfigurable 3D Magnetic Nanoarchitectures. *Advanced Functional Materials*, 35(50):e15338, 2025. doi:10.1002/adfm.202515338.

[65] A. Fernández-Pacheco, L. Skoric, J. M. De Teresa, J. Pablo-Navarro, M. Huth, and O. V. Dobrovolskiy. Writing 3D Nanomagnets Using Focused Electron Beams. *Materials*, 13(17):3774, January 2020. doi:10.3390/ma13173774.

[66] J. Fullerton and C. Phatak. Design and Control of Three-Dimensional Topological Magnetic Fields Using Interwoven Helical Nanostructures. *Nano Letters*, 25(13):5148–5155, April 2025. doi:10.1021/acs.nanolett.4c06152.

[67] L. Keller, M. K. I. Al Mamoori, J. Pieper, C. Gspan, I. Stockem, C. Schröder, S. Barth, R. Winkler, H. Plank, M. Pohlit, J. Müller, and M. Huth. Direct-write of free-form building blocks for artificial magnetic 3D lattices. *Scientific Reports*, 8(1):6160, April 2018. doi:10.1038/s41598-018-24431-x.

[68] J. Fullerton, J. Koenig, and C. Phatak. Magnetic solitons and thickness-dependent magnetization reversal in interconnected helical nanowire arrays. *Advanced Physics Research*, 5(2):e00135, 2026. doi:10.1002/apxr.202500135.

[69] D. Wolf, S. Schneider, U. K. Rößler, A. Kovács, M. Schmidt, R. E. Dunin-Borkowski, B. Büchner, B. Rellinghaus, and A. Lubk. Unveiling the three-dimensional magnetic texture of skyrmion tubes. *Nature Nanotechnology*, 17(3):250–255, March 2022. doi:10.1038/s41565-021-01031-x.

[70] L. E. Franken, K. Grünewald, E. J. Boekema, and M. C. A. Stuart. A Technical Introduction to Transmission Electron Microscopy for Soft-Matter: Imaging, Possibilities, Choices, and Technical Developments. *Small*, 16(14):1906198, 2020. doi:10.1002/smll.201906198.

[71] K. D. Vernon-Parry. Scanning electron microscopy: an introduction. *III-Vs Review*, 13(4):40–44, July 2000. doi:10.1016/S0961-1290(00)80006-X.

[72] D. B. Williams and C. B. Carter. Lenses, Apertures, and Resolution. In D. B. Williams and C. B. Carter, editors, *Transmission Electron Microscopy: A Textbook for Materials Science*, pages 91–114. Springer US, Boston, MA, 2009. doi:10.1007/978-0-387-76501-3_6.

[73] T. E. Everhart and R. F. M. Thornley. Wide-band detector for micro-microampere low-energy electron currents. *Journal of Scientific Instruments*, 37(7):246, July 1960. doi:10.1088/0950-7671/37/7/307.

[74] D. C. Joy and C. S. Joy. Low voltage scanning electron microscopy. *Micron*, 27(3):247–263, June 1996. doi:10.1016/0968-4328(96)00023-6.

[75] S. Töberg and E. Reithmeier. Quantitative 3D Reconstruction from Scanning Electron Microscope Images Based on Affine Camera Models. *Sensors*, 20(12):3598, January 2020. doi:10.3390/s20123598.

[76] P. J. Goodhew, J. Humphreys, and J. Humphreys. *Electron Microscopy and Analysis*. CRC Press, London, 3 edition, November 2000. doi:10.1201/9781482289343.

[77] W. Zhou, R. Apkarian, Z. L. Wang, and D. Joy. Fundamentals of Scanning Electron Microscopy (SEM). In W. Zhou and Z. L. Wang, editors, *Scanning Microscopy for Nanotechnology: Techniques and Applications*, pages 1–40. Springer, New York, NY, 2007. doi:10.1007/978-0-387-39620-0_1.

[78] P. de Vera, M. Azzolini, G. Sushko, I. Abril, R. Garcia-Molina, M. Dapor, I. A. Solovyov, and A. V. Solovyov. Multiscale simulation of the focused electron beam induced deposition process. *Scientific Reports*, 10(1):20827, November 2020. doi:10.1038/s41598-020-77120-z.

[79] L. Skoric, D. Sanz-Hernández, F. Meng, C. Donnelly, S. Merino-Aceituno, and A. Fernández-Pacheco. Layer-by-Layer Growth of Complex-Shaped Three-Dimensional Nanostructures with Focused Electron Beams. *Nano Letters*, 20(1):184–191, January 2020. doi:10.1021/acs.nanolett.9b03565.

[80] D. Sanz-Hernández, A. Hierro-Rodriguez, C. Donnelly, J. Pablo-Navarro, A. Sorrentino, E. Pereiro, C. Magén, S. McVitie, J. M. de Teresa, S. Ferrer, P. Fischer, and A. Fernández-Pacheco. Artificial Double-Helix for Geometrical Control of Magnetic Chirality. *ACS Nano*, 14(7):8084–8092, July 2020. doi:10.1021/acsnano.0c00720.

[81] R. Winkler, J. D. Fowlkes, P. D. Rack, G. Kothleitner, and H. Plank. Shape

evolution and growth mechanisms of 3D-printed nanowires. *Additive Manufacturing*, 46:102076, October 2021. doi:10.1016/j.addma.2021.102076.

[82] R. Córdoba, N. Sharma, S. Kölling, P. M. Koenraad, and B. Koopmans. High-purity 3D nano-objects grown by focused-electron-beam induced deposition. *Nanotechnology*, 27(35):355301, July 2016. doi:10.1088/0957-4484/27/35/355301.

[83] V. Reisecker, R. Winkler, and H. Plank. A Review on Direct-Write Nanoprinting of Functional 3D Structures with Focused Electron Beams. *Advanced Functional Materials*, 34(46):2407567, 2024. doi:10.1002/adfm.202407567.

[84] C. Hetherington. Aberration correction for TEM. *Materials Today*, 7(12):50–55, December 2004. doi:10.1016/S1369-7021(04)00571-1.

[85] N. Tanaka. Present status and future prospects of spherical aberration corrected TEM and STEM for study of nanomaterials. *Science and Technology of Advanced Materials*, 9(1):014111, June 2008. doi:10.1088/1468-6996/9/1/014111.

[86] D. B. Williams and C. B. Carter. The Instrument. In D. B. Williams and C. B. Carter, editors, *Transmission Electron Microscopy: A Textbook for Materials Science*, pages 141–171. Springer US, Boston, MA, 2009. doi:10.1007/978-0-387-76501-3_9.

[87] D. B. Williams and C. B. Carter. Electron Energy-Loss Spectrometers and Filters. In D. B. Williams and C. B. Carter, editors, *Transmission Electron Microscopy: A Textbook for Materials Science*, pages 679–698. Springer US, Boston, MA, 2009. doi:10.1007/978-0-387-76501-3_37.

[88] M. Haider, H. Rose, S. Uhlemann, E. Schwan, B. Kabius, and K. Urban. A spherical-aberration-corrected 200 kV transmission electron microscope. *Ultramicroscopy*, 75(1):53–60, October 1998. doi:10.1016/S0304-3991(98)00048-5.

[89] D. B. Williams and C. B. Carter. How to 'See' Electrons. In D. B. Williams and C. B. Carter, editors, *Transmission Electron Microscopy: A Textbook for Materials Science*, pages 115–126. Springer US, Boston, MA, 2009. doi:10.1007/978-0-387-76501-3_7.

[90] P. Ercius, I. J. Johnson, P. Pelz, B. H. Savitzky, L. Hughes, H. G. Brown, S. E. Zeltmann, S.-L. Hsu, C. C. S. Pedroso, B. E. Cohen, R. Ramesh, D. Paul, J. M. Joseph, T. Stezelberger, C. Czarnik, M. Lent, E. Fong, J. Ciston, M. C. Scott, C. Ophus, A. M. Minor, and P. Denes. The 4D Camera: An 87 kHz Direct

Electron Detector for Scanning/Transmission Electron Microscopy. *Microscopy and Microanalysis*, 30(5):903–912, November 2024. doi:10.1093/mam/ozae086.

[91] D. B. Williams and C. B. Carter. Amplitude Contrast. In D. B. Williams and C. B. Carter, editors, *Transmission Electron Microscopy: A Textbook for Materials Science*, pages 371–388. Springer US, Boston, MA, 2009. doi:10.1007/978-0-387-76501-3_22.

[92] D. B. Williams and C. B. Carter. High Energy-Loss Spectra and Images. In D. B. Williams and C. B. Carter, editors, *Transmission Electron Microscopy: A Textbook for Materials Science*, pages 715–739. Springer US, Boston, MA, 2009. doi:10.1007/978-0-387-76501-3_39.

[93] J. C. Slater. A Simplification of the Hartree-Fock Method. *Physical Review*, 81(3):385–390, February 1951. doi:10.1103/PhysRev.81.385.

[94] A. J. Craven, B. Sala, J. Bobynko, and I. MacLaren. Spectrum imaging of complex nanostructures using DualEELS: II. Absolute quantification using standards. *Ultramicroscopy*, 186:66–81, March 2018. doi:10.1016/j.ultramic.2017.12.011.

[95] J. Scott, P. J. Thomas, M. MacKenzie, S. McFadzean, J. Wilbrink, A. J. Craven, and W. A. P. Nicholson. Near-simultaneous dual energy range EELS spectrum imaging. *Ultramicroscopy*, 108(12):1586–1594, November 2008. doi:10.1016/j.ultramic.2008.05.006.

[96] A. J. Craven, B. Sala, D. A. MacLaren, S. McFadzean, B. Schaffer, and I. MacLaren. Splicing dual-range EELS spectra: Identifying and correcting artefacts. *Ultramicroscopy*, 272:114135, June 2025. doi:10.1016/j.ultramic.2025.114135.

[97] F. Hofer, F. P. Schmidt, W. Grogger, and G. Kothleitner. Fundamentals of electron energy-loss spectroscopy. *IOP Conference Series: Materials Science and Engineering*, 109(1):012007, January 2016. doi:10.1088/1757-899X/109/1/012007.

[98] H. Tan, J. Verbeeck, A. Abakumov, and G. Van Tendeloo. Oxidation state and chemical shift investigation in transition metal oxides by EELS. *Ultramicroscopy*, 116:24–33, May 2012. doi:10.1016/j.ultramic.2012.03.002.

[99] C. Cherqui, N. Thakkar, G. Li, J. P. Camden, and D. J. Masiello. Characterizing Localized Surface Plasmons Using Electron Energy-Loss Spectroscopy. *Annual Review of Physical Chemistry*, 67(Volume 67, 2016):331–357, May 2016. doi:

10.1146/annurev-physchem-040214-121612.

[100] O. L. Krivanek, N. Dellby, J. A. Hachtel, J. C. Idrobo, M. T. Hotz, B. Plotkin-Swing, N. J. Bacon, A. L. Bleloch, G. J. Corbin, M. V. Hoffman, C. E. Meyer, and T. C. Lovejoy. Progress in ultrahigh energy resolution EELS. *Ultramicroscopy*, 203:60–67, August 2019. doi:10.1016/j.ultramic.2018.12.006.

[101] C. Colliex. From early to present and future achievements of EELS in the TEM. *The European Physical Journal Applied Physics*, 97:38, 2022. doi:10.1051/epjap/2022220012.

[102] A. Tonomura. Applications of electron holography. *Reviews of Modern Physics*, 59(3):639–669, July 1987. doi:10.1103/RevModPhys.59.639.

[103] H. Lichte. Gottfried Möllenstedt and his electron biprism: four decades of challenging and exciting electron physics. *Journal of Electron Microscopy*, 47(5):387–394, January 1998. doi:10.1093/oxfordjournals.jmicro.a023609.

[104] C. Phatak, M. Beleggia, and M. De Graef. Vector field electron tomography of magnetic materials: Theoretical development. *Ultramicroscopy*, 108(6):503–513, May 2008. doi:10.1016/j.ultramic.2007.08.002.

[105] K. C. Prabhat, K. Aditya Mohan, C. Phatak, C. Bouman, and M. De Graef. 3D reconstruction of the magnetic vector potential using model based iterative reconstruction. *Ultramicroscopy*, 182:131–144, November 2017. doi:10.1016/j.ultramic.2017.07.005.

[106] D. A. Broadway, M. Flaks, A. E. Dubois, and P. Maletinsky. Reconstruction of nontrivial magnetization textures from magnetic field images using neural networks. *Physical Review Applied*, 23(4):044012, April 2025. doi:10.1103/PhysRevApplied.23.044012.

[107] B. Lyu, S. Zhao, Y. Zhang, W. Wang, F. Zheng, R. E. Dunin-Borkowski, J. Zang, and H. Du. Three-dimensional magnetization reconstruction from electron optical phase images with physical constraints. *Science China Physics, Mechanics & Astronomy*, 67(11):117511, September 2024. doi:10.1007/s11433-024-2448-6.

[108] R. P. Feynman. Space-Time Approach to Quantum Electrodynamics. *Physical Review*, 76(6):769–789, September 1949. doi:10.1103/PhysRev.76.769.

[109] G. L. Light. Electromagnetism in the Standard Model. *International Journal of*

Applied Mathematics, 28(5):541–555, October 2015. doi:10.12732/ijam.v28i5.7.

[110] A. Caprez, B. Barwick, and H. Batelaan. Macroscopic Test of the Aharonov-Bohm Effect. *Physical Review Letters*, 99(21):210401, November 2007. doi:10.1103/PhysRevLett.99.210401.

[111] E. Comay. The Rise and Fall of the Electromagnetic 4-Potential. *Open Access Library Journal*, 5(11):1–18, November 2018. doi:10.4236/oalib.1104979.

[112] F. Zheng, V. Migunov, J. Caron, H. Du, G. Pozzi, and R. E. Dunin-Borkowski. Nanoscale Three-Dimensional Charge Density and Electric Field Mapping by Electron Holographic Tomography. *Nano Letters*, 23(3):843–849, February 2023. doi:10.1021/acs.nanolett.2c03879.

[113] M. Wu, A. Tafel, P. Hommelhoff, and E. Spiecker. Determination of 3D electrostatic field at an electron nano-emitter. *Applied Physics Letters*, 114(1), January 2019. doi:10.1063/1.5055227.

[114] S. Rohart and A. Thiaville. Skyrmion confinement in ultrathin film nanostructures in the presence of Dzyaloshinskii-Moriya interaction. *Physical Review B*, 88(18):184422, November 2013. doi:10.1103/PhysRevB.88.184422.

[115] I. I. Lobanova, S. Despréaux, S. Labbé, C. Celada-Casero, and F. van den Berg. Micromagnetic modelling of magnetostriction under uniaxial stress. *Journal of Magnetism and Magnetic Materials*, 564:170028, December 2022. doi:10.1016/j.jmmm.2022.170028.

[116] T. Gilbert. A phenomenological theory of damping in ferromagnetic materials. *IEEE Transactions on Magnetics*, 40(6):3443–3449, November 2004. doi:10.1109/TMAG.2004.836740.

[117] M. J. Donahue. OOMMF User's Guide, Version 1.0. *NIST*, September 1999. doi:10.6028/NIST.IR.6376.

[118] A. Vansteenkiste and B. Van de Wiele. MuMax: A new high-performance micromagnetic simulation tool. *Journal of Magnetism and Magnetic Materials*, 323(21):2585–2591, November 2011. doi:10.1016/j.jmmm.2011.05.037.

[119] P. Ó Conbhuí, W. Williams, K. Fabian, P. Ridley, L. Nagy, and A. R. Muxworthy. MERRILL: Micromagnetic Earth Related Robust Interpreted Language Laboratory. *Geochemistry, Geophysics, Geosystems*, 19(4):1080–1106, April 2018. doi:10.1002/

2017GC007279.

[120] J. M. De Teresa, A. Fernández-Pacheco, R. Córdoba, L. Serrano-Ramón, S. Sangiao, and M. R. Ibarra. Review of magnetic nanostructures grown by focused electron beam induced deposition (FEBID). *Journal of Physics D: Applied Physics*, 49(24):243003, May 2016. doi:10.1088/0022-3727/49/24/243003.

[121] I. Utke, P. Swiderek, K. Höflich, K. Madajska, J. Jurczyk, P. Martinović, and I. B. Szymańska. Coordination and organometallic precursors of group 10 and 11: Focused electron beam induced deposition of metals and insight gained from chemical vapour deposition, atomic layer deposition, and fundamental surface and gas phase studies. *Coordination Chemistry Reviews*, 458:213851, May 2022. doi:10.1016/j.ccr.2021.213851.

[122] A. Botman, J. J. L. Mulders, and C. W. Hagen. Creating pure nanostructures from electron-beam-induced deposition using purification techniques: a technology perspective. *Nanotechnology*, 20(37):372001, August 2009. doi:10.1088/0957-4484/20/37/372001.

[123] K. Muthukumar, H. O. Jeschke, R. Valentí, E. Begun, J. Schwenk, F. Porrati, and M. Huth. Spontaneous dissociation of Co2(CO)8 and autocatalytic growth of Co on SiO2: A combined experimental and theoretical investigation. *Beilstein Journal of Nanotechnology*, 3(1):546–555, July 2012. doi:10.3762/bjnano.3.63.

[124] R. E. Winters and R. W. Kiser. Ions Produced by Electron Impact with the Dimetallic Carbonyls of Cobalt and Manganese1. *The Journal of Physical Chemistry*, 69(5):1618–1622, May 1965. doi:10.1021/j100889a029.

[125] J. A. Connor, H. A. Skinner, and Y. Virmani. High temperature microcalorimetric studies of the thermal decomposition and iodination of polynuclear carbonyls of Fe, Co, Ru, Rh, Re, Os and Ir. *Faraday Symposia of the Chemical Society*, 8(0):18–28, January 1973. doi:10.1039/FS9730800018.

[126] E. M. Markin and K.-i. Sugawara. Energy-Resolved Collision-Induced Dissociation of Fe2(CO)y. *The Journal of Physical Chemistry A*, 104(7):1416–1422, February 2000. doi:10.1021/jp993434t.

[127] J. Dewar and H. O. Jones. On a new Iron carbonyl, and on the action of light and of heat on the Iron carbonyls. *Proceedings of the Royal Society of London. Series A, Containing Papers of a Mathematical and Physical Character*, 79(527):66–80,

March 1907. doi:10.1098/rspa.1907.0015.

[128] L. Bertini, C. Greco, L. De Gioia, and P. Fantucci. Time-Dependent Density Functional Theory Study of Fe2(CO)9 Low-Lying Electronic Excited States. *The Journal of Physical Chemistry A*, 110(47):12900–12907, November 2006. doi:10.1021/jp0646022.

[129] G. Hochleitner, H. D. Wanzenboeck, and E. Bertagnolli. Electron beam induced deposition of iron nanostructures. *Journal of Vacuum Science & Technology B: Microelectronics and Nanometer Structures Processing, Measurement, and Phenomena*, 26(3):939–944, April 2008. doi:10.1116/1.2907781.

[130] J. Pablo-Navarro, D. Sanz-Hernández, C. Magén, A. Fernández-Pacheco, and J. M. de Teresa. Tuning shape, composition and magnetization of 3D cobalt nanowires grown by focused electron beam induced deposition (FEBID). *Journal of Physics D: Applied Physics*, 50(18):18LT01, April 2017. doi:10.1088/1361-6463/aa63b4.

[131] L. Serrano-Ramón, R. Córdoba, L. A. Rodríguez, C. Magén, E. Snoeck, C. Gatel, I. Serrano, M. R. Ibarra, and J. M. De Teresa. Ultrasmall Functional Ferromagnetic Nanostructures Grown by Focused Electron-Beam-Induced Deposition. *ACS Nano*, 5(10):7781–7787, October 2011. doi:10.1021/nn201517r.

[132] R. Córdoba, J. Sesé, J. M. De Teresa, and M. R. Ibarra. High-purity cobalt nanostructures grown by focused-electron-beam-induced deposition at low current. *Microelectronic Engineering*, 87(5):1550–1553, May 2010. doi:10.1016/j.mee.2009.11.027.

[133] C. Trummer, R. Winkler, H. Plank, G. Kothleitner, and G. Haberfehlner. Analyzing the Nanogranularity of Focused-Electron-Beam-Induced-Deposited Materials by Electron Tomography. *ACS Applied Nano Materials*, 2(9):5356–5359, September 2019. doi:10.1021/acsanm.9b01390.

[134] H. Plank, R. Winkler, C. H. Schwalb, J. Hütner, J. D. Fowlkes, P. D. Rack, I. Utke, and M. Huth. Focused Electron Beam-Based 3D Nanoprinting for Scanning Probe Microscopy: A Review. *Micromachines*, 11(1):48, January 2020. doi:10.3390/mi11010048.

[135] F. Porrati, R. Sachser, C. H. Schwalb, A. S. Frangakis, and M. Huth. Tuning the electrical conductivity of Pt-containing granular metals by postgrowth electron irradiation. *Journal of Applied Physics*, 109(6):063715, March 2011. doi:10.1063/

1.3559773.

[136] E. Begun, O. V. Dobrovolskiy, M. Kompaniiets, R. Sachser, C. Gspan, H. Plank, and M. Huth. Post-growth purification of Co nanostructures prepared by focused electron beam induced deposition. *Nanotechnology*, 26(7):075301, January 2015. doi:10.1088/0957-4484/26/7/075301.

[137] M. V. Puydinger dos Santos, M. F. Velo, R. D. Domingos, Y. Zhang, X. Maeder, C. Guerra-Nuñez, J. P. Best, F. Béron, K. R. Pirota, S. Moshkalev, J. A. Diniz, and I. Utke. Annealing-Based Electrical Tuning of Cobalt–Carbon Deposits Grown by Focused-Electron-Beam-Induced Deposition. *ACS Applied Materials & Interfaces*, 8(47):32496–32503, November 2016. doi:10.1021/acsami.6b12192.

[138] T. Almeida, D. Mcgrouther, A. Kovács, R. Dunin-Borkowski, and S. Mcvitie. Effect of annealing on the magnetic states of FEBID-grown cobalt nanopatterns examined by off-axis electron holography. *Journal of Microscopy*, 279(3):217–221, 2020. doi:10.1111/jmi.12869.

[139] M. J. Martínez-Pérez, J. Pablo-Navarro, B. Müller, R. Kleiner, C. Magén, D. Koelle, J. M. de Teresa, and J. Sesé. NanoSQUID Magnetometry on Individual As-grown and Annealed Co Nanowires at Variable Temperature. *Nano Letters*, 18(12):7674–7682, December 2018. doi:10.1021/acs.nanolett.8b03329.

[140] J. Pablo-Navarro, C. Magén, and J. M. de Teresa. Purified and Crystalline Three-Dimensional Electron-Beam-Induced Deposits: The Successful Case of Cobalt for High-Performance Magnetic Nanowires. *ACS Applied Nano Materials*, 1(1):38–46, January 2018. doi:10.1021/acsanm.7b00016.

[141] J. Pablo-Navarro, R. Winkler, G. Haberfehlner, C. Magén, H. Plank, and J. M. De Teresa. *In situ* real-time annealing of ultrathin vertical Fe nanowires grown by focused electron beam induced deposition. *Acta Materialia*, 174:379–386, August 2019. doi:10.1016/j.actamat.2019.05.035.

[142] M. Shimojo, M. Takeguchi, R. Che, W. Zhang, M. Tanaka, K. Mitsuishi, and K. Furuya. Effects of Heat Treatment on Electric Properties of Nanorods Formed by Electron Beam-Induced Deposition. *Japanese Journal of Applied Physics*, 45(6):5509, June 2006. doi:10.1143/JJAP.45.5509.

[143] M. Toth, C. Lobo, V. Friedli, A. Szkudlarek, and I. Utke. Continuum models of focused electron beam induced processing. *Beilstein Journal of Nanotechnology*,

6(1):1518–1540, July 2015. doi:10.3762/bjnano.6.157.

[144] D. Sanz-Hernández, R. F. Hamans, J.-W. Liao, A. Welbourne, R. Lavrijsen, and A. Fernández-Pacheco. Fabrication, Detection, and Operation of a Three-Dimensional Nanomagnetic Conduit. *ACS Nano*, 11(11):11066–11073, November 2017. doi:10.1021/acsnano.7b05105.

[145] A. Prosvetov, A. V. Verkhovtsev, G. Sushko, and A. V. Solovyov. Atomistic simulation of the FEBID-driven growth of iron-based nanostructures. *Physical Chemistry Chemical Physics*, 24(18):10807–10819, May 2022. doi:10.1039/D2CP00809B.

[146] A. Prosvetov, A. V. Verkhovtsev, G. Sushko, and A. V. Solovyov. Atomistic modeling of thermal effects in focused electron beam-induced deposition of Me_2\Au(tfac). *The European Physical Journal D*, 77(1):15, January 2023. doi:10.1140/epjd/s10053-023-00598-5.

[147] S. J. Randolph, J. D. Fowlkes, and P. D. Rack. Focused, Nanoscale Electron-Beam-Induced Deposition and Etching. *Critical Reviews in Solid State and Materials Sciences*, 31(3):55–89, September 2006. doi:10.1080/10408430600930438.

[148] A. Fernández-Pacheco, J. M. De Teresa, R. Córdoba, and M. R. Ibarra. Magnetotransport properties of high-quality cobalt nanowires grown by focused-electron-beam-induced deposition. *Journal of Physics D: Applied Physics*, 42(5):055005, February 2009. doi:10.1088/0022-3727/42/5/055005.

[149] F. Vollnhals, M. Drost, F. Tu, E. Carrasco, A. Späth, R. H. Fink, H.-P. Steinrück, and H. Marbach. Electron-beam induced deposition and autocatalytic decomposition of Co(CO)3NO. *Beilstein Journal of Nanotechnology*, 5(1):1175–1185, July 2014. doi:10.3762/bjnano.5.129.

[150] I. Utke, J. Michler, P. Gasser, C. Santschi, D. Laub, M. Cantoni, P. A. Buffat, C. Jiao, and P. Hoffmann. Cross Section Investigations of Compositions and Sub-Structures of Tips Obtained by Focused Electron Beam Induced Deposition. *Advanced Engineering Materials*, 7(5):323–331, 2005. doi:10.1002/adem.200500061.

[151] I. Utke, P. Hoffmann, R. Berger, and L. Scandella. High-resolution magnetic Co supertips grown by a focused electron beam. *Applied Physics Letters*, 80(25):4792–4794, June 2002. doi:10.1063/1.1489097.

[152] R. Winkler, B. Lewis, J. Fowlkes, P. Rack, and H. Plank. High-Fidelity 3D-Nanoprinting via Focused Electron Beams: Growth Fundamentals. *ACS Applied*

Nano Materials, 1(3):1014–1027, March 2018. doi:10.1021/acsanm.8b00158.

[153] H. Plank, C. Gspan, M. Dienstleder, G. Kothleitner, and F. Hofer. The influence of beam defocus on volume growth rates for electron beam induced platinum deposition. *Nanotechnology*, 19(48):485302, November 2008. doi:10.1088/0957-4484/19/48/485302.

[154] A. J. Craven, J. A. Wilson, and W. A. P. Nicholson. A fast beam switch for controlling the intensity in electron energy loss spectrometry. *Ultramicroscopy*, 92(3):165–180, August 2002. doi:10.1016/S0304-3991(02)00130-4.

[155] A. J. Craven, M. MacKenzie, and S. McFadzean. Dual energy range EELS spectrum imaging using a fast beam switch. In M. Luysberg, K. Tillmann, and T. Weirich, editors, *EMC 2008 14th European Microscopy Congress 1–5 September 2008, Aachen, Germany*, pages 363–364. Springer, 2008. doi:10.1007/978-3-540-85156-1_182.

[156] G. Lucas, P. Burdet, M. Cantoni, and C. Hébert. Multivariate statistical analysis as a tool for the segmentation of 3D spectral data. *Micron*, 52-53:49–56, September 2013. doi:10.1016/j.micron.2013.08.005.

[157] L. R. Castillo-Rico, M. A. Flores-Mancera, and G. Massillon-JL. Stopping power and CSDA range of electrons in liquid water, LiF, CaF2, and Al2O3 from the energy gap up to 433 keV. *Nuclear Instruments and Methods in Physics Research Section B: Beam Interactions with Materials and Atoms*, 502:189–197, September 2021. doi:10.1016/j.nimb.2021.07.002.

[158] E. Völkl, L. F. Allard, and B. Frost. A software package for the processing and reconstruction of electron holograms. *Journal of Microscopy*, 180(1):39–50, 1995. doi:10.1111/j.1365-2818.1995.tb03655.x.

[159] V. Boureau, R. McLeod, B. Mayall, and D. Cooper. Off-axis electron holography combining summation of hologram series with double-exposure phase-shifting: Theory and application. *Ultramicroscopy*, 193:52–63, October 2018. doi:10.1016/j.ultramic.2018.06.004.

[160] D. R. G. Mitchell and B. Schaffer. Scripting-customised microscopy tools for Digital Micrograph™. *Ultramicroscopy*, 103(4):319–332, July 2005. doi:10.1016/j.ultramic.2005.02.003.

[161] L. A. Rodríguez, L. Deen, R. Córdoba, C. Magén, E. Snoeck, B. Koopmans, and J. M. D. Teresa. Influence of the shape and surface oxidation in the magnetization

reversal of thin iron nanowires grown by focused electron beam induced deposition. *Beilstein Journal of Nanotechnology*, 6(1):1319–1331, June 2015. doi:10.3762/bjnano.6.136.

[162] A. Akhtari-Zavareh, M. De Graef, and K. L. Kavanagh. Magnetic phase shift reconstruction for uniformly magnetized nanowires. *Ultramicroscopy*, 172:10–16, January 2017. doi:10.1016/j.ultramic.2016.10.002.

[163] E. Snoeck, R. E. Dunin-Borkowski, F. Dumestre, P. Renaud, C. Amiens, B. Chaudret, and P. Zurcher. Quantitative magnetization measurements on nanometer ferromagnetic cobalt wires using electron holography. *Applied Physics Letters*, 82(1):88–90, January 2003. doi:10.1063/1.1532754.

[164] J. Crangle and G. M. Goodman. The magnetization of pure iron and nickel. *Proceedings of the Royal Society of London. A. Mathematical and Physical Sciences*, 321(1547):477–491, March 1971. doi:10.1098/rspa.1971.0044.

[165] J. C. Ashley, C. J. Tung, R. H. Ritchie, and V. E. Anderson. Calculations of mean free paths and stopping powers of low energy electrons (less than 10 keV) in solids using a statistical model. *IEEE Transactions on Nuclear Science*, 23(6):1833–1837, December 1976. doi:10.1109/TNS.1976.4328586.

[166] H. D. Wanzenboeck, G. Hochleitner, J. Mika, M. M. Shawrav, M. Gavagnin, and E. Bertagnolli. Mapping of local argon impingement on a virtual surface: an insight for gas injection during FEBID. *Applied Physics A*, 117(4):1749–1756, December 2014. doi:10.1007/s00339-014-8755-y.

[167] F. Zheng, N. S. Kiselev, F. N. Rybakov, L. Yang, W. Shi, S. Blügel, and R. E. Dunin-Borkowski. Hopfion rings in a cubic chiral magnet. *Nature*, 623(7988):718–723, November 2023. doi:10.1038/s41586-023-06658-5.

[168] C. Donnelly, S. Finizio, S. Gliga, M. Holler, A. Hrabec, M. Odstrčil, S. Mayr, V. Scagnoli, L. J. Heyderman, M. Guizar-Sicairos, and J. Raabe. Time-resolved imaging of three-dimensional nanoscale magnetization dynamics. *Nature Nanotechnology*, 15(5):356–360, May 2020. doi:10.1038/s41565-020-0649-x.

[169] C. Donnelly, M. Guizar-Sicairos, V. Scagnoli, S. Gliga, M. Holler, J. Raabe, and L. J. Heyderman. Three-dimensional magnetization structures revealed with X-ray vector nanotomography. *Nature*, 547(7663):328–331, July 2017. doi:10.1038/nature23006.

[170] M. Di Pietro Martínez, A. Wartelle, C. Herrero Martínez, F. Fettar, F. Blondelle, J.-F. Motte, C. Donnelly, L. Turnbull, F. Ogrin, G. van der Laan, H. Popescu, N. Jaouen, F. Yakhou-Harris, and G. Beutier. Three-dimensional tomographic imaging of the magnetization vector field using Fourier transform holography. *Physical Review B*, 107(9):094425, March 2023. doi:10.1103/PhysRevB.107.094425.

[171] C. Phatak, A. K. Petford-Long, and M. De Graef. Three-Dimensional Study of the Vector Potential of Magnetic Structures. *Physical Review Letters*, 104(25):253901, June 2010. doi:10.1103/PhysRevLett.104.253901.

[172] J. Caron. *Model-based reconstruction of magnetisation distributions in nanostructures from electron optical phase images*. PhD thesis. Forschungszentrum Jülich GmbH Zentralbibliothek, Verlag, Jülich, 2018.

[173] A. Lubk and J. Zweck. Differential phase contrast: An integral perspective. *Physical Review A*, 91(2):023805, February 2015. doi:10.1103/PhysRevA.91.023805.

[174] S. You, P.-H. Lu, T. Schachinger, A. Kovács, R. E. Dunin-Borkowski, and A. M. Maiden. Lorentz near-field electron ptychography. *Applied Physics Letters*, 123(19):192406, November 2023. doi:10.1063/5.0169788.

[175] J. Cui, H. Sha, W. Yang, and R. Yu. Antiferromagnetic imaging via ptychographic phase retrieval. *Science Bulletin*, 69(4):466–472, February 2024. doi:10.1016/j.scib.2023.12.044.

[176] S. McVitie and G. S. White. Imaging Amperian currents by Lorentz microscopy. *Journal of Physics D: Applied Physics*, 37(2):280, December 2003. doi:10.1088/0022-3727/37/2/018.

[177] F. Junginger, M. Kläui, D. Backes, S. Krzyk, U. Rüdiger, T. Kasama, R. E. Dunin-Borkowski, J.-M. Feinberg, R. J. Harrison, and L. J. Heyderman. Quantitative determination of vortex core dimensions in head-to-head domain walls using off-axis electron holography. *Applied Physics Letters*, 92(11):112502, March 2008. doi:10.1063/1.2829601.

[178] J. Caron. Magnetisation reconstruction in three dimensions. In *Model-based reconstruction of magnetisation distributions in nanostructures from electron optical phase images*, pages 119–140. PhD thesis. Forschungszentrum Jülich GmbH Zentralbibliothek, Verlag, Jülich, 2018.

[179] P. Diehle, A. Kovács, T. Duden, R. Speen, K. Žagar Soderžnik, and R. E. Dunin-

Borkowski. A cartridge-based turning specimen holder with wireless tilt angle measurement for magnetic induction mapping in the transmission electron microscope. *Ultramicroscopy*, 220:113098, January 2021. doi:10.1016/j.ultramic.2020.113098.

[180] K. A. Mohan, P. KC, C. Phatak, M. De Graef, and C. A. Bouman. Model-Based Iterative Reconstruction of Magnetization Using Vector Field Electron Tomography. *IEEE Transactions on Computational Imaging*, 4(3):432–446, September 2018. doi:10.1109/TCI.2018.2838454.

[181] M. Mansuripur. Computation of electron diffraction patterns in Lorentz electron microscopy of thin magnetic films. *Journal of Applied Physics*, 69(4):2455–2464, February 1991. doi:10.1063/1.348682.

[182] J. Caron. Reconstructibility and null spaces. In *Model-based reconstruction of magnetisation distributions in nanostructures from electron optical phase images*, pages 74–82. PhD thesis. Forschungszentrum Jülich GmbH Zentralbibliothek, Verlag, Jülich, 2018.

[183] S. McVitie, S. Hughes, K. Fallon, S. McFadzean, D. McGrouther, M. Krajnak, W. Legrand, D. Maccariello, S. Collin, K. Garcia, N. Reyren, V. Cros, A. Fert, K. Zeissler, and C. H. Marrows. A transmission electron microscope study of Néel skyrmion magnetic textures in multilayer thin film systems with large interfacial chiral interaction. *Scientific Reports*, 8(1):5703, April 2018. doi:10.1038/s41598-018-23799-0.

[184] M. Weyland and P. Midgley. Electron Tomography. In C. B. Carter and D. B. Williams, editors, *Transmission Electron Microscopy: Diffraction, Imaging, and Spectrometry*, pages 343–376. Springer International Publishing, Cham, 2016. doi:10.1007/978-3-319-26651-0_12.

[185] S. van der Walt, J. L. Schönberger, J. Nunez-Iglesias, F. Boulogne, J. D. Warner, N. Yager, E. Gouillart, and T. Yu. scikit-image: image processing in Python. *PeerJ*, 2:e453, June 2014. doi:10.7717/peerj.453.

[186] F. de la Peña, E. Prestat, V. T. Fauske, P. Burdet, P. Jokubauskas, M. Nord, T. Ostasevicius, K. E. MacArthur, M. Sarahan, D. N. Johnstone, J. Taillon, J. Lähnemann, V. Migunov, A. Eljarrat, J. Caron, T. Aarholt, S. Mazzucco, M. Walls, T. Slater, F. Winkler, pquinn dls, B. Martineau, G. Donval, R. McLeod, E. R. Hoglund, I. Alxneit, D. Lundeby, T. Henninen, L. F. Zagonel, and A. Garmannslund. hyper-

spy/hyperspy: HyperSpy v1.5.2, September 2019. doi:10.5281/zenodo.3396791.

[187] G. W. Paterson, R. W. H. Webster, A. Ross, K. A. Paton, T. A. Macgregor, D. McGrouther, I. MacLaren, and M. Nord. Fast Pixelated Detectors in Scanning Transmission Electron Microscopy. Part II: Post-Acquisition Data Processing, Visualization, and Structural Characterization. *Microscopy and Microanalysis*, 26(5):944–963, October 2020. doi:10.1017/S1431927620024307.

[188] P. A. Penczek, J. Zhu, and J. Frank. A common-lines based method for determining orientations for $N > 3$ particle projections simultaneously. *Ultramicroscopy*, 63(3):205–218, July 1996. doi:10.1016/0304-3991(96)00037-X.

[189] P. Virtanen, R. Gommers, T. E. Oliphant, M. Haberland, T. Reddy, D. Cournapeau, E. Burovski, P. Peterson, W. Weckesser, J. Bright, S. J. van der Walt, M. Brett, J. Wilson, K. J. Millman, N. Mayorov, A. R. J. Nelson, E. Jones, R. Kern, E. Larson, C. J. Carey, I. Polat, Y. Feng, E. W. Moore, J. VanderPlas, D. Laxalde, J. Perktold, R. Cimrman, I. Henriksen, E. A. Quintero, C. R. Harris, A. M. Archibald, A. H. Ribeiro, F. Pedregosa, and P. van Mulbregt. SciPy 1.0: fundamental algorithms for scientific computing in Python. *Nature Methods*, 17(3):261–272, March 2020. doi:10.1038/s41592-019-0686-2.

[190] J. Caron. A forward model for the calculation of the magnetic phase. In *Model-based reconstruction of magnetisation distributions in nanostructures from electron optical phase images*, pages 21–57. PhD thesis. Forschungszentrum Jülich GmbH Zentralbibliothek, Verlag, Jülich, 2018.

[191] J. Nocedal and S. J. Wright. Conjugate Gradient Methods. In *Numerical Optimization*, pages 101–134. Springer, New York, NY, 2006. doi:10.1007/978-0-387-40065-5_5.

[192] M. van Heel and M. Schatz. Fourier shell correlation threshold criteria. *Journal of Structural Biology*, 151(3):250–262, September 2005. doi:10.1016/j.jsb.2005.05.009.

[193] J. Ungermann, M. Kaufmann, L. Hoffmann, P. Preusse, H. Oelhaf, F. Friedl-Vallon, and M. Riese. Towards a 3-D tomographic retrieval for the air-borne limb-imager GLORIA. *Atmospheric Measurement Techniques*, 3(6):1647–1665, November 2010. doi:10.5194/amt-3-1647-2010.

[194] J. M. D. Teresa, A. Fernández-Pacheco, R. Córdoba, L. Serrano-Ramón, S. San-

giao, and M. R. Ibarra. Review of magnetic nanostructures grown by focused electron beam induced deposition (FEBID). *Journal of Physics D: Applied Physics*, 49(24):243003, May 2016. doi:10.1088/0022-3727/49/24/243003.

[195] L. Houben and M. Bar Sadan. Refinement procedure for the image alignment in high-resolution electron tomography. *Ultramicroscopy*, 111(9):1512–1520, August 2011. doi:10.1016/j.ultramic.2011.06.001.

[196] A. Kovács, J. Caron, A. S. Savchenko, N. S. Kiselev, K. Shibata, Z.-A. Li, N. Kanazawa, Y. Tokura, S. Blügel, and R. E. Dunin-Borkowski. Mapping the magnetization fine structure of a lattice of Bloch-type skyrmions in an FeGe thin film. *Applied Physics Letters*, 111(19):192410, November 2017. doi:10.1063/1.5004394.

[197] D. Song, Z.-A. Li, J. Caron, A. Kovács, H. Tian, C. Jin, H. Du, M. Tian, J. Li, J. Zhu, and R. E. Dunin-Borkowski. Quantification of Magnetic Surface and Edge States in an FeGe Nanostripe by Off-Axis Electron Holography. *Physical Review Letters*, 120(16):167204, April 2018. doi:10.1103/PhysRevLett.120.167204.

[198] J. Caron. Solving the inverse problem of magnetisation retrieval. In *Model-based reconstruction of magnetisation distributions in nanostructures from electron optical phase images*, FZJ-2018-05288, pages 59–82. PhD thesis, Forschungszentrum Jülich GmbH Zentralbibliothek, Verlag, Jülich, 2018. doi:http://hdl.handle.net/2128/19740.

[199] F. Tejo, R. H. Heredero, O. Chubykalo-Fesenko, and K. Y. Guslienko. The Bloch point 3D topological charge induced by the magnetostatic interaction. *Scientific Reports*, 11(1):21714, November 2021. doi:10.1038/s41598-021-01175-9.

[200] K. Halbach. Design of permanent multipole magnets with oriented rare earth cobalt material. *Nuclear Instruments and Methods*, 169(1):1–10, February 1980. doi:10.1016/0029-554X(80)90094-4.

[201] W. Jiang. Quantifying chiral exchange interaction for Néel-type skyrmions via Lorentz transmission electron microscopy. *Physical Review B*, 99(10), 2019. doi:10.1103/PhysRevB.99.104402.

[202] J. Nocedal and S. J. Wright. Introduction. In *Numerical Optimization*, pages 1–9. Springer, New York, NY, 2006. doi:10.1007/978-0-387-40065-5_1.

[203] A. Apseros, V. Scagnoli, M. Holler, M. Guizar-Sicairos, Z. Gao, C. Appel, L. J. Heyderman, C. Donnelly, and J. Ihli. X-ray linear dichroic tomography of crys-

tallographic and topological defects. *Nature*, 636(8042):354–360, December 2024. doi:10.1038/s41586-024-08233-y.

List of figures

List of tables